TRAJECTORY PLANNING FOR SPACECRAFT FORMATIONS NEAR ELLIPTICAL ORBITS

A Dissertation

Presented to the Faculty of the Graduate School

of Cornell University

in Partial Fulfillment of the Requirements for the Degree of

Doctor of Philosophy

by

Darren Joseph Zanon

May 2009

TRAJECTORY PLANNING FOR SPACECRAFT FORMATIONS NEAR ELLIPTICAL ORBITS

Darren Joseph Zanon, Ph.D.

Cornell University 2009

Hamilton-Jacobi-Bellman (HJB) optimization is used to find optimal solutions to cost functions for spacecraft formation maneuver planning. Such solutions are first explored using splines to approximate functions which are otherwise difficult to evaluate. This technique is applied to simple problems of formation transits for a four-satellite tetrahedron performing maneuvers similar to those proposed for the Magnetospheric Multiscale (MMS) mission by assuming thrust along two axes. This scenario and mission are further used as a basis for generating a mixed-metric cost function in which the tetrahedron is evaluated for ability to take meaningful scientific data. The methods derived for solving this cost function can be utilized for advanced exploration of mission profiles for MMS-type formations with constraints. These HJB methods are then combined with Linear Programming (LP) methods and extended to apply to problems in which the spacecraft thrust is applied by a set of thrusters on a spacecraft which is rotating, providing a practical method for determining optimal formation maneuvers for realistic multi-spacecraft missions with complex thruster layouts. Several parameterizations are also derived which can describe single-spacecraft relative orbits and multiple-spacecraft formations. In many cases, these parameterizations provide insight into general properties which apply to underlying optimal formation maneuvers. These can be readily adapted by mission designers to enhance mission performance and extend mission life.

BIOGRAPHICAL SKETCH

Darren Joseph Zanon received his B.A. in physics from Gustavus Adolphus College in 2001 and an M.S. from Cornell University in Aerospace Engineering, with a focus on Guidance, Navigation, and Control, in 2005. His work on optimal maneuvers for spacecraft formations has been published in the *Journal of Guidance, Control, and Dynamics* and presented at several conferences. His academic interests include both open-loop and closed-loop optimal control methods, with a focus on computational solution techniques for on-orbit maneuvers.

For Melissa, with all my love.

ACKNOWLEDGEMENTS

This project would not have been possible without my adviser, Dr. Mark Campbell, to whom I will be forever grateful. I also owe sincere thanks to the other members of my faculty committee: Dr. Mason Peck gave me insights into different dimensions of the satellite design world, while Dr. Joe Burns kept me excited about the familiar world of physics. My deepest gratitude (and sympathies) also go out to the professors and teachers who poked and prodded me to do better throughout the years.

Of my friends, too many to list, I would especially like to thank my best friend, Melissa, whom I had the good fortune to marry. Which is a great segue to Shan, who has been sensible enough to know that living might be work, but work shouldn't be life. Brett and Sherback, you're always welcome on my couch — or even in the spare bed. This also applies to Justin and Edgar, who have put up with a lot from this old man. Mike M, you helped push me to finish, though you beat me at the wire. I'd also like to thank Terry, Eelco, Jarurat, Bernardo, Atif, Ramu, and Mike T, who made work in Upson a lot more interesting.

Finally, a big acknowledgement goes to my soon-to-be born child, whose debut became the ultimate deadline.

TABLE OF CONTENTS

LIST OF FIGURES

LIST OF TABLES

LIST OF SYMBOLS

The following is a list of the most commonly used symbols. Others symbols are defined as needed in the text.

$\dot{()}$	Derivative with respect to time
$()'$	Derivative with respect to true anomaly
$()^i$	For the formation, referring to the ith element in the cluster
$()_{\mathrm{PL}}$	Planar position, velocity, and parameterization elements
$()_{\mathrm{CR}}$	Cross-axis position, velocity, and parameterization elements
$()^N$	Position or velocity in inertially fixed reference frame
$()^R$	Position or velocity in relative reference frame
$()^B$	Position or velocity in spacecraft body frame
$()^*$	Single-spacecraft or formation optimal
$()_{\mathrm{MC}}$	Monte Carlo optimal (MC optimal)
θ	Reference orbit true anomaly
a	Orbit altitude
e	Orbit eccentricity
μ	Central gravitational constant
m	Spacecraft mass
ω	Spacecraft orbit angular rate
$\Phi(\theta)$	Fundamental matrix solution to linearized relative dynamics
$\mathbf{Q} = \begin{bmatrix} \mathbf{Q}_{\mathrm{PL}} \\ \mathbf{Q}_{\mathrm{CR}} \end{bmatrix}$	Vector representation of single-spacecraft thrust effect
p_j^i	Relative parameterization element p_j for the ith spacecraft
$\mathbf{p} = \begin{bmatrix} \mathbf{p}_{\mathrm{PL}} \\ \mathbf{p}_{\mathrm{CR}} \end{bmatrix}$	Relative reference frame parameterization vector
$\mathbf{x}_c$	Relative position of apparent formation center
$\mathbf{x}_p^i(\theta)$	Relative position of ith spacecraft at true anomaly θ
$\mathbf{x}$	Spacecraft state (position and velocity) in relative reference frame
$\mathbf{z} = \begin{bmatrix} \mathbf{z}_{\mathrm{PL}} \\ \mathbf{z}_{\mathrm{CR}} \end{bmatrix}$	Spacecraft state in angular velocity-normalized reference frame
$\mathbf{R}$	Spacecraft position in inertial reference frame
$\mathbf{\Delta}$	Relative reference frame single-spacecraft parameterization
$\mathbf{\Delta}_s$	Relative reference frame stable, single-spacecraft parameterization
$\mathbf{\Upsilon} = \{\mathbf{\Upsilon}_{\mathrm{free}}, \mathbf{\Upsilon}_{\mathrm{fixed}}\}$	Relative reference frame formation parameterization, fixed and free elements
$\mathbf{q}$	Formation rotation quaternion
$\mathbf{x}^{ij}$	Vector distance from Spacecraft i to Spacecraft j
τ	Formation quality factor cut-off for science cost calculation
$\mathbf{T}$	Thrust vector in relative reference frame
$\mathbf{u}$	Vector thrust-to-mass ratio

θ_C	Critical true anomaly at which the formation is in an equilateral tetrahedron
θ_D	True anomaly at which data is desired to be taken
d^{ij}	Normative distance from Spacecraft i to Spacecraft j
$d_{\max}$	Maximum allowed interspacecraft separation distance for true anomalies in Θ_{sci}
$d_{\min}$	Minimum allowed interspacecraft separation distance
L_{tet}	Nominal tetrahedron leg length at critical true anomaly θ_C
$\bar{L}$	Mean tetrahedron leg length
δ_{sci}	Minimum allowed science window width
Θ_{sci}	Region of the orbit, given by $\Theta_{\text{sci}} = [\theta_C - \delta_{\text{sci}}, \theta_C + \delta_{\text{sci}}]$, in which data is scientifically viable
δ_D^+, δ_D^-	True anomaly bounds, about θ_D, of the data-taking region
Θ_D	Region of the orbit, given by $\Theta_D = \left[\theta_D - \delta_D^-, \theta_D + \delta_D^+\right]$, in which data-taking occurs
Q_{R8}	Fractional geometric quality factor for formation evaluation
J^i_{fuel}	Single-spacecraft maneuver fuel cost
J_{fuel}	Formation maneuver fuel cost
J_{sci}	Formation data-taking capability in cost functional form
J_{MMS}	Formation cost — a weighted sum of science and fuel costs
α_{fuel}	Fuel cost multiplier in formation cost
$\alpha_{\text{sci,0}}$	Maneuver start science cost multiplier in formation cost
$\alpha_{\text{sci,F}}$	Maneuver end science cost multiplier in formation cost
α_{sci}	Science cost multiplier for maneuvers in which initial science cost is not considered
$\underline{\mathbf{q}}$	Formation rotation quaternion about relative reference frame axes
$\mathbf{q}$	Formation rotation quaternion vector
$T(\theta)$	Time-varying rotation matrix from body to inertial frames
$\mathcal{S}$	Matrix of unit thrust directions
$\boldsymbol{\alpha}(\theta)$	Time-varying thrust activation vector
$\aleph$	Linear Programming thrust activation vector
$\mathcal{Q}$	Splined thrust approximation matrix
$\mathcal{Q}_S$	Linear Programming thrust approximation matrix

Chapter 1: Introduction

Spacecraft formation flying is a developing technology with potentially significant implications. Multi-spacecraft missions can provide improved scientific results at a lower cost than their single-spacecraft counterparts while allowing for more flexible mission designs. Additional spacecraft add redundancy to the system and can be deployed in a variety of orbital conditions, including highly elliptical and Lagrange point orbits. Both NASA and the Department of Defense have shown recent interest in the technology[1, 2, 3, 4]. While system-level improvements must be made to ensure consistent communication, formation attitude control, and fault detection — particularly in high-radiation environments — further progress in optimizing formation maneuvers will greatly enhance the performance of the success of these missions.

Early work on formation flying focused on finding closed-form descriptions of optimal formation maneuvers for a single spacecraft near a circular orbit[5, 6]. Further advancements incorporated additional formation elements[7, 8], collision avoidance constraints[9], and motion in a nonspherical gravitational field[10]. However, none of these solutions addresses the complexities of the high-eccentricity orbits proposed for many spacecraft formation missions. Carter and Humi[11] resolved the motion of a spacecraft near an elliptical orbit, and later improvements[12, 13] made possible a description of the motion which was free of singularities. That work was partially developed to produce solutions using local linearization[14], which proves sufficient for small eccentricities but produces unreliable solutions for high eccentricities. This dissertation builds upon Carter's formulation to solve for fuel-optimal formation maneuvers for spacecraft near an arbitrary Keplerian orbit. The primary examples of spacecraft formations utilized in this paper are the four-spacecraft Magnetospheric Multiscale mission[1] and a modified version of the two-member CU Sat mission[15]. The dissertation is presented

as three papers, each addressing a different aspect of the spacecraft formation flying problem.

The first paper provides the foundation for solving the formation optimal maneuver problem using a Hamilton-Jacobi-Bellman (HJB) formulation. This method minimizes a cost function by considering variations in a costate problem whose dynamics are related to those of the originating system. Due to the complexity of the problem at hand, some of the integrals are approximated using a piecewise polynomial, or spline, describing the integrated effects of thrust inputs on the spacecraft. These minimum-fuel transit solution methods are then applied to an MMS-like formation in which the spacecraft are capable of thrust along two axes; by varying one or more system parameters, significant fuel savings can be made.

The second paper builds on these results by first solving the approximated integrals, then by applying realistic problem constraints. The paper then examines different methods for reducing a complex parametric space describing the tetrahedron formation and considers the consequences of these reductions. It also seeks to provide mission planners a series of signposts which may be useful for mission design.

The third and final paper considers the formation optimal maneuver problem for a CU Sat-like spacecraft pair in which the objective is for one spacecraft to image the other. The problem complexity increases by including a time-varying set of thrust vectors whose effects can again not be integrated. By applying the spline techniques used previously, an approximation of these effects can be made, and Linear Programming can be deployed to obtain a piecewise optimal solution to the problem. Because the LP solution is only approximate, HJB methods can be employed to improve on the LP solutions and obtain optimal or near-optimal formation maneuvers.

Each paper is presented in full.

Chapter 2: Optimal Planner for Spacecraft Formations in Elliptical Orbits[1]

Abstract

An optimal planner for spacecraft formations in elliptical reference orbits is presented. A fast solution to an individual spacecraft minimum time or fuel maneuver utilizing the Hamilton-Jacobi-Bellman formulation is developed using spline approximations to evaluate thrust effect integrals. The individual optimal spacecraft maneuvers use realistic low thrust, bounded inputs similar to those produced by electric propulsion systems. A formation optimal planner is then formulated using the individual spacecraft maneuvers as a basis. The formulation is easily scalable to larger clusters, provably optimal over the formation, and numerically robust; it also requires minimal communication between fleet members. An example is presented of a tetrahedron formation in a highly elliptical reference orbit ($e = 0.8$), with solutions to both formation minimum time and minimum fuel problems given. Comparison with linear programming techniques show a distinct savings in fuel usage for high eccentricity examples.

2.1 Introduction

Autonomous satellite formations represent a key component in several ongoing and proposed NASA and Department of Defense projects[1, 3, 4, 17]. These missions will require a variety of formations held under vastly differing orbital conditions. The advantages to such formations are an increase in scientific gains while potentially saving costs and extending mission life. However, the technological challenges presented by

[1]Published under this title, by Darren J. Zanon and Mark E. Campbell, *Journal of Guidance, Control, and Dynamics*, Vol 29, No 1, Pg 161-171, Jan-Feb 2006.

this technique have been difficult to overcome: fleet-wide communication and fault detection, collision avoidance, and path planning and control are all active areas of exploration in the field[7, 18, 19].

The planning and control problem is generally posed in two forms: formation *maneuvering*, where the spacecraft plan and execute a thrust command to move the cluster from one stable formation to another; and formation *keeping*, where the spacecraft remain in a stable formation to within a specified tolerance in the presence of disturbances. While these problems are related and can be addressed by similar methodologies, it is important to explore both in detail in order to ensure accurate performance of the formation as a whole.

Both problems have been addressed in recent literature. A thorough review of the body of work in which both theoretical and practical solutions and applications for the single-satellite linearized rendezvous problem have been offered is given in [20] and [21], as well as by Carter[13]. Formation keeping algorithms have been constructed using several control techniques, including traditional feedback control[22] and higher-order orbit descriptions[5], but these solutions do not adequately address formation maneuver problems, such as minimizing fuel across a fleet of spacecraft transiting between stable formations about an elliptical orbit.

The formation keeping problem has also been addressed using convex optimization[23], which discretizes the trajectory in terms of the true anomaly and integrates constraints such as error boxes and thrust saturation in a parallelizable approach. These techniques were also applied to the formation maneuvering problem; [23] shows a low-eccentricity example of a linear programming solution for generating thrust maps. As described in [23], however, the computational burden of the linear program increases as the number of discretization points along the trajectory increases. Several methods for resolving

this problem are proposed, including coarser discretization, application of constraints at only a subset of points, and the use of a receding horizon (in formation keeping only) — each at the expense of performance (typically fuel usage or final position accuracy). In addition, while the linear programs can be shown to be optimal, they are only optimal for the discretized system, not the originating continuous time system.

For maneuvering, other solutions often rely on finite-horizon planning with quadratic cost thrust[8], consider only impulsive thrusts with quadratic cost[24], or examine low-earth orbits[10]. While finite-horizon methods are adaptable and effective, they are also computationally intensive when used for clusters and frequently rely on specialty software. Quadratic costs, meanwhile, tend to simplify the problem but do not adequately represent the large class of high specific impulse, low-thrust devices which are the most realistic for use on precision formations of satellites[25, 26]; [27] shows that the use of a quadratic cost can require up to an additional 50 percent more fuel usage when compared to the more appropriate absolute fuel cost. Finally, restrictions to low altitudes limit applicability to high-earth orbiting clusters with relatively high eccentricities, such as the Magnetospheric Multiscale (MMS) mission [1].

The objective of this work is to construct a full-maneuver planning and control methodology that is optimal across a cluster of spacecraft in formation about a general elliptical orbit, extending the work in [18]. The approach utilizes a direct point-to-point analysis for the general linearized relative orbit, which is then built into a formation-optimal control methodology. The approach is unique in that it develops formation maneuvers that are provably optimal across the entire cluster, works well in all regimes for which the linearization is valid, considers absolute thrust limitations, and is flexible for solving problems involving any cost using fuel and time. As shown in [9], it can also be expanded to work with additional constraints, such as those on collision avoidance,

and is computationally tractable and parallelizable across the individual spacecraft in a cluster.

The paper is presented as follows. First, a summary of the relative orbital dynamics is presented as a basis for the formation planning work. Key to this work is the ability to generate point-to-point optimal control solutions for a single spacecraft as quickly as possible. To this end, a spline method is presented which allows the state transition matrix for the relative dynamics to be written analytically, and therefore used in the development of optimal controllers. The spline work is general enough that it can be applied to a variety of other related problems, such as those which include non-spherical gravitational effects[28]. Next, a thorough treatment of formation parameterizations is given. This is important to the overall methodology because, unique to formation maneuvering, the cluster optimal (fuel or time) plan attempts to minimize the cost across the fleet as a function of these parameters. Finally, the formation optimal control methodology is outlined using the above tools and is applied to an example of a four-spacecraft tetrahedron formation.

2.2 Relative Orbital Dynamics

The relative dynamics of a spacecraft about an elliptical reference orbit are generally given by a local linearization. A key aspect of the work presented here is defining the state propagation as an analytic function via the state transition matrix. Using procedures outlined in [14], [29], and [30], the equations of motion for a satellite in a general force field $f(\mathbf{R})$ with thrust $\mathbf{T}$ are given by

$$\ddot{\mathbf{r}} = -f(\mathbf{R})\mathbf{r} - f'(\mathbf{R})\left(\frac{\mathbf{R}\cdot\mathbf{r}}{|\mathbf{R}|}\right)\mathbf{R} + \frac{\mathbf{T}}{m} \tag{2.1}$$

where $\mathbf{R}$ is the position of a reference satellite with respect to the center of gravitational attraction and $\mathbf{r}$ is the relative position of the spacecraft from this reference, and $|\mathbf{r}| \ll |\mathbf{R}|$

Transforming to a rotating frame centered on the reference orbit, where the x_3 axis points in the direction of the reference orbit angular momentum vector, x_2 is aligned with the position vector $\mathbf{R}$, and x_1 completes the right-hand set, the relative and absolute positions become $\mathbf{r} = (x_1, x_2, x_3)$ and $\mathbf{R} = (0, R, 0)$, with the rotational velocity of the satellite given by $\Omega = (0, 0, \omega)$.

In a general elliptical orbit, the position and angular rate are functions of the true anomaly θ, so that $\mathbf{R} = \mathbf{R}(\theta)$ and $\omega = \omega(\theta)$. In the following derivation, let $(\cdot)'$ denote differentiation with respect to θ. Using Equation 2.1 and the conservation of angular momentum $R^2\omega = const = L$, the relative position and velocity are normalized via

$$y_i = \omega(\theta)^{\frac{1}{2}} x_i \ , \quad v_i = y_i' \ , \quad u_i = \frac{T_i}{m} \ , \tag{2.2}$$

The generalized force can be re-written as $G[\omega(\theta)] = -\omega(\theta)^{-2} f'(\mathbf{R})\mathbf{R}$, and the motion is represented by a linear equation. In the case of a general Newtonian gravitational field,

$$G[\omega(\theta)] = -\frac{d}{dR}\left(\frac{\mu}{R(\theta)^3}\right)\frac{R(\theta)}{\omega(\theta)^2} \tag{2.3}$$

where μ is the constant of gravitational attraction of the central body.

The transformed system has a propagation equation

$$\mathbf{z}(\theta) \quad = \quad \Phi(\theta)\Phi^{-1}(\theta_0)\mathbf{z}(\theta_0) + \Phi(\theta)\int_{\theta_0}^{\theta} \Phi^{-1}(\tau)B(\tau)\mathbf{u}\, d\tau \tag{2.4}$$

where $\mathbf{z}(\theta) = (y_1, v_1, y_2, v_2, y_3, v_3)$, and $\Phi(\theta)$ and its inverse are as given by Carter[13], with the correction that

$$
\begin{aligned}
\phi_3^{'}(\theta) &= 6e\phi_1^{'}(\theta)K(\theta) + \frac{6e\sin^3\theta}{\rho(\theta)^3} - \frac{4\sin\theta(e+\cos\theta)}{\rho(\theta)^3} \\
&\quad + \sin\theta\cos\theta\frac{(2+e\cos\theta)}{\rho(\theta)^2} + 2\sin\theta\cos\theta \\
K(\theta) &= \int \frac{\sin^2\theta}{\rho(\theta)^4}\, d\theta \\
\rho(\theta) &= 1 + e\cos\theta
\end{aligned}
$$

as in Appendix A. This solution is valid for eccentricities $0 \leq e < 1$.

Further defining

$$
\mathbf{Q}[\theta_0, \theta] = \int_{\theta_0}^{\theta} \Phi^{-1}(\tau)B(\tau)\mathbf{u}\, d\tau \tag{2.5}
$$

the state propagation equation is simply

$$
\mathbf{z}(\theta) = \Phi(\theta)\Phi^{-1}(\theta_0)\mathbf{z}(\theta_0) + \Phi(\theta)\mathbf{Q}[\theta_0, \theta] \tag{2.6}
$$

This equation captures only linearized motion, though it could be extended to incorporate nonlinear perturbations. Writing $\mathbf{y}(\theta) = (y_1, y_2, y_3)^T$, $\mathbf{v}(\theta) = (v_1, v_2, v_3)^T$, the un-normalized relative states can be recovered using

$$
\begin{aligned}
\mathbf{x}(\theta) &= \frac{L^{\frac{3}{2}}}{\mu}\left(\frac{\mathbf{y}(\theta)}{\rho(\theta)}\right) && (2.7) \\
\dot{\mathbf{x}}(\theta) &= \frac{\mu}{L^{\frac{3}{2}}}[e\sin\theta\mathbf{y}(\theta) + \rho(\theta)\mathbf{v}(\theta)] && (2.8)
\end{aligned}
$$

2.3 Analytical Approximations of State Propagation

A solution to the state propagation (Equation 2.6) is dictated by the solvability of $\mathbf{Q}[\theta_0, \theta]$. Using the transformations

$$\sin E = \frac{\sqrt{1-e^2}\,\sin\theta}{\rho(\theta)}\,, \quad \cos E = \frac{\cos\theta + e}{\rho(\theta)} \tag{2.9}$$

and the identity

$$\omega(\theta) = \frac{\rho(\theta)^2}{C^2}\,, \quad C = \left(\frac{L^3}{\mu^2}\right)^{\frac{1}{2}} \tag{2.10}$$

the components of **Q** become

$$\begin{aligned}
Q(1) &= C^3 \int_{\theta_0}^{\theta} \left(-2\frac{u_1}{\rho(\theta)^3}\left[3e\rho(\theta)^2 K(\theta) - \frac{\sin\theta}{\rho(\theta)}\right]\right. \\
&\qquad \left. -\frac{u_2}{\rho(\theta)^3}\left[-6e^2\rho(\theta)\sin\theta K(\theta) + \frac{2e\sin^2\theta}{\rho(\theta)^2} - \frac{\cos\theta}{\rho(\theta)}\right]\right) d\theta \qquad (2.11)\\
Q(2) &= \frac{-2u_1C^3}{(1-e^2)^{\frac{5}{2}}}\left[\left(\frac{e^3}{2} - e\right)E + \sin E - \frac{e}{4}\left(E + \sin E\cos E\right)\right] \\
&\qquad -\frac{u_2C^3}{(1-e^2)}\cos E \qquad (2.12)\\
Q(3) &= \frac{u_1C^3}{(1-e^2)^{\frac{5}{2}}}\left[E - 2e\sin E + \frac{e^2}{2}(E + \sin E\cos E)\right] \qquad (2.13)\\
Q(4) &= C^3 \int_{\theta_0}^{\theta} \left(-\frac{u_1}{\rho(\theta)^3}\left[-6\rho(\theta)^2 K(\theta) - \frac{2\sin\theta\cos\theta}{\rho(\theta)} - \sin\theta\cos\theta\right] - \frac{u_2}{\rho(\theta)^3}\times\right. \\
&\qquad \left. \left[6e\rho(\theta)\sin\theta K(\theta) - \frac{2\sin^2\theta}{\rho(\theta)^2} - \frac{\cos^2\theta}{\rho(\theta)} - \cos^2\theta\right]\right) d\theta \qquad (2.14)\\
Q(5) &= \frac{-u_3C^3}{(1-e^2)^2}\left(\frac{e}{2}\cos^2 E - \cos E\right) \qquad (2.15)\\
Q(6) &= u_3C^3\left(\frac{\sin\theta}{\rho(\theta)^3} - 3eK(\theta)\right) \qquad (2.16)
\end{aligned}$$

There are no singularities at $e = 0$ in the closed-form solutions.

A considerable amount of difficulty arises when attempting to evaluate $Q(1)$ and $Q(4)$, as no closed-form solution exists to the integration of $\rho(\theta)^{-1}K(\theta)$. However, because the planner methodology derived in this work is based on analytical models, a good approximation of the integral is sufficient.

One relatively precise method for approximating integrals is to use a set of piecewise polynomials (PP) to form a spline function. Consider a real, continuous function $g(x)$,

with a series of m breakpoints, or knots, defining the endpoints of $m-1$ intervals on that function: $g(t_0), g(t_1), ..., g(t_m)$. The PP approximation for each interval is a kth-order polynomial representation identically equal to $g(x)$ at the endpoints of the interval, such that

$$\hat{g}_i(x) = a_0 + a_1 x + a_2 x^2 + ... + a_{k-1} x^{k-1}, \quad t_{i-1} \leq x \leq t_i \tag{2.17}$$

where

$$\hat{g}_i(t_{i-1}) = g(x)|_{x=t_{i-1}}, \quad \hat{g}_i(t_i) = g(x)|_{x=t_i} \tag{2.18}$$

The collection of polynomials is a spline of the function, written compactly as $\hat{g}_{PP}(x) = [\hat{g}_1(x \in [t_0, t_1]), \hat{g}_2(x \in [t_1, t_2]), ...]$; the spline is continuous, since $\hat{g}_{PP}(t_i) = \hat{g}_i(t_i) = \hat{g}_{i+1}(t_i)$. Also, because $\hat{g}_{PP}(x)$ is a continuous function of polynomials, its integral is continuous and has the same breakpoints as the original spline. The accuracy of the representation of certain functions is particularly sensitive to the order k, the location and number of knots.

In general, note that the error in the integral over any segment in such a spline approximation will never deviate from the true value by more than

$$\max_{x \in [t_{i-1},\, t_i]} (\hat{g}_i(x) - g(x)) \times (t_i - t_{i-1})$$

A spline representation is clearly not unique, and an effective method of determining coefficients on each spline segment attempts to minimize the maximum error over each segment. The method employed for this survey is de Boor's Algorithm. A complete treatment of the construction of piecewise polynomial interpolants can be found in [31] and [32].

Consider now each of the integrands of $Q(1)$ and $Q(4)$ from Equations 2.11 and 2.14 as the originating function $g(x)$ for a spline. These functions are continuous and differentiable, so an approximation over some arbitrary interval approaches the exact

value as knot spacing approaches zero. To illustrate the usefulness of the approximation, consider a spacecraft orbiting Earth at altitude $2Re$ that thrusts radially for a quarter orbit from apogee, then against-track to perigee. The 2-norm of the position error when the spacecraft returns to apogee is calculated as the difference between the position using a numerical solver and the position using a spline approximation of Equations 2.11 and 2.14. As shown in Figure 2.1, this error drops off dramatically using fewer than 20 knots for a 4th-order spline, even as eccentricity increases. To ensure feasibility of results, all examples in this paper utilize 512 knots per orbit. Because this is simply a function call, the large number of knots has minimal effects on the overall computational time.

Propagation of the state of the system can now be performed for any given series of finite-width inputs $\mathbf{u}^1, \mathbf{u}^2, ..., \mathbf{u}^j$, from which minimum-time and minimum-fuel planners can be derived. The final state of the system is

$$\begin{aligned} \mathbf{z}(\theta_f) &= \Phi(\theta_f)\Phi^{-1}(\theta_0)\mathbf{z}(\theta_0) + \Phi(\theta_f)\left(\mathbf{Q}_{\mathbf{u}^1}[\theta_1, \theta_2] + \right. \\ &\quad \left. \mathbf{Q}_{\mathbf{u}^2}[\theta_2, \theta_3] + ... + \mathbf{Q}_{\mathbf{u}^j}[\theta_j, \theta_{j+1}]\right) \end{aligned} \tag{2.19}$$

2.4 Formation Parameterization

Cluster optimal maneuvers are defined by minimizing a formation-based cost, subject to varying one or more parameters in the system. It is therefore vital for formation optimization to use a parameterization scheme which is both easy to implement and adaptable to as many formation mission problems as possible. In order to facilitate cluster optimal control, definitions for spacecraft formation parameterizations are introduced.

Based on the stable solutions to the unforced dynamics, each spacecraft within a formation of N satellites can be defined using a set of parameters $\mathbf{\Delta} = [\mathbf{\Delta}_1, \mathbf{\Delta}_2, ..., \mathbf{\Delta}_N]$,

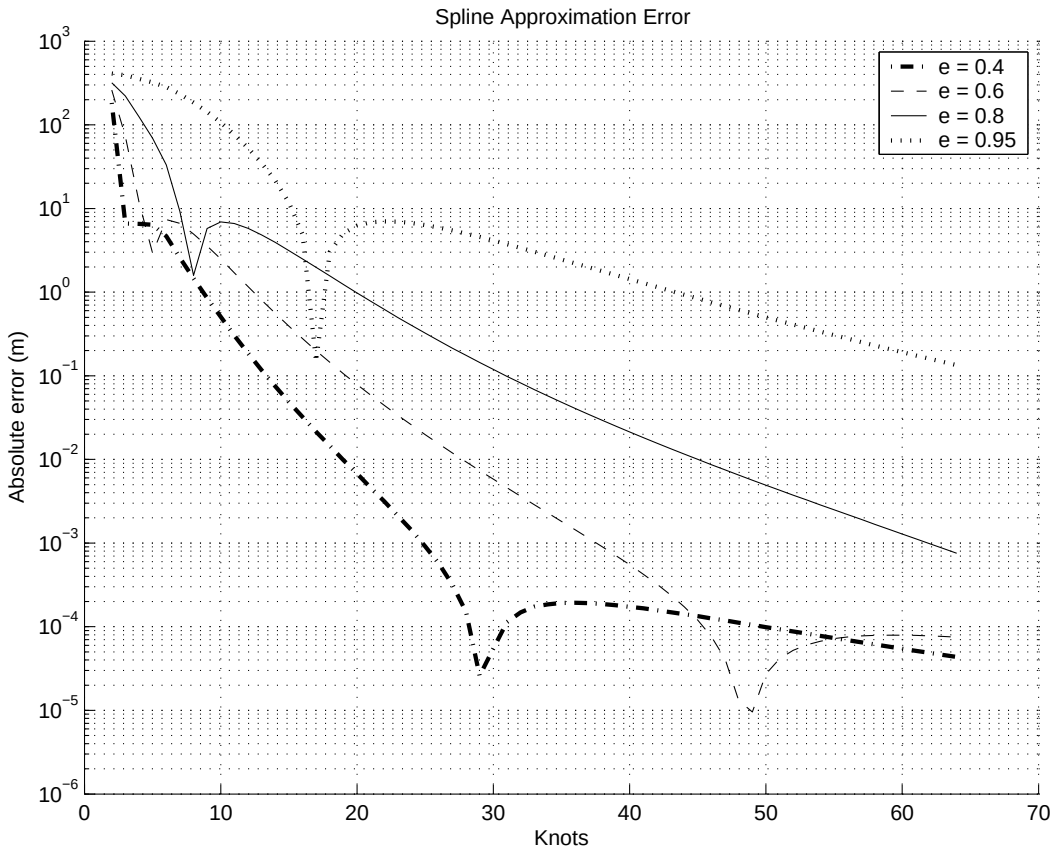

Figure 2.1: Fourth-order spline precision as a function of knot spacing for various eccentricities. The 2-norm of the final position error is calculated for a spacecraft at altitude 2 Re beginning on an elliptical orbit and thrusting in-track for 1/4 orbit and radially for 1/4 orbit. Input thrust is $u = -6 \times 10^{-5}\ N$ and final position is approximately $2.0 \times 10^{3}\ m$ from reference center. A precipitous drop occurs with relatively few knots even at high eccentricity.

which include those parameters necessary to uniquely define the state of each satellite. Specific definitions for these parameters are given in Section 4.1. Related to all spacecraft within the formation is a fleet-wide set of formation parameters, described using Υ. The approach here, as shown in Section 4.2, is to define the formation using a desired shape at only one true anomaly θ_C with a center $\mathbf{x}_c = (x_1, x_2, x_3)_c$; this shape can be rotated about any axis and translated.

The complete set of elements for a formation is then given by $\mathbf{\Lambda} = [\mathbf{\Delta};\ \Upsilon, \theta_C]$, and optimization occurs over any subset of elements contained in $\mathbf{\Delta}$ (specific to one satellite) or Υ (common to all formation elements). The formation optimal maneuver can then be written compactly as

$$\mathbf{\Lambda}_F^* = \min_{\mathbf{\Lambda}_F} \ J_{FORMATION}(\mathbf{\Lambda}_0, \mathbf{\Lambda}_F) \tag{2.20}$$

where $J_{FORMATION}$ is the formation-based cost, typically a function of time and fuel. Here, $\mathbf{\Lambda}_0$ is assumed to be a known initial formation parameter set, while some subset of parameters in $\mathbf{\Lambda}_F$ is to be optimized over. Note that other variations of the problem are also possible, such as free parameters in $\mathbf{\Lambda}_0$, though these problems are generally not useful for on-board applications.

2.4.1 Single Spacecraft Parameterizations, $\mathbf{\Delta}_i$

The solution to the cluster-optimal control problem is rooted in the parameterization of the initial state of each member, $\mathbf{\Delta}_i$. A stable, unforced initialization for a satellite at an arbitrary point (x_1, x_2, x_3) in the reference frame about the eccentric trajectory at true anomaly θ can be found using the representation given by Inalhan *et al*[14] in terms of the original coordinate states, x_i. These states can be written in a slightly different and more insightful way as

$$x_1(\theta) = \frac{p_1}{\rho(\theta)} + \left(\frac{1}{\rho(\theta)} + 1\right)(ep_2 \cos\theta + p_3 \sin\theta) + p_4\left[2eJ(\theta)\rho(\theta)\right] \quad (2.21)$$

$$x_2(\theta) = p_3 \cos\theta - ep_2 \sin\theta - p_4\left[\frac{e\cos\theta}{\rho(\theta)^2} - 2e^2 J(\theta)\right] \quad (2.22)$$

$$x_3(\theta) = p_5\frac{\sin\theta}{\rho(\theta)} + p_6\frac{\cos\theta}{\rho(\theta)} \quad (2.23)$$

where

$$J(\theta) = \frac{\sin\theta}{\rho(\theta)} - 3eK(\theta) \quad (2.24)$$

Note that $J(\theta)$ is not a periodic function. The constants can be arbitrarily chosen to produce an orbit about an elliptical reference, but stable formations — i.e. those in which the state repeats after N full orbits — require that the non-periodic $J(\theta)$ elements be eliminated. Thus, the constant p_4 must be set to 0, and all elements in brackets in Equations 2.21-2.23 drop out. This leaves five variables to describe all stable relative orbits. From these, the first single-spacecraft parameter set is given as $\mathbf{\Delta}_i = [p_1, p_2, p_3, p_5, p_6]$.

The role of each of the constants p_i is readily apparent. In particular, the elements (p_2, p_3) define a circle of radius $\sqrt{p_3^2 + (ep_1)^2}$, while p_1 defines variable against-track offset at each angle, bounded by $[p_1/(1+e),\ p_1/(1-e)]$. Figure 2.2 shows the planar motion of three stable initializations as a function of parameter p_1. Note that these stable orbits are in general not symmetric, experiencing deformations based on the chosen parameter values. The amplitude of the cross-track oscillation is given by $\sqrt{p_5^2 + p_6^2}$, and the motion is skewed due to the $\rho(\theta)^{-1}$ relationship.

The corresponding converted z-coordinate position and velocity components can be calculated directly from Equations 2.21-2.23 using the transformations from Equations 2.7 and 2.8. The six unforced initialization states become:

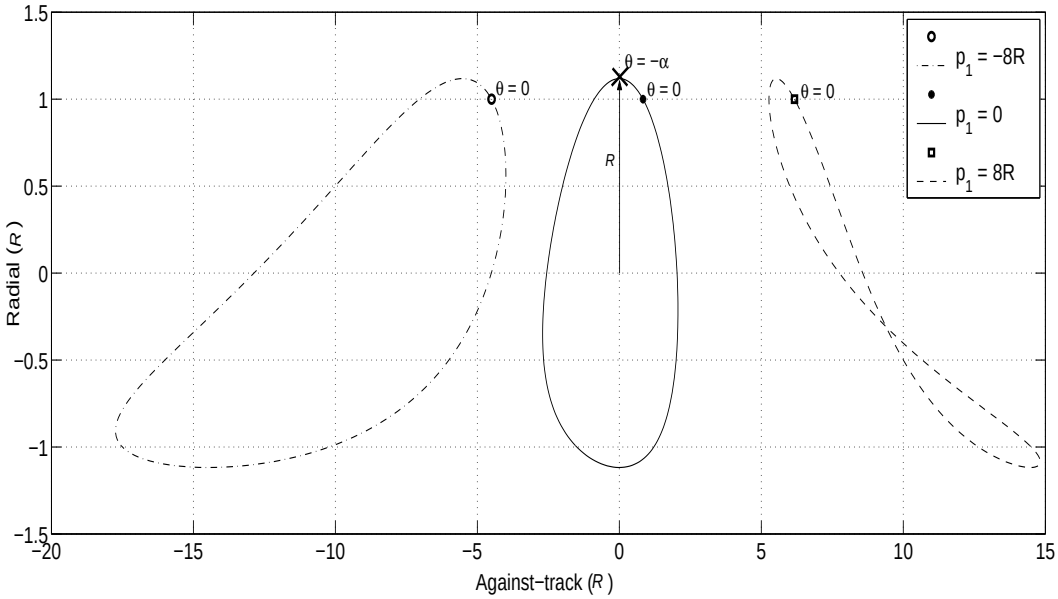

Figure 2.2: Effects of the choice of parameter value p_1 at $e = 0.5$. Orbits produced by varying p_1 at non-zero eccentricities are both offset and skewed.

$$y_1(\theta) = C^{-1}p_1 + C^{-1}(\rho(\theta)+1)\,(ep_2\cos\theta + p_3\sin\theta) \tag{2.25}$$

$$v_1(\theta) = \left(1+\frac{1}{\rho(\theta)}\right)y_2(\theta) - C^{-1}(e\sin\theta)\,(ep_2\cos\theta + p_3\sin\theta) \tag{2.26}$$

$$y_2(\theta) = \omega(\theta)^{\frac{1}{2}}\,(p_3\cos\theta - ep_2\sin\theta) \tag{2.27}$$

$$v_2(\theta) = -\frac{e\sin\theta}{\rho(\theta)}\,y_2(\theta) - \omega(\theta)^{\frac{1}{2}}\,(ep_2\cos\theta + p_3\sin\theta) \tag{2.28}$$

$$y_3(\theta) = C^{-1}\,(p_5\sin\theta + p_6\cos\theta) \tag{2.29}$$

$$v_3(\theta) = C^{-1}\,(p_5\cos\theta - p_6\sin\theta) \tag{2.30}$$

with $\omega(\theta)$ and C as defined in Equation 2.10. Notice that the relationship between y_2 and v_1 approaches that given by Inalhan and How for initialization at perigee ($\theta = 0$)[23].

The set $\mathbf{\Delta}_i$ gives the parameterization for the stable initialization for the ith satellite. This set is clearly not unique, as other transformations of the state parameters also

provide a parameterization for each cluster member.

2.4.2 Centered Parameterizations for Single Spacecraft

For clusters, a reduction of the size of the parameter set of each formation member often provides a more functional means of solving the optimal control problem. Centered formations, or those where $p_1 = 0$ (see Figure 2.2), are considered in the remainder of this paper. A more detailed analysis of non-centered orbits is given in [33]. Centered formations always encircle the point $(x_1, x_2) = (0, 0)$; the parameter set for a centered orbit can then be written $\mathbf{\Delta}^c = \{\mathbf{\Delta} \mid p_1 = 0\}$. For this case, another insightful parameter set can be defined[16] as $\mathbf{\Delta}^c_{R,i} = [R, \alpha, R_{x_3}, \alpha_{x_3}]$, where size and phasing parameters are used; for this case, the unforced equations reduce to those given by Campbell[9] for the circular reference orbit.

In the formation optimal planner examined in this paper, the satellite parameterization is defined using a formation shape at the critical true anomaly θ_C. This shape is given by a position basis $\boldsymbol{P}_i$ for each satellite, which locates each member of the formation about the cluster center. The position of the ith spacecraft with respect to this center at θ_C is then given by

$$\mathbf{x}_{\Delta_i}(\theta_C) = l \cdot \boldsymbol{P}_i \tag{2.31}$$

where l is a scaling length and the elements of $\mathbf{x}_{\Delta_i}$ correspond to the position elements in Equations 2.21-2.23. As a simplification, it is assumed that the formation is centered ($p_1 = 0$) and that $\dot{x}_{3,i}(\theta_C) = 0$ This parameterization is given by $\mathbf{\Delta}^c_{P,i} = [l \cdot \mathbf{P}_i, p_1 = 0, \dot{x}_{3,i}(\theta_C) = 0]$.

As an example, consider four spacecraft arranged in a regular tetrahedron. This formation corresponds to the demands of the MMS mission. It is characterized by position bases which place four satellites unit distance apart:

$$\mathbf{P}_{MMS,1} = \begin{pmatrix} 0 \\ \frac{\sqrt{3}}{2\sqrt{2}} \\ 0 \end{pmatrix}, \quad \mathbf{P}_{MMS,2} = \begin{pmatrix} 0 \\ \frac{-\sqrt{3}}{6\sqrt{2}} \\ \frac{-\sqrt{3}}{3} \end{pmatrix}, \quad \mathbf{P}_{MMS,3} = \begin{pmatrix} -\frac{1}{2} \\ \frac{-\sqrt{3}}{6\sqrt{2}} \\ \frac{\sqrt{3}}{6} \end{pmatrix}, \quad \mathbf{P}_{MMS,4} = \begin{pmatrix} \frac{1}{2} \\ \frac{-\sqrt{3}}{6\sqrt{2}} \\ \frac{\sqrt{3}}{6} \end{pmatrix}$$

and is then denoted by the parameterization $\mathbf{\Delta}^c_{P_{MMS}} = \{\mathbf{\Delta}^c_P \mid \mathbf{P} = \mathbf{P}_{MMS}\}$.

2.4.3 Formation Parameterizations, Υ

A formation of N satellites begins with the definition of a parameter set $\mathbf{\Delta}_i$ for each spacecraft. The formation is defined about a center point $\mathbf{x}_c$, which can be rotated via Euler rotations T_{ij} about the relative motion coordinate axes through angles $(\psi_{12}, \psi_{13}, \psi_{23})$. As well, the center can be translated to some point $\mathbf{x}_c$. The set of rotations, the specification of the formation center, and the number of satellites are invariant over all spacecraft in the formation; such parameters are contained in the formation parameterization set $\Upsilon = [N, \mathbf{x}_c, (\psi_{12}, \psi_{13}, \psi_{23})]$. The relationship between the actual position of the satellite at the formation true anomaly θ_C and the elements of the sets $\mathbf{\Delta}_i$ and Υ is illustrated in Figure 2.3 and given mathematically by

$$\mathbf{x}_i(\theta_C) = \mathbf{x}_c + T_{12}T_{13}T_{23}\mathbf{x}_{\Delta_i}(\theta_C) \tag{2.32}$$

While it is possible to define the formation at only true anomaly θ_C, it is important for optimal control purposes to be able to uniquely place the spacecraft on a stable orbit at an arbitrary true anomaly θ using a given parameterization. This can be accomplished by first converting to the **z** frame via Equations 2.7-2.8, propagating the system through a zero-thrust maneuver to the desired true anomaly, and transforming back to **x** coordinates. Likewise, the values of p_i can be determined using Equations 2.7-2.8 and Equations 2.25-2.30:

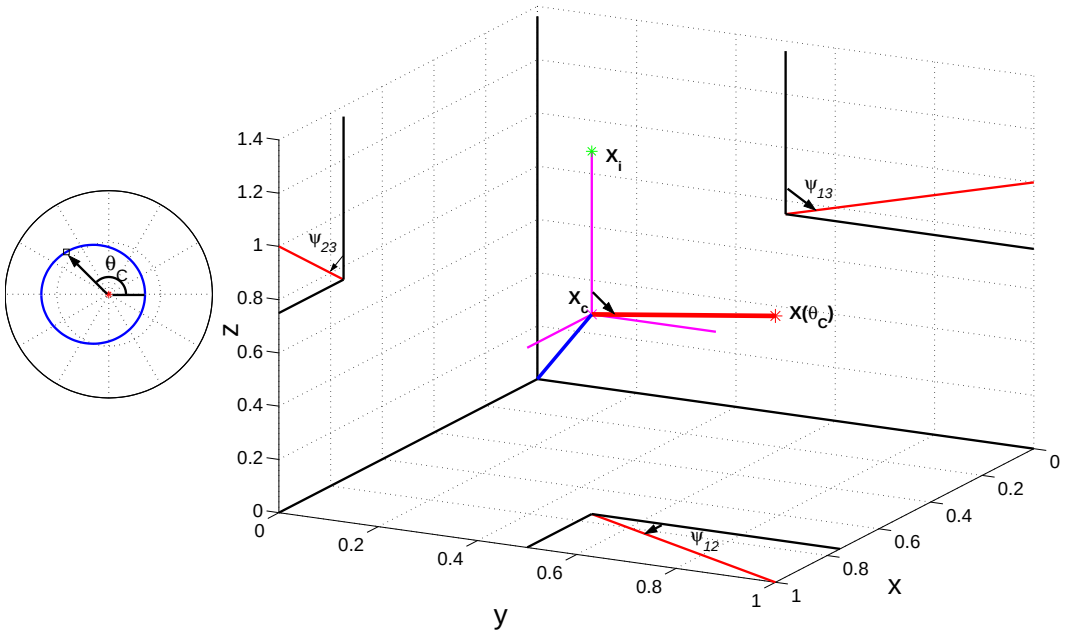

Figure 2.3: The position of a single spacecraft in relation to formation parameters θ_C, $\mathbf{x}_c$, and $(\psi_{12}, \psi_{13}, \psi_{23})$.

$$\mathbf{x}_i(\theta_C) \xrightarrow{\text{Equations 7-8}} \mathbf{z}_i(\theta_C) \xrightarrow{\text{Equation 4, } u=0} \mathbf{z}_i(\theta) \xrightarrow{\text{Equations 7-8}} \mathbf{x}_i(\theta) \xrightarrow{\text{Equations 7-8, 25-30}} [p_1, \ldots, p_6] \tag{2.33}$$

The formation can therefore be described compactly as $\mathbf{\Lambda} = [\mathbf{\Delta};\ \Upsilon, \theta_C]$. For most optimization problems, the cost is evaluated by varying a subset of the single-spacecraft parameters in $\mathbf{\Delta}_i$ and/or the parameters of the formation set Υ. To differentiate the optimization variables, the parameter sets can be partitioned into free and fixed parameters such that $\mathbf{\Delta}_i = [\mathbf{\Delta}_i(free) \mid \mathbf{\Delta}_i(fixed)]$ and $\Upsilon = [\Upsilon(free) \mid \Upsilon(fixed)]$.

2.5 Formation Optimal Maneuvers

Time-optimal and fuel-optimal maneuvers for a spacecraft have been widely explored in the last two decades. Most recently, Campbell[18] used relative dynamics and a circular reference orbit to develop formation optimal minimum time and minimum fuel planners

for satellite formations based on optimal thrust for two inputs. This work extends the approach to the eccentric orbit case using the state propagation equation, the spline approximation in Section 3, and the formation parameterizations in Section 4. While only cluster fuel- and time-optimal formulations are considered here, the results are general and can be integrated into the planning methodology described in [18], with constraints such as collision avoidance and communication; other considerations may be required as well, depending on the mission demands. As in the circular case, though, solution times must remain under one orbit, with true anomaly $\theta \leq 2\pi$, to guarantee validity[18].

The formation optimal maneuver between initial cluster parameterization $\mathbf{\Lambda_0}$ and final cluster parameterization $\mathbf{\Lambda}_F$ is defined by the formation cost

$$\mathbf{\Lambda}_F^* = \min_{\mathbf{\Lambda}_F} J_{FORMATION}(\mathbf{\Lambda}_0, \mathbf{\Lambda}_F) \tag{2.34}$$

Formation optimal maneuvers are developed here using single spacecraft optimal control. The generation of single-spacecraft optimal maneuvers is presented for both minimum time and minimum fuel cases. The solution approach is integrated into a methodology to solve Equation 2.34.

2.5.1 Single Spacecraft Minimum Time

The cost function for a minimum time optimal maneuver for a single spacecraft uses the fact that the true anomaly θ increases monotonically with time and can be defined as

$$J_T = \int_{\theta_0}^{\theta_F} d\theta \tag{2.35}$$

Because the cross-axis y_3 element is decoupled, the six states in the original optimal control problem are separated into a four-state problem in the orbital plane and a two-state problem out of the orbital plane.

For the in-plane problem and assuming thrust-limited propulsion as with electric thrusters, following [18], the shape of the time-optimal input for a single spacecraft in the orbital plane is assumed to be a three-switch *bang-bang* thrust sequence terminating at the minimum time. Dropping the subscript i notation for this section and further simplifying the model to consider thrust input in the along-track direction only, the planar state is $\mathbf{z}_p = (y_1, v_1, y_2, v_2)^T$ with state matrices $(A(\theta), B(\theta))$ defined as

$$A(\theta) = \begin{bmatrix} 0 & 1 & 0 & 0 \\ 0 & 0 & 0 & 2 \\ 0 & 0 & 0 & 1 \\ 0 & -2 & G[\omega(\theta)] & 0 \end{bmatrix} \quad B(\theta) = \begin{pmatrix} 0 \\ \omega(\theta)^{-\frac{3}{2}} \\ 0 \\ 0 \end{pmatrix} \tag{2.36}$$

The initial condition $\mathbf{z}_p(\theta_0)$ is assumed to be known. Let $\mathbf{Q}^p$ be the first four elements of the $\mathbf{Q}$ vector, given in Equations 2.11-2.14. The elements of the jth input vector $\mathbf{Q}_j^p$ on each of the four constant-thrust intervals $[\theta_{j-1}, \theta_j]$ become

$$\mathbf{Q}_j^p[\theta_{j-1}, \theta_j] = (-1)^{j-1} u \begin{pmatrix} -2S[S[\phi_2(\theta)]\omega(\theta)^{-\frac{3}{2}}] \\ 2S[S[\phi_1(\theta)]\omega(\theta)^{-\frac{3}{2}}] \\ S[\omega(\theta)^{-\frac{3}{2}}] \\ -S[S[\phi_3(\theta)]\omega(\theta)^{-\frac{3}{2}}] \end{pmatrix} \Bigg|_{\theta_{j-1}}^{\theta_j}$$

It is important to note that spline construction can be performed *a priori* using only the orbital data. Thus, the computation time does not generally increase as the number of knots increases.

From the adjoint system

$$\lambda'(\theta) = -A^T(\theta)\lambda(\theta) \tag{2.37}$$

the Hamiltonian can be defined as

$$\mathcal{H}_T(\theta) = 1 + \boldsymbol{\lambda}^T(\theta)[A(\theta)\mathbf{z}_p(\theta) + B(\theta)(-1)^{j-1}u], \quad \theta_{j-1} \leq \theta \leq \theta_j \tag{2.38}$$

The costate at any true anomaly θ is

$$\boldsymbol{\lambda}(\theta) = \Psi_{[1\text{-}4]}(\theta)\Psi^{-1}_{[1\text{-}4]}(\theta_0)\boldsymbol{\lambda}_0 \tag{2.39}$$

where the full matrix Ψ is given by Carter[13] and shown in Appendix B. The notation $[\cdot]_{[r\text{-}s]}$ represents the $(s-r+1)\times(s-r+1)$ square partition of the referenced matrix $[\cdot]$ containing both $[\cdot](r,r)$ and $[\cdot](s,s)$.

The constraints to be satisfied for the time-optimal control problem for a single spacecraft are

$$\begin{aligned}
\mathbf{z}_p(\theta_F^*) &= \Phi_{[1\text{-}4]}(\theta_F^*)\Phi^{-1}_{[1\text{-}4]}(\theta_0)\mathbf{z}_p(\theta_0) + \Phi_{[1\text{-}4]}(\theta_F^*)\Big(\mathbf{Q}_1^p[\theta_0,\theta_1^*]+ \\
&\qquad \mathbf{Q}_2^p[\theta_1^*,\theta_2^*] + \mathbf{Q}_3^p[\theta_2^*,\theta_3^*] + \mathbf{Q}_4^p[\theta_3^*,\theta_F^*]\Big) \qquad (2.40)\\
\boldsymbol{\lambda}^T(\theta_i^*)B(\theta_i^*) &= 0 \ , \ \ i = 1,2,3 \qquad (2.41)\\
\mathcal{H}_T(\theta_F^*) &= 0 \qquad (2.42)
\end{aligned}$$

with $\mathbf{z}_p(\theta_F)$ determined as described in Equation 2.33. The values θ_i^* represent the true anomaly values at which the control input switches. This problem has eight unknowns: three switches $(\theta_1^*, \theta_2^*, \theta_3^*)$, the final time for the maneuver (θ_F^*), and four initial conditions on the costate $(\boldsymbol{\lambda}_0)$. There are also eight constraint equations; note that all switch times θ_i^* are solvable independent of the costate. Thus, the costate solution simply verifies optimality. Using the final angle θ_F as a free parameter representing the shut-off time for the thrust inputs, the constraint equations for the input times can be solved numerically.

The cross-axis problem consists of a two-state system which is decoupled from the in-plane problem. The minimum time control input for maneuvering under one orbit

is again *bang-bang*, consisting of a single switch (θ_1^*) and a shut-off time (θ_F^*). The dynamics in the rotating **z** frame are given by

$$\begin{pmatrix} y_3 \\ v_3 \end{pmatrix}' = \begin{bmatrix} 0 & 1 \\ -1 & 0 \end{bmatrix} \begin{pmatrix} y_3 \\ v_3 \end{pmatrix} + \begin{bmatrix} 0 \\ \omega(\theta)^{-\frac{3}{2}} \end{bmatrix} u_3 \tag{2.43}$$

Let $\mathbf{Q}_i^{z_3}$ be the 2-element vector $(Q_i(5), Q_i(6))^T$, and recall from Equations 2.15 and 2.16 that this input vector has a closed-form solution. Defining $\mathbf{z_3} = (y_3, v_3)^T$ and the out-of-plane costate similar to the planar costate as $\boldsymbol{\lambda}_{z_3}(\theta)$, the optimal thrust constraints are

$$\begin{aligned} \mathbf{z_3}(\theta_F^*) &= \Phi_{[5\text{-}6]}(\theta_F^*)\Phi_{[5\text{-}6]}^{-1}(\theta_0)\mathbf{z_3}(\theta_0) + \Phi_{[5\text{-}6]}(\theta_F^*) \times \\ &\qquad \left(\mathbf{Q}_1^{z_3}[\theta_0, \theta_1^*] + \mathbf{Q}_2^{z_3}[\theta_1^*, \theta_F^*]\right) && (2.44) \\ \boldsymbol{\lambda}_{z_3}^T(\theta_i^*)B_{z_3}(\theta_i^*) &= 0 \ , \quad i = 1, 2, 3 && (2.45) \\ \mathcal{H}_{z_3,T}(\theta_F^*) &= 0 && (2.46) \end{aligned}$$

2.5.2 Single Spacecraft Minimum Fuel

The single spacecraft minimum fuel problem uses a cost function defined as

$$J_F = \int_{t_0}^{t_F} |\mathbf{u}| \, dt \tag{2.47}$$

with $|\cdot|$ denoting the summed absolute value of the vector. The time dependence of this cost must first be converted to true anomaly in order to solve using the true anomaly-based dynamics used here. The time and true anomaly differentials are related by

$$dt = \sqrt{\frac{a^3}{\mu}} \frac{(1-e^2)^{\frac{3}{2}}}{\rho(\theta)^2} \, d\theta = \omega(\theta)^{-1} \, d\theta \tag{2.48}$$

The solution is assumed to be *bang-off-bang*, with the planar maneuver beginning at time θ_0 and ending at time θ_F. The planar solution consists of four thrust segments and is defined by six unknowns. In this case, the constraints for the minimum fuel problem are given by

$$\begin{aligned} \mathbf{z}_p(\theta_F) &= \Phi_{[1\text{-}4]}(\theta_F)\Phi^{-1}_{[1\text{-}4]}(\theta_0)\mathbf{z}_p(\theta_0) + \Phi_{[1\text{-}4]}(\theta_F)\left(\mathbf{Q}^p_1[\theta_0, \theta^*_1]+\right. \\ &\qquad \left.\mathbf{Q}^p_2[\theta^*_2, \theta^*_3] + \mathbf{Q}^p_3[\theta^*_4, \theta^*_5] + \mathbf{Q}^p_4[\theta^*_6, \theta_F]\right) \qquad (2.49) \\ \boldsymbol{\lambda}^T(\theta^*_i)B(\theta^*_i) &= -sgn((u(\theta^*_i))\omega(\theta)^{-1} \quad , \quad i = 1, 2, 3, 4, 5, 6 \qquad (2.50) \end{aligned}$$

where $sgn(u)$ indicates

$$\begin{aligned} u(\theta) &= u \quad \text{for} \quad \boldsymbol{\lambda}^T(\theta)B(\theta) < -\omega(\theta)^{-1} \\ u(\theta) &= 0 \quad \text{for} \quad -\omega(\theta)^{-1} \le \boldsymbol{\lambda}^T(\theta)B(\theta) \le +\omega(\theta)^{-1} \qquad (2.51) \\ u(\theta) &= -u \quad \text{for} \quad \boldsymbol{\lambda}^T(\theta)B(\theta) > +\omega(\theta)^{-1} \end{aligned}$$

and $\boldsymbol{\lambda}(\theta)$ is given by Equation 2.39. Unlike the minimum time problem, the solution for the switching true anomalies is coupled with the costate, resulting in 10 coupled nonlinear equations. These equations can be reduced to six coupled nonlinear equations by first finding $\boldsymbol{\lambda}_0$ through the overdetermined matrix costate equation

$$\begin{bmatrix} B(\theta_1)^T\Psi(\theta_1) \\ - - - - - \\ B(\theta_2)^T\Psi(\theta_2) \\ - - - - - \\ \vdots \\ - - - - - \\ B(\theta_6)^T\Psi(\theta_6) \end{bmatrix} \Psi(\theta_0)^{-1}\boldsymbol{\lambda}_0 = \begin{bmatrix} \omega(\theta_1)^{-1} \\ - - - \\ \omega(\theta_2)^{-1} \\ - - - \\ \vdots \\ - - - \\ \omega(\theta_6)^{-1} \end{bmatrix} \qquad (2.52)$$

The cross axis maneuver is assumed to occur during the same time period $[\theta_0, \theta_F]$, but, to allow more solution flexibility, it is not assumed to begin and end at these points. Instead, it is a two-thrust sequence with four unknown switches and two initial costate elements. The solution is found by the equations

$$\begin{aligned} \mathbf{z}_3(\theta_F) &= \Phi_{[5\text{-}6]}(\theta_F)\Phi^{-1}_{[5\text{-}6]}(\theta_0)\mathbf{z}_3(\theta_0) + \Phi_{[5\text{-}6]}(\theta_F) \times \\ &\qquad \left(\mathbf{Q}_1^{z_3}[\theta_1^*, \theta_2^*] + \mathbf{Q}_2^{z_3}[\theta_3^*, \theta_4^*]\right) \qquad (2.53) \\ \boldsymbol{\lambda}^T_{z_3}(\theta_i^*)B_{z_3}(\theta_i^*) &= -sgn(u(\theta)_i^*)\omega(\theta)^{-1} \quad , \quad i = 1, 2, 3, 4 \qquad (2.54) \end{aligned}$$

which can be reduced to four equations in a manner similar to the planar case.

2.6 Simulation Results

In order to examine formation optimal planners, consider a tetrahedral formation of four satellites, as described in Section 4.3. The orbital data and formation correspond to the proposed Magnetospheric Multiscale mission[1], a cluster which will operate in medium- to high-altitude orbits with $e \gtrsim 0.7$. The scientific goals of MMS require the formation to be a tetrahedron with leg length approximately 1 km at apogee, with no constraints on formation orientation; the tetrahedron can reconfigure its size and orientation during each orbit. The objective of the formation planner is to optimize such a reconfiguration to leg length 1.1 km starting at apogee and finishing before the following apogee over the final Euler angle $\psi_{12,F}$ based on the formation cost. For this problem, both formation optimal minimum time and minimum fuel solutions are generated. While motion occurs in three dimensions, the cross-axis is invariant under rotations about ψ_{12} and therefore does not enter the formation optimization problem.

Table 2.1: Initial and final parameter values for example simulation.

		Parameter	Initial	Final
Reference		a	12 *Re*	12 *Re*
		e	0.8	0.8
		μ	3.986012×10^5	3.986012×10^5
$\mathbf{\Lambda}_i$	θ_C		π	π
	$\mathbf{\Delta}_i$	$l \cdot \mathbf{P}_i$	1.0 km $\cdot\mathbf{P}_i$	1.1 km $\cdot\mathbf{P}_i$
		p_1	0	0
		$\dot{x}_3(\theta_C)$	0	0
	$\mathbf{\Upsilon}$	N	4	4
		$\mathbf{x}_c$	$(0,0,0)$	$(0,0,0)$
		$(\psi_{12}, \psi_{13}, \psi_{23})$	$(0, 45^\circ, 45^\circ)$	$(\psi_{12}, 45^\circ, 45^\circ)$

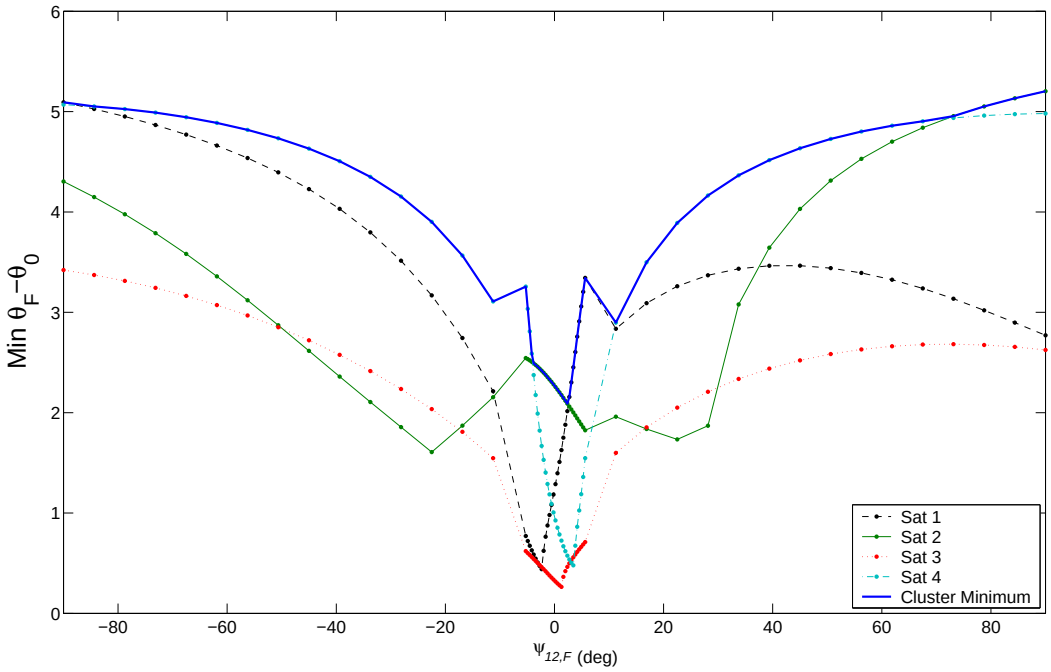

Figure 2.4: Minimum time solution for variable ψ_{12} for the example problem. The solid line represents the cluster minimum time at each angle, with optimal final angle $\psi_{12} = 2.3°$.

2.6.1 Minimum Time

The formation minimum time control problem is defined as

$$\mathbf{\Lambda}_F^* = \min_{\psi_{12}} \max_{i\in[1,\ldots,4]} J_{T,i} \tag{2.55}$$

The minimum maneuver time and the optimal final cluster rotation angle ψ_{12} can be found using Figure 2.4, which gives the single-spacecraft minimum time solutions at each angle. The cluster minimum solution — which corresponds to the worst-case single-satellite minimum time — is shown in bold. The four-satellite optimal plan results in the smallest cluster minimum time, which occurs at approximately $\psi_{12,F} = 2.3°$; at this point, the cluster maneuver time is 7 percent less than with zero rotation ($\psi_{12} = 0°$). This shows that although the final rotation is small, significant cost savings can be attained by considering a cluster optimal solution.

In this problem, 63 evaluations of $\psi_{12,F}$ were made for each spacecraft by performing two scans. First, the profile of $\psi_{12,F} \in [-90°, 90°]$ was scanned using 33 evenly-spaced points. Then, the central region of $\psi_{12,F} \in [-5.625°, 5.625°]$, where the coarse profile shows a minimum, was further scanned using a fine grid of 32 points with $0.35°$ spacing. The fine-grid scan — which requires only a good initial profile and can therefore be initialized using partial *a priori* solution information — requires less than 5 sec to evaluate each point using a MATLAB implementation on a Pentium IV, 1.8 GHz machine. Because the process is parallelizable, each spacecraft can evaluate its own profile, and the planner implementation in this region can be performed in ∼3 min. Clearly, a C/C++ implementation and a more effective scanning routine would further speed this solution process.

The three-dimensional motion of this cluster-optimal maneuver is shown in Figure 2.5. It is evident that the spacecraft both begin and end in a tetrahedron formation,

though they are not in this formation at intermediate points. The maneuver is completed at a true anomaly of $\theta_F = 5.25$ rad, or before the four satellites reach perigee. Therefore, the second half of the trajectory occurs under unforced, stable dynamics. Note that collision avoidance is not considered here and is unnecessary for this example due to the large spacing between the spacecraft, but it could in general be added as a constraint as in [9].

2.6.2 Minimum Fuel

A formation optimal minimum fuel plan is generated using the sum of the fuel usage over all spacecraft. This is given as

$$\mathbf{\Lambda}_F^* = \min_{\psi_{12}} \sum_{i=1}^{4} J_{F,i} \tag{2.56}$$

for a fixed final true anomaly θ_F. From Equations 2.47 and 2.48, it is clear that the cost for large eccentricities is weighted towards thrusts occurring near perigee, where a small input is most effective at changing the trajectory of the satellite. With this objective, the fuel optimal cost for each satellite and the fleet-wide minimum fuel solutions for the sample problem are shown in Figure 2.6 for a final true anomaly of 0.92 orbits past apogee, such that $\theta_F = \theta_0 + 0.92(2\pi)$. The plot has been truncated to show the region of importance. The cluster minimum occurs at zero rotation ($\psi_{12} = 0^\circ$), where a savings of 94 percent in fuel use is attained over the minimum time solution.

The planar single-spacecraft minimum-fuel solution can have up to six switches and as few as four switches, depending on the final true anomaly. Figure 2.7 shows a plot of the switch times and fuel as a function of the end maneuver time, θ_F. For small θ_F, the solution includes six switches and follows a profile that closely resembles the minimum time solution with brief intermediate coasts. For small increases in θ_F,

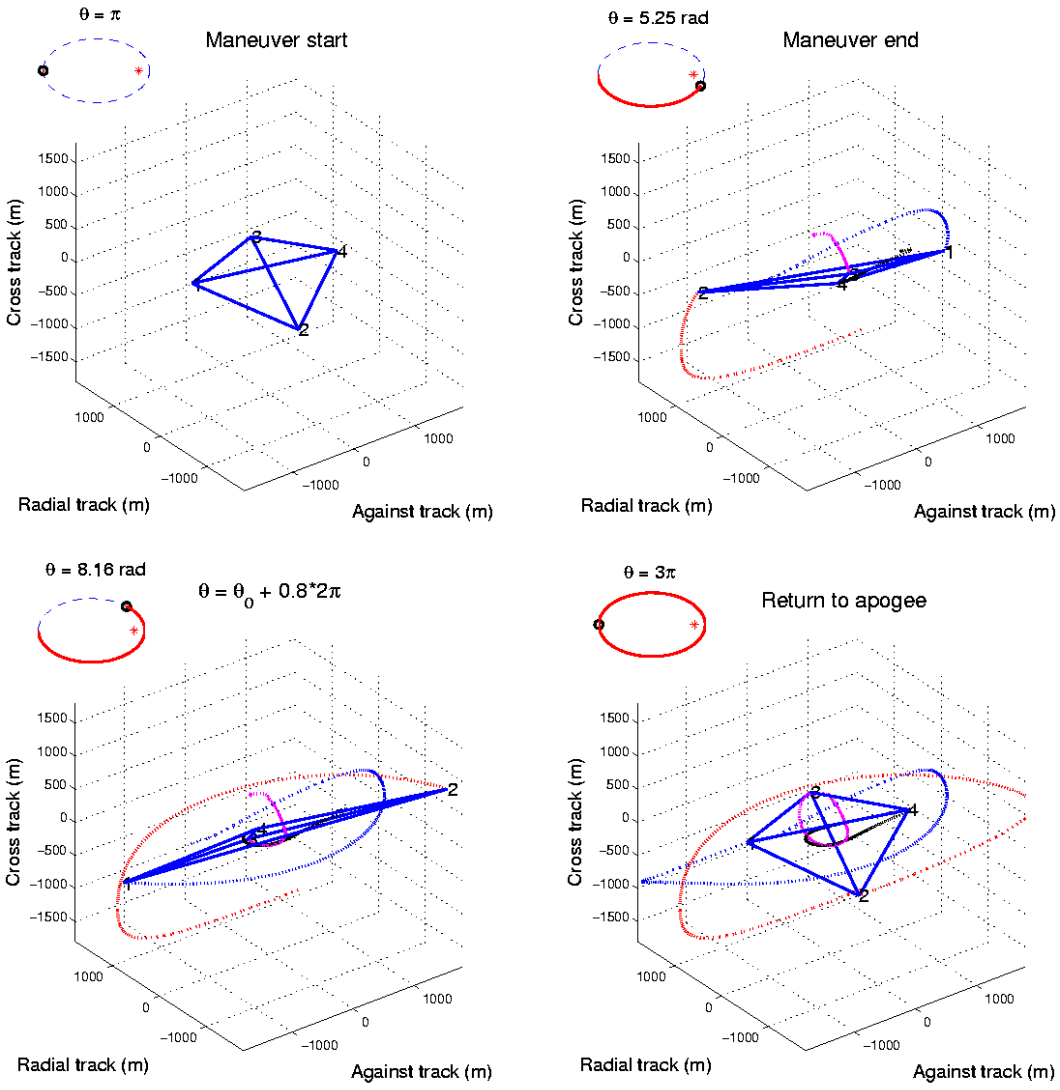

Figure 2.5: The trajectory of a tetrahedral satellite formation change at apogee for eccentricity $e = 0.8$ and reference altitude 12 *Re*. The formation begins in a regular tetrahedron of leg length 1.0 km (top left), proceeds through its series of thrusts (top right), then coasts back to apogee (lower left and right). It ends as a regular tetrahedron of leg length 1.1 km.

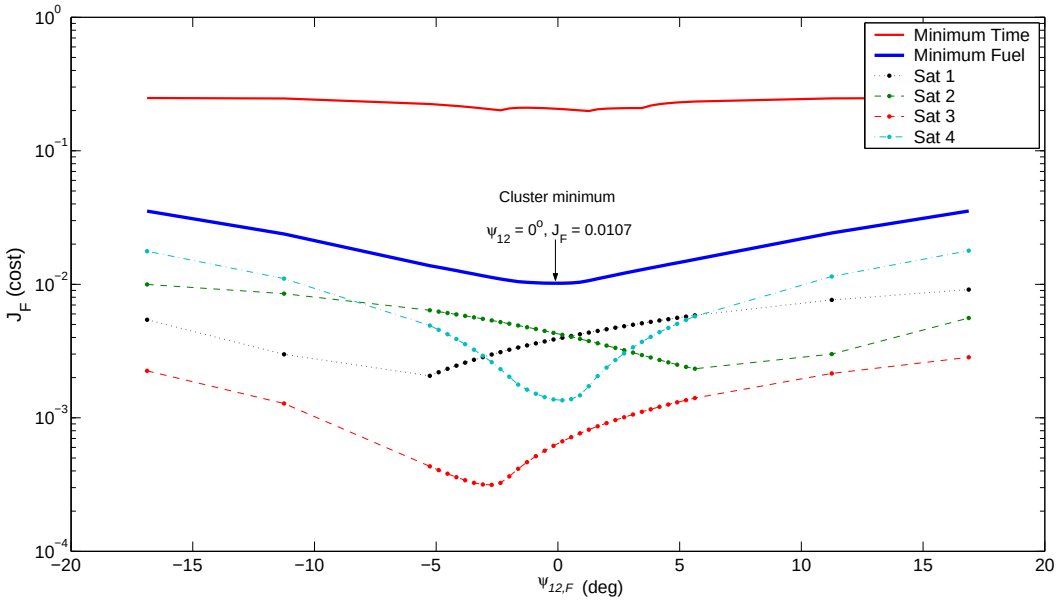

Figure 2.6: Minimum fuel solution with a final maneuver true anomaly of $\theta_F = \theta_0 + 0.92$ orbits for varying final angle ψ_{12} for the example problem. The solid line represents the total cost for all four satellites at each angle, with optimal $\psi_{12,F} = 0°$. Cost increases significantly outside the region shown.

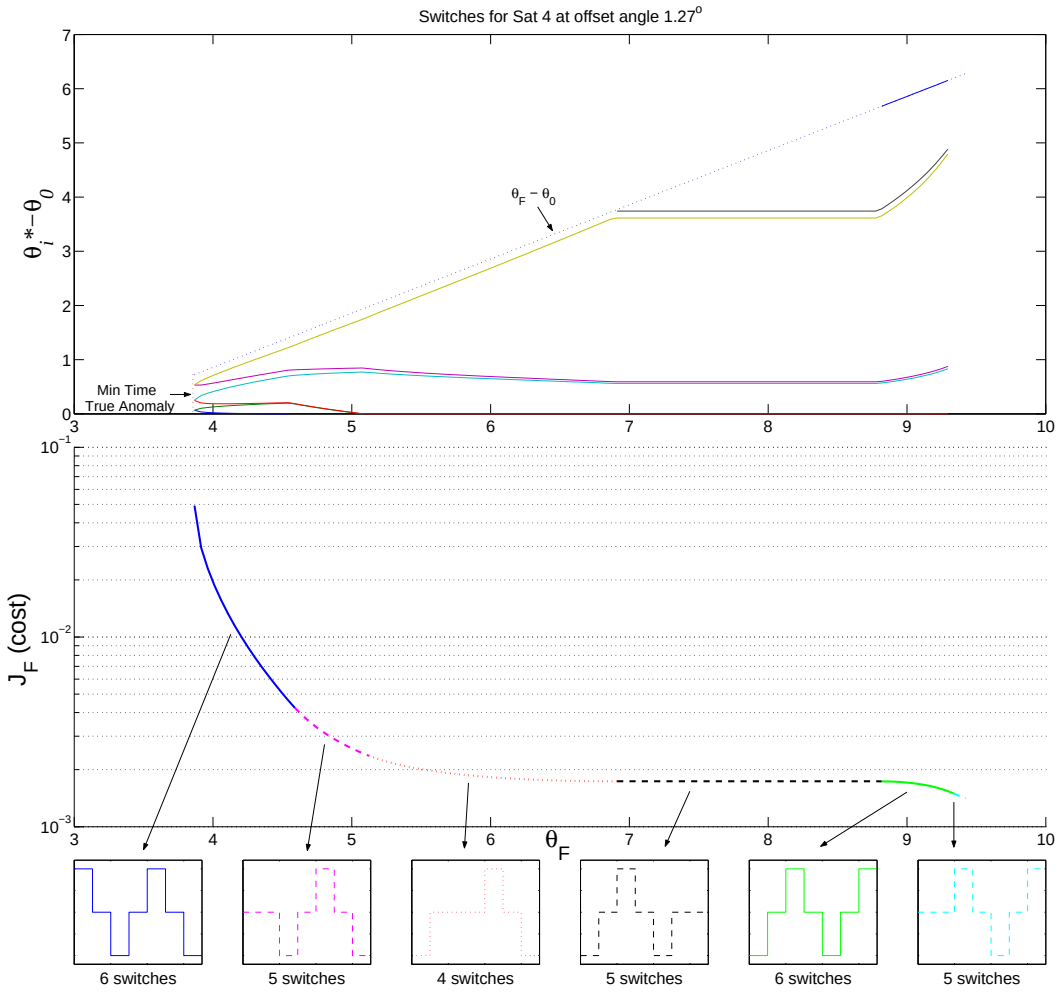

Figure 2.7: The minimum fuel solution varies with θ_F. (*Top*) Individual switches are shown for the fourth satellite at an offset of 1.27°. (*Bottom*) The total fuel cost, along with the corresponding switch profile for each portion of the representation.

though, the fuel cost quickly decreases, indicating that a smart planning methodology can save significant amounts of fuel without requiring a significant time expenditure. As θ_F increases, the thrust traverses a variety of thrust profiles, and the fuel cost is non-increasing with θ_F. In addition, there is continuity between segments in which the thrust profile changes.

Calculation time for this problem is again dependent on the number of samples. The region shown contains 34 points and was generating using a coarse grid of 7 points evenly spaced across the range $\psi_{12} \in [-17^\circ, 17^\circ]$ and a fine mesh of 30 constantly-spaced points for the inner region of $\psi_{12} \in [-5.625, 5.625]$. The initialization strategy employed here considers small variations in the final true anomaly, starting with the minimum-time true anomaly; each point on the fine grid requires less than 30 sec per satellite to solve in MATLAB on a Pentium IV, 1.8 GHz computer. Run in parallel, the formation planner needs ~15 min to complete the optimization. In general, this computation time can be reduced through a more efficient initialization scheme and the use of C/C++ programming. For instance, once one point on the fuel curves is found, all subsequent points can be found by using the previous solution as an initial guess. This approach has worked well in practice in reducing computation time to several seconds per point per satellite.

It is also notable that the solution time is relatively invariant with the number of spline segments. When repeating the above example for cases ranging from 20 to 512 knots, no measurable increase in computation time was found.

2.6.3 Comparison with Linear Programming

The method examined in the previous example is provably optimal for the time varying, linearized state propagation form given in Equation 2.6, and is therefore able to outper-

form any technique relying on discretization in the linear regime. In this section, the performance of the Hamilton-Jacobi-Bellman (HJB) optimization method is compared to linear programming (LP), which has been shown to quickly generate near-optimal solutions for some eccentric orbit problems[23].

The problem shown in Figure 2.7 was solved using an LP in MATLAB. The LP was posed by discretizing the orbit into 1000 points. Identical constraints on thrust (6×10^{-5} N) and final relative position and velocity (10m, 2m/sec) were used for both solution approaches. Note that a final position constraint is used in the HJB solution by selecting the tolerance on the constraint equations (Equations 2.40,2.44, 2.49,2.53).

Simulation results show a 15% fuel savings of the HJB approach compared to that of the linear program. The computational solution times were comparable (several seconds per solution) in both cases. Increasing the number of discretization points to 10,000 points decreases the fuel savings to 10%, indicating that the LP solution is a function of the discretization. This is most evident when the eccentricity is large ($e = 0.8$) and the system matrices are time varying. Computational time in this case increases to tens of seconds for the LP solutions. When the eccentricity for this example is decreased to $e = 0.005$ (the same used in [23]), the LP solutions are 1.5% higher on average than the HJB solutions, indicating that sensitivity to eccentricity is a factor in the LP solutions. Finally, when the constraint on the final position and velocity is increased by a factor of 10 for the $e = 0.8$ case, the average savings in fuel usage for the HJB solutions is 5.4%. If the constraint on the final position and velocity is decreased by a factor of 10, the average fuel savings for the HJB solutions is 33%. In all cases, the LP solutions show "chatter" about the expected switch times, and this chatter increases as higher accuracy in the end point is required. This indicates that the LP solution uses additional thrust (and increasing fuel usage) in an attempt to overcome discretization errors and attain

final end point accuracy.

2.7 Conclusions

A methodology has been described for constructing formation optimal maneuvers for satellites with bounded thrust propulsion based on the Hamilton-Jacobi-Bellman formulation. The technique uses a dynamical model based on normalized time (true anomaly) and employs spline approximations to calculate non-integrable input functions. These approximations allow for relatively fast calculation of single-spacecraft optimal trajectories, which can be solved in parallel across all satellites in the cluster; the single-spacecraft optimal trajectories are then used to determine formation optimal conditions. The theoretical approach can be extended to any system in which a state transition matrix and stable initial state are known and provides an idealized basis to which perturbed closed-loop maneuvers can be compared.

The optimal formation planner was demonstrated and analyzed using a tetrahedral formation, common to several proposed satellite cluster missions. The planar, single satellite minimum time solutions solve for three switch times and a final time; the minimum fuel maneuvers contain 4 to 6 switch times as a function of the final maneuver time. The fuel costs decrease rapidly for small increases in the final maneuver time, and the thrust profile typically acts at or near perigee of the orbit; both conclusions indicate that a smart planner such as the one proposed could save fuel in future formation based missions. Single satellite maneuvers can be calculated in $\approx$5-10 sec, and the full formation planner can be solved in minutes using MATLAB. Because the technique is parallelizable across a cluster, calculation time for the formation optimal planner is well under an orbit for both minimum time and minimum fuel determinations, providing a practical alternative to current finite-horizon techniques. Comparisons with linear pro-

gramming approaches show a definitive savings in fuel for cases of high eccentricity orbits, and strict requirements on end point accuracy.

Acknowledgments

Research funded under the NASA Cross-Enterprise Technology Development Program, NASA Grant # NAG5-10440.

Chapter 3: Formation Planning Optimization for Scientific Objectives in the Magnetospheric Multiscale Mission

Abstract

Hamilton-Jacobi-Bellman optimization is used to evaluate solutions to mixed-metric costs in spacecraft formation maneuver planning which include fuel use, collision avoidance considerations, and scientific effectiveness. Specifically, this mixed-metric cost is explored to determine effective operating regions for the Magnetospheric Multiscale (MMS) mission which maximize mission lifetime while gathering significant data and satisfying collision constraints. A method is presented for quickly finding scientifically useful solutions as well as determining near-optimal transits for problems in which the search space is generally large and single-point solves computationally expensive. Initialization and transits between scientifically useful formations are considered, and parameter combinations which greatly affect achievement of mission objectives are determined. The study indicates different behavior when just one formation step is considered; however, relative weightings of fuel and science cost in the mixed-metric cost function, as well as the resultant parameterization changes, must be regarded carefully when optimization occurs over multiple formation steps. These results can be directly applied to the MMS mission to maximize its scientific benefits.

3.1 Introduction

Multi-spacecraft missions such as Magnetospheric Multiscale mission (MMS)[1] are primarily designed to accomplish scientific objectives at a lower cost than their single-

spacecraft alternatives, but the successful completion of all mission goals is closely linked with lifetime. Exploitation of the natural dynamics of bodies in relative orbits allows for improved scientific data-taking capabilities, while precise planning of formation shapes can reduce the cost of achieving successive tasks. Spacecraft formation maneuvers are frequently considered independent of the overall mission, but a unique and important set of maneuver evaluation techniques can be developed by considering both the formation dynamics and scientific data-taking capabilities.

Both NASA and the Department of Defense have a history of interest in spacecraft formations[3, 4, 17], a trend which promises to continue with the renewed support of MMS[34], a mission whose purpose is to make three-dimensional measurements of the magnetosphere boundary across a broad range of distance scales. Providing the dual benefits of improved data-taking and extended mission life with lower overall launch weight and cost, formations have been suggested for a variety of applications in widely varying orbital regimes, including drift-away solar, Lagrange point, and high-Earth orbits. Many systems-level issues must be addressed before most of these proposals are fully realized, including precise attitude control strategies for multiple-spacecraft formations, communications and fault detection, and formation keeping and maneuvering with limited power and fuel capabilities[34, 36].

In this paper, formation maneuvering is considered in the context of science goals and formation constraints. The goal of the work is to explore the trade-offs between scientific objectives and fuel use as applied to the formation in the MMS mission; both elements are critical to the eventual success of that mission. The first critical step of this problem is the determination of the set of parameters which has the largest influence on mission effectiveness. The next step is to develop a cost function which includes both the science goals and fuel usage, over which an optimization can be performed; the MMS

mission is used as a basis for this optimization, but the approach is generalizable to any high-Earth orbit formation. For this problem, each mission-optimal formation maneuvering solution requires significant computation time, upwards of several minutes per point with current processors. Additionally, the solution may lie in a very large search region with both local and global minima. In order to make the optimization tractable over a large sample space, the search criteria is restricted. To this end, a singular value decomposition is first employed to determine beneficial search directions; next, a multi-path gradient scheme is used to find the minimum. A bisecting line search is employed along multiple search directions. This search is shown to scale well computationally for problems in which cost varies continuously across a search space.

The science-weighted minimum fuel problem has been examined recently by several authors, and different methods have been proposed for analyzing tetrahedron formations. Atkins and Clemente[37] performed a multi-step approach based on a Monte Carlo optimization to find near-optimal formations, but their search is restricted to those formations in which all members are centered about the reference orbit. The work also looks at impulsive solutions to maximize formation viability through active control, but it does not examine constrained thrust propulsion common in formation missions, or the problem of transits between formations. Mailhe and Guzman[38] explored the problem of initialization of a formation after launch, though the work does not discuss the use of scientific objectives in determining the initial formation.

This paper brings together several elements of the MMS mission to construct a cohesive strategy for successfully planning a complex spacecraft formation scenario with intermediate transitions. The text is arranged in three primary sections. First, a relative dynamics model for spacecraft in high Earth orbits is shown, and both single-spacecraft and formation parameterizations are introduced. Optimal planning is also discussed in

relation to these parameterizations, including the conditions required for fuel optimal, constrained thrust solutions. The second section examines scientific costs and develops a means of quantifying formations based on utility towards achieving the mission objectives as well as collision avoidance considerations. A mixed-metric cost function is introduced which incorporates both fuel use and scientific efficacy. A means of searching for parameterizations which provide an extended data-taking period while satisfying formation constraints such as transit times and collision avoidance is then considered. In the final section, a gradient search method is presented which can be used to obtain near-optimal formation maneuvers while minimizing this mixed-metric cost. These formation analysis techniques are then examined using a parametric study for the MMS mission.

3.2 Relative Dynamics Formulations

The motion of a body moving in a gravitational field is described in an inertial reference frame N by the differential equation

$$\ddot{\mathbf{R}}^N(t) = -f(\mathbf{R}^N)\mathbf{R}^N \tag{3.1}$$

where $\mathbf{R}^N$ is the position of the particle with respect to the center of the gravitating body. Writing the derivative of a function with respect to time as $\dot{()}$, a nearby particle with applied thrust $\mathbf{T}^N/m$ will experience a similar effect:

$$\ddot{\mathbf{r}}^N = -f(\mathbf{R}^N)\mathbf{r}^N - \dot{f}(\mathbf{R}^N)\left(\frac{\mathbf{R}^N \cdot \mathbf{r}^N}{|\mathbf{R}^N|}\right)\mathbf{R}^N + \frac{\mathbf{T}^N}{m} \tag{3.2}$$

at distance $\mathbf{r}^N$ from the reference particle. For $\mathbf{r}^N << \mathbf{R}^N$, this equation can be further simplified by writing the elements of $\mathbf{r}^N$ in a reference frame centered about the refer-

ence position $\mathbf{R}^N$. To simplify notation, the vectors in this relative reference frame will be given without superscript. The coordinate axes for a body at the relative position (x_1, x_2, x_3) are defined by the radial vector $\mathbf{R}^N = R\mathbf{x}_2$ and the angular momentum vector $\mathbf{h}^N = h\mathbf{x}_3$, with $R = ||\mathbf{R}^N||$ and $h = ||\mathbf{h}^N||$; $\mathbf{x}_1$ completes the right-handed set.

Dynamics in this frame are readily examined using a set of converted coordinates $(z_1, z_2, z_3)^T$. If the reference particle has angular velocity $\omega(\theta)$ for any true anomaly θ, this converted coordinate set is given by $z^i = \omega(\theta)^{1/2} x_i$, with new positions and velocities

$$\mathbf{z}(\theta) = \begin{pmatrix} z_1 \\ z_1' \\ z_2 \\ z_2' \\ z_3 \\ z_3' \end{pmatrix} = \begin{bmatrix} G(\theta)^{-1} & \mathbf{0}_{2\times2} & \mathbf{0}_{2\times2} \\ \mathbf{0}_{2\times2} & G(\theta)^{-1} & \mathbf{0}_{2\times2} \\ \mathbf{0}_{2\times2} & \mathbf{0}_{2\times2} & G(\theta)^{-1} \end{bmatrix} \begin{pmatrix} x_1 \\ \dot{x}_1 \\ x_2 \\ \dot{x}_2 \\ x_3 \\ \dot{x}_3 \end{pmatrix} = \tilde{F}(\theta)^{-1}\mathbf{x}(\theta, t) \tag{3.3}$$

Here, $(\cdot)'$ denotes differentiation with respect to true anomaly θ. The relative state vector $\mathbf{x}(\theta, t)$ is written explicitly as a function of time to indicate it contains explicit time derivatives, while the vector $\mathbf{z}(\theta)$ does not. The function $G(\theta)$ is given by

$$G(\theta) = \begin{bmatrix} \frac{C}{\rho(\theta)} & 0 \\ C^{-1}e\sin\theta & C^{-1}\rho(\theta) \end{bmatrix} \tag{3.4}$$

with $C^2 = \sqrt{\frac{\mu}{[a(1-e^2)]^3}}$. In these coordinates, the linearized form of Equation 3.2 can be expressed as

$$\mathbf{z}'(\theta) = A(\theta)\mathbf{z}(\theta) + B(\theta)\mathbf{u}(\theta) \tag{3.5}$$

Building on the work of Lawden[39], Carter and Humi[11] solved the unforced system in closed form using the true anomaly θ; Carter extended that solution[12, 13] to remove singularities for circular orbits, recovering the solution to Hill's equation at $e = 0$.

The relative position of the spacecraft at any true anomaly can then be recovered using the equations

$$\mathbf{x}_p = \begin{pmatrix} x_1 \\ x_2 \\ x_3 \end{pmatrix} = \begin{bmatrix} 1 & 0 & 0 & 0 & 0 & 0 \\ 0 & 0 & 1 & 0 & 0 & 0 \\ 0 & 0 & 0 & 0 & 1 & 0 \end{bmatrix} \tilde{F}(\theta)\mathbf{z}(\theta) = F_p(\theta)\mathbf{z}(\theta) \tag{3.6}$$

Likewise, for the relative frame velocities,

$$\dot{\mathbf{x}}_p = \mathbf{x}_v = \begin{pmatrix} \dot{x}_1 \\ \dot{x}_2 \\ \dot{x}_3 \end{pmatrix} = \begin{bmatrix} 0 & 1 & 0 & 0 & 0 & 0 \\ 0 & 0 & 0 & 1 & 0 & 0 \\ 0 & 0 & 0 & 0 & 0 & 1 \end{bmatrix} \tilde{F}(\theta)\mathbf{z}(\theta) = F_v(\theta)\mathbf{z}(\theta) \tag{3.7}$$

This ability to extract position or velocity information will be useful when evaluating the scientific merits of different relative orbits. It will also simplify constraint equations applied to the formations considered in this paper.

In the converted **z** frame, the unforced solution to the linearized relative dynamics equation at any true anomaly θ given an initial condition $\mathbf{z}(\theta_0)$ is derived by Carter[13]; Zanon and Campbell[40] extended that work to the forced solution under a constant thrust, defined as

$$\mathbf{z}(\theta) = \Phi(\theta)\Phi^{-1}(\theta_0)\mathbf{z}(\theta_0) + \Phi(\theta)\mathbf{Q}[\theta_0, \theta] \tag{3.8}$$

where the vector **Q** contains the vector thrust **u**. The values of the fundamental matrix solution $\Phi(\theta)$ and its inverse, as well as the elements of the thrust effect integral **Q** for

fixed thrust directions are given by Zanon and Campbell[41]. This state propagation equation forms the basis for the work presented in the following sections.

3.3 State Parameterizations

Descriptive parameterization of the state of each member of a cluster forms the foundation for determining the mission value of a particular formation. The parameterization is defined here by the set Υ_i, which may contain information relating to any of a number of available state parameterizations. This set also contains formation information, such as the desired motion of each spacecraft in a cluster, which is often dependent on the formation structure and the motions of the other formation elements.

This section describes several important parameterizations for both single spacecraft and formations. While many parameterizations exist, the approach here seeks to develop a parameterization which is the most useful for solving the formation minimum fuel problem with scientific objectives and collision avoidance constraints.

3.3.1 Single-Spacecraft Parameterization Δ

In the most general case, an unforced solution for a satellite with position $\mathbf{x}_p(\theta)$ in the relative reference frame about an eccentric orbit at true anomaly θ can be written as:

$$x_1(\theta) = \frac{p_1}{\rho(\theta)} + \left(\frac{1}{\rho(\theta)} + 1\right)(ep_2\cos\theta + p_3\sin\theta) + 2ep_4\tilde{J}(\theta)\rho(\theta) \tag{3.9}$$

$$x_2(\theta) = p_3\cos\theta - ep_2\sin\theta - p_4\left[\frac{e\cos\theta}{\rho(\theta)^2} - 2e^2\tilde{J}(\theta)\right] \tag{3.10}$$

$$x_3(\theta) = p_5\frac{\sin\theta}{\rho(\theta)} + p_6\frac{\cos\theta}{\rho(\theta)} \tag{3.11}$$

where $\rho(\theta) = 1 + e\cos\theta$ and $\tilde{J}(\theta)$ is given by

$$\tilde{J}(\theta) = \frac{\sin\theta}{\rho(\theta)} - 3e(1-e^2)^{-\frac{5}{2}}\left[\frac{1}{2}\epsilon - \frac{1}{2}\sin\epsilon\cos\epsilon - \frac{e}{3}\sin^3\epsilon\right] \tag{3.12}$$

Here, ϵ is the eccentric anomaly such that

$$\cos\epsilon = \frac{\cos\theta + e}{\rho(\theta)} \sin\epsilon = \frac{\sqrt{1-e^2}\sin\theta}{\rho(\theta)} \tag{3.13}$$

A parameterization for a single spacecraft in a relative reference frame, in this general case, is given by $\mathbf{\Delta} = [p_1, p_2, p_3, p_4, p_5, p_6]$. In the **z**-coordinate frame, the elements of $\mathbf{\Delta}$ can be separated using the fundamental matrix solution $\Phi(\theta)$:

$$\mathbf{z}(\theta) = \Phi(\theta)C^{-1}\begin{bmatrix} -ep_2 \\ -p_3 \\ p_4 - ep_3 \\ p_1 \\ - - -- \\ p_6 \\ p_5 \end{bmatrix} = \Phi(\theta)C^{-1}\begin{bmatrix} \mathbf{p}_{\text{PL}} \\ \mathbf{p}_{\text{CR}} \end{bmatrix} = \Phi(\theta)C^{-1}\mathbf{p} \tag{3.14}$$

The notation $()_{\text{PL}}$ and $()_{\text{CR}}$ are used throughout this chapter to indicate in-plane and cross-axis elements, respectively. In this context, the vector $\mathbf{p}_{\text{PL}} = [-ep_2,\ -p_3,\ p_4 - ep_3,\ p_1]^T$, while $\mathbf{p}_{\text{CR}} = [p_6,\ p_5]^T$.

The $\tilde{J}(\theta)$ term is non-periodic and is therefore associated with a drift that causes the spacecraft to deviate from a repeating planar relative orbit. If only orbits with no drift are considered, $p_4 = 0$ and the equations of motion become

$$x_1(\theta) = \frac{p_1}{\rho(\theta)} + \left(\frac{1}{\rho(\theta)} + 1\right)(ep_2\cos\theta + p_3\sin\theta) \tag{3.15}$$

$$x_2(\theta) = p_3\cos\theta - ep_2\sin\theta \tag{3.16}$$

$$x_3(\theta) = p_5\frac{\sin\theta}{\rho(\theta)} + p_6\frac{\cos\theta}{\rho(\theta)} \tag{3.17}$$

In this case, the *stable* parameter set can be written more compactly as $\mathbf{\Delta}_s = \mathbf{\Delta}||_{p_4=0} = [p_1, p_2, p_3, p_5, p_6]$. This formulation collapses to the Hill's solution for $e = 0$ if θ is additionally treated as a free parameter.

3.3.2 Formation Parameterization for MMS, $\Upsilon_{\mathbf{MMS}}$

The previous subsection provides a parameterization for describing the relative motion of a single spacecraft near a reference orbit. However, this paper is largely concerned with a formation, particularly an MMS-type tetrahedron. While a formation comprised of N_{SC} spacecraft in stable relative orbits can be specified using N_{SC} sets of parameterizations $\mathbf{\Delta}^i$, $i \in \{1, 2, \ldots, N_{\text{SC}}\}$, such a description is not illustrative of the relative motions of elements and, consequently, the utility of the formation. For this reason, it is useful to consider a formation-specific parameter set which both uniquely specifies the single-spacecraft parameterizations Δ^i of all formation elements and provides insight into relevant formation information. It is noted that the general formation parameterization must have $6 \cdot N_{\text{SC}}$ parameters, though formation constraints may reduce the number of free parameters in the system.

For the Magnetospheric Multiscale mission (MMS), the formation parameter set describes a formation with characteristics which include the formation shape and the point in the orbit at which that shape is achieved. In this case, $N_{\text{SC}} = 4$ and the ideal science shape is a tetrahedron. The constraints for this scenario are as follows:

- $\mathbf{x}_p^c$: Formation center parameter [3 constraints]
- $\underline{\mathbf{q}} = [\cos(q_\phi/2), \ \mathbf{q}\sin(q_\phi/2)]$: Formation rotation quaternion [4 constraints]
- θ_C: True anomaly at which regular tetrahedron is defined [1 constraint]
- $\mathbf{x}_p^i(\theta_C), \ i = 1, 2, 3, 4$: Tetrahedron positions [4 constraints]

- $p_4^i,\ i = 1, 2, 3, 4$: Stability parameters [4 constraints]

- $p_1^i, p_5^i,\ i = 1, 2, 3, 4$: Relative orbit centering parameters [8 constraints]

where the superscript i denotes the ith spacecraft in the formation. The vector $\mathbf{x}_p^c$ defines the formation center, and the quaternion $\underline{\mathbf{q}}$ gives a quaternion rotation such that, for the ith spacecraft in the formation, its relative position at the critical true anomaly θ_C is given by:

$$\mathbf{x}_p^i(\theta_C) = \mathbf{q}\bar{\mathbf{x}}_p^i(\theta_C) + \mathbf{x}_p^c \tag{3.18}$$

The positions considered at critical true anomaly θ_C for a tetrahedron such as MMS are shown in Table 3.1, scaled by the nominal tetrahedron leg length L_{tet}; this leg length represents the separation distance between spacecraft at true anomaly $\theta = \theta_C$. With these constraints, the formation parameterization set Υ_{MMS} is then succinctly written as:

$$\Upsilon_{\text{MMS}} = \left\{\mathbf{x}_p^c,\ q_\phi,\ \mathbf{q},\ \theta_C, \left\{\bar{mathbf}{f}x_p^i,\ p_4^i,\ p_1^i,\ p_5^i,\ i = 1, 2, 3, 4\right\}\right\} \tag{3.19}$$

The $6 \cdot 4 = 24$ elements in Υ_{MMS} of Equation 3.19 are not only sufficient to determine the parameterization of all four spacecraft in the tetrahedron, they represent a utilitarian set which will greatly aid the solution of the relative orbit transitions explored throughout this paper. Note the tetrahedron leg length is implicitly contained in the relative position of each spacecraft in the formation. In this way, the actual position of each spacecraft is a function of only elements in the formation parameter set Υ_{MMS}.

Without loss of generality, consider stable relative orbits for which $p_4^i = 0\ \forall\ i$, such that all Δ^i can be reduced to a corresponding set Δ_s^i. All elements of $\Delta_s^i,\ i \in [1, 2, 3, 4]$ can be shown to be fully specified within the set Υ_{MMS}. In this case, given p_1^i and p_5^i for each spacecraft, the parameters p_2^i, p_3^i, and p_6^i can be found algebraically as:

Table 3.1: Nominal tetrahedron positions $\vec{\mathbf{x}}_p^i$ for MMS formation of unit leg length

Normalized Position	SC 1	SC 2	SC 3	SC 4
$\frac{1}{L_{\text{tet}}}\overline{mathbf{x}}_p(\theta_C)$	0	0	$-\frac{1}{2}$	$\frac{1}{2}$
	0	$-\frac{2\sqrt{3}}{3\sqrt{2}}$	$-\frac{2\sqrt{3}}{3\sqrt{2}}$	$-\frac{2\sqrt{3}}{3\sqrt{2}}$
	0	$-\frac{\sqrt{3}}{3}$	$\frac{\sqrt{3}}{6}$	$\frac{\sqrt{3}}{6}$

$$ep_2^i = \frac{\rho(\theta_C)}{\rho(\theta_C)+1}(x_1^i(\theta_C) - \frac{p_1^i}{\rho(\theta_C)})\cos\theta_C - x_2^i(\theta_C)\sin\theta_C \tag{3.20}$$

$$p_3^i = \frac{\rho(\theta_C)}{\rho(\theta_C)+1}(x_1^i(\theta_C) - \frac{p_1^i}{\rho(\theta_C)})\sin\theta_C + x_2^i(\theta_C)\cos\theta_C \tag{3.21}$$

$$p_6^i = \frac{\rho(\theta_C)}{\cos\theta_C}x_3^i(\theta_C) - p_5^i\tan\theta_C \tag{3.22}$$

For non-zero values of p_4^i, these equations are more complex but equally tractable. While the formation parameter set Υ_{MMS} is necessary to solve these equations, showing that any set of single-spacecraft parameterizations can be expressed as a formation parameterization set, the inverse is not always true. In the stable relative orbit case, Equation 3.22 is singular as $\cos\theta_C \to 0$. This singularity can be resolved by noting that, for any given p_5^i, if $\cos\theta_C = 0$, a stable orbit requires that $\rho(\theta_C)x_3^i = p_5^i\sin\theta_C$; so long as this relationship is satisfied, p_6^i can take any value, i.e. p_6^i is actually a free parameter. Equations 3.20 is also not applicable to circular orbits ($e = 0$).

3.4 Optimal Formation Maneuvers

The goal of this paper is to explore the design space for MMS mission objectives using optimization of a maneuver or set of maneuvers. To simplify the discussion in this sec-

tion, the set Υ_{MMS} will be denoted simply as Υ. The optimization for a single formation maneuver is defined as

$$(\Upsilon_0^*, \Upsilon_F^*) = \arg \min_{\Upsilon_0, \Upsilon_F} J_{\text{MMS}}(\Upsilon_0, \Upsilon_F) \tag{3.23}$$

where J_{MMS} is the formation-based cost which can be a function of fuel, time, collision avoidance considerations, and/or the ability of the formation to meet scientific objectives. The notation $()_0$ and $()_F$ denote the formation parameterizations at the start and end of the maneuver, respectively. The optimization is to be performed over a subset of the parameters in Υ_0 and Υ_F, one or both of which may be assumed to be known. In this respect, a series of optimal transitions performed in the sequence $\Upsilon_0 \rightarrow \Upsilon_1 \rightarrow \cdots \rightarrow \Upsilon_F$ can be used to map a complete formation mission from initial to final states, Υ_0 to Υ_F. Therefore, a single maneuver is considered in this section between a general Υ_0 and Υ_F without loss of generality.

The cost function J_{MMS} which is defined and used here is explicitly dependent on fuel use and scientific objectives, as this most accurately captures the needs of the MMS mission. In particular, the objective function explored here is a linear combination of both, or

$$J_{\text{MMS}} = \alpha_{\text{fuel}} J_{\text{fuel}} + \alpha_{\text{sci}} J_{\text{sci}} \tag{3.24}$$

The remainder of this section describes the costs J_{fuel} and J_{sci} individually, while subsequent sections illustrate the use of this metric to evaluate formation maneuvers for transition $\Upsilon_0 \rightarrow \Upsilon_F$.

3.4.1 Fuel Cost

Formation time- and fuel-optimal maneuvers have been discussed in recent literature[42, 43, 44]. The methods described here rely on the strategy originally used by Campbell[9] for spacecraft near a circular orbit and extended to formations about an elliptical reference orbit by Zanon and Campbell[16]. The fuel-optimal formulation can be directly applied to the problem considered here.

For a single spacecraft, the cost function defining fuel use is

$$J^i_{\text{fuel}} = \int_{t_0}^{t_F} |\mathbf{u}^i| \, dt = \int_{\theta_0}^{\theta_F} |\mathbf{u}^i| \sqrt{\frac{a^3}{\mu}} \frac{(1-e^2)^{\frac{3}{2}}}{\rho(\theta)^2} \, d\theta = \int_{\theta_0}^{\theta_F} |\mathbf{u}^i| \omega(\theta)^{-1} \, d\theta \tag{3.25}$$

with $|\cdot|$ denoting the one-norm of the vector. This cost function holds the integrated fuel use over thrusts applied at all true anomalies, and it includes both planar and cross-axis components.

The solution to the single-spacecraft minimum fuel problem is *bang-off-bang*[16], and the planar and cross-axis ω-normalized formation states are dynamically decoupled. Let the maximum thrust available along any axis be given by u. Consider first the planar maneuver beginning at time θ_0 and ending at time θ_F. When completed in under one orbit, the in-plane solution for an optimal transit from initial state $\mathbf{z}^i_{\text{PL}}(\theta_0)$ to final state $\mathbf{z}^i_{\text{PL}}(\theta_F)$ consists of four thrust segments and is defined by six unknown switch times; the solution is therefore coupled with the costate[16]. The vector $\mathbf{z}^i_{\text{PL}}(\theta)$ consists of the first four elements of the vector $\mathbf{z}^i(\theta)$ and has dynamics governed by the upper 4×4 portion of the state transition matrix $\Phi(\theta)$. The state constraints for the minimum fuel problem are given by

$$\mathbf{z}^i_{\mathrm{PL}}(\theta_F) = \Phi_{[1\text{-}4]}(\theta_F)\Phi^{-1}_{[1\text{-}4]}(\theta_0)\mathbf{z}^i_{\mathrm{PL}}(\theta_0) + \Phi_{[1\text{-}4]}(\theta_F)\left(\mathbf{Q}^i_{\mathrm{PL},1}[\theta_0, \theta^*_1]+ \right.$$
$$\left.\mathbf{Q}^i_{\mathrm{PL},2}[\theta^*_2, \theta^*_3] + \mathbf{Q}^i_{\mathrm{PL},3}[\theta^*_4, \theta^*_5] + \mathbf{Q}^i_{\mathrm{PL},4}[\theta^*_6, \theta_F]\right) \tag{3.26}$$

The minimum fuel solution is dependent on the costate (adjoint) of the *z*-coordinate system, defined as

$$\frac{d\boldsymbol{\lambda}^i(\theta)}{d\theta} = -A^T(\theta)\boldsymbol{\lambda}^i(\theta) \tag{3.27}$$

This function can similarly be partitioned into planar and cross-axis dynamics. Simplifying Equation 3.26 using Equation 3.14 and combining it with the costate constraints, the fuel-optimal solution satisfies

$$\mathbf{p}^i_{\mathrm{PL}}(\theta_F) = \mathbf{p}^i_{\mathrm{PL}}(\theta_0) + C\left(\mathbf{Q}^i_{1,\mathrm{PL}}[\theta_0, \theta^{i,*}_{1,\mathrm{PL}}] + \mathbf{Q}^i_{2,\mathrm{PL}}[\theta^{i,*}_{2,\mathrm{PL}}, \theta^{i,*}_{3,\mathrm{PL}}]+ \right.$$
$$\left.\mathbf{Q}^i_{3,\mathrm{PL}}[\theta^{i,*}_{4,\mathrm{PL}}, \theta^{i,*}_{5,\mathrm{PL}}] + \mathbf{Q}^i_{4,\mathrm{PL}}[\theta^{i,*}_{6,\mathrm{PL}}, \theta_F]\right) \tag{3.28}$$

$$\boldsymbol{\lambda}^i_{\mathrm{PL}}(\theta^{i,*}_{j,\mathrm{PL}})^T B_{\mathrm{PL}}(\theta^{i,*}_j) = -sgn((u(\theta^{i,*}_{j,\mathrm{PL}}))\omega(\theta^{i,*}_{j,\mathrm{PL}})^{-1} \quad , \quad j = 1,2,3,4,5,6 \tag{3.29}$$

where $sgn(u(\theta))$ indicates

$$\begin{aligned} u(\theta) &= u \quad \text{for} && \boldsymbol{\lambda}^i_{\mathrm{PL}}(\theta)^T B_{\mathrm{PL}}(\theta) < -\omega(\theta)^{-1} \\ u(\theta) &= 0 \quad \text{for} && -\omega(\theta)^{-1} \le \boldsymbol{\lambda}^i_{\mathrm{PL}}(\theta)^T B_{\mathrm{PL}}(\theta) \le +\omega(\theta)^{-1} \\ u(\theta) &= -u \quad \text{for} && \boldsymbol{\lambda}^i_{\mathrm{PL}}(\theta)^T B_{\mathrm{PL}}(\theta) > +\omega(\theta)^{-1} \end{aligned} \tag{3.30}$$

The cross axis maneuver must also be completed on the same time period $[\theta_0, \theta_F]$ and typically consists of three thrust segments and four unknown thrust switching true anomalies. Dynamics in the cross axis act along the final two elements of the vector $\mathbf{z}^i(\theta)$ through the lower right 2×2 portion of the matrix $\Phi(\theta)$. The sequence is again found through the costate by the equations

$$\mathbf{z}^i_{\mathrm{CR}}(\theta_F) = \Phi_{[5\text{-}6]}(\theta_F)\Phi^{-1}_{[5\text{-}6]}(\theta_0)\mathbf{z}^i_{\mathrm{CR}}(\theta_0) + \Phi_{[5\text{-}6]}(\theta_F) \times \left(\mathbf{Q}^i_{1,\mathrm{CR}}[\theta^{i,*}_{1,\mathrm{CR}}, \theta^{i,*}_{2,\mathrm{CR}}] + \mathbf{Q}^i_{2,\mathrm{CR}}[\theta^{i,*}_{3,\mathrm{CR}}, \theta^{i,*}_{4,\mathrm{CR}}]\right) \quad (3.31)$$

$$\boldsymbol{\lambda}^i_{\mathrm{CR}}(\theta^{i,*}_{j,\mathrm{CR}})^T B_{\mathrm{CR}}(\theta^{i,*}_{j,\mathrm{CR}}) = -sgn(u(\theta)^{i,*}_{j,\mathrm{CR}}))\omega(\theta^{i,*}_{j,\mathrm{CR}})^{-1} \quad , \quad j = 1,2,3,4 \quad (3.32)$$

Using Equation 3.14, the simplified set of constraints is:

$$\mathbf{p}^i_{\mathrm{CR}}(\theta_F) = \mathbf{p}^i_{\mathrm{CR}}(\theta_0) + C\left(\mathbf{Q}^i_{1,\mathrm{CR}}[\theta^{i,*}_{1,CR}, \theta^*_{2,CR}] + \mathbf{Q}^i_{2,\mathrm{CR}}[\theta^*_{3,CR}, \theta^*_{4,CR}]\right) \quad (3.33)$$

$$\boldsymbol{\lambda}^i_{\mathrm{CR}}(\theta^{i,*}_{j,CR})^T B_{\mathrm{CR}}(\theta^*_{i,CR}) = -sgn(u(\theta^{i,*}_{j,CR}))\omega(\theta^{i,*}_{j,CR})^{-1} \quad , \quad j = 1,2,3,4 \quad (3.34)$$

The total MMS fuel cost to make the transit $\boldsymbol{\Upsilon}_0 \rightarrow \boldsymbol{\Upsilon}_F$ can be readily determined using the sum of the single-spacecraft fuel costs over the four elements in the MMS cluster. Assuming thrust control switches at $\theta^{i,*}_0$, for the ith spacecraft, the single-spacecraft cost is

$$\begin{aligned} J^i_{\mathrm{fuel}}(\boldsymbol{\Delta}^i_{s,0}, \boldsymbol{\Delta}^i_{s,F}) = u\Big\{&\left[\omega(\theta^{i,*}_{1,\mathrm{PL}})^{-1} - \omega(\theta_0)^{-1}\right] + \left[\omega(\theta^{i,*}_{3,\mathrm{PL}})^{-1} - \omega(\theta^{i,*}_{2,\mathrm{PL}})^{-1}\right] + \\ &\left[\omega(\theta^{i,*}_{5,\mathrm{PL}})^{-1} - \omega(\theta^{i,*}_{4,\mathrm{PL}})^{-1}\right] + \left[\omega(\theta_F)^{-1} - \omega(\theta^{i,*}_{6,\mathrm{PL}})^{-1}\right] + \\ &\left[\omega(\theta^{i,*}_{2,CR})^{-1} - \omega(\theta^{i,*}_{1,CR})^{-1}\right] + \left[\omega(\theta^{i,*}_{4,CR})^{-1} - \omega(\theta^{i,*}_{3,CR})^{-1}\right]\Big\} \end{aligned} \quad (3.35)$$

The total formation cost J_{fuel} for the $N_{\mathrm{SC}} = 4$ MMS tetrahedron is then:

$$J_{\mathrm{fuel}}(\boldsymbol{\Upsilon}_0, \boldsymbol{\Upsilon}_F) = \sum_{i=1}^{4} J^i_{\mathrm{fuel}}(\boldsymbol{\Delta}^i_{s,0}, \boldsymbol{\Delta}^i_{s,F}) \quad (3.36)$$

Note that J_{fuel} on the left-hand side is explicitly a function of $\boldsymbol{\Upsilon}_0$ and $\boldsymbol{\Upsilon}_F$, indicating it is the formation fuel cost, whereas each J^i_{fuel} on the right-hand side is explicitly a function of $\boldsymbol{\Delta}^i_{s,0}$ and $\boldsymbol{\Delta}^i_{s,F}$, whose elements are determined by the elements of the sets $\boldsymbol{\Upsilon}_0$ and $\boldsymbol{\Upsilon}_F$, respectively.

3.4.2 Scientific Cost

Evaluating the possibility for achieving scientific objectives in the MMS mission is challenging, but several methods have been put forward to accomplish the task[46]. The primary considerations in the selection of a particular metric are its ability to capture the desired property of the tetrahedron in a meaningful way and its computational ease of implementation. Several potential science metrics, or quality factors, have been put forward, including the Robert-Roux parameter, the fractional geometric parameter, and the Glassmeier parameter. The Robert-Roux parameter relates the volume of the tetrahedron to the volume of the sphere circumscribing the four vertices[46] and is the most commonly explored parameter for tetrahedron formations[37, 40]. The Glassmeier parameter compares the volume and surface area of a tetrahedron with that of a regular tetrahedron of the same average leg length, but it has not been significantly used because it is offers similar information to both the Robert-Roux and geometric quality factors at greater computational expense. Each of these parameters is intended to evaluate how closely the formation resembles a regular tetrahedron with equal leg lengths by encompassing both the true leg lengths and three-dimensionality in a single value; however, these parameters do not indicate the size of the resultant tetrahedron. The MMS mission designers propose to use the fractional geometric quality factor — denoted with the subscript $R8$ — which takes on values similar to the Robert-Roux quality factor but is the least computationally intensive of the three. For formation flying missions in which the relative distance between formation elements is small, collision avoidance is also of concern, and both the Robert-Roux parameter and the fractional geometric quality factor can be readily employed in the presence of collision avoidance constraints, since both are a function of inter-spacecraft distance.

The nominal fractional geometric quality factor describing a tetrahedron is[46]:

$$Q_{R8} = \frac{V_{\text{tet}}}{V_{\text{ideal}}} \tag{3.37}$$

where V_{ideal} is the volume of a regular tetrahedron with leg length equal to the mean of the leg lengths of the true tetrahedron, $\bar{L}$. The true tetrahedron cannot encompass a volume greater than the ideal tetrahedron, so the quality factor $0 \leq Q_{R8} \leq 1$. Figure 3.1 shows the relationship between the true and ideal tetrahedron volume for one example and highlights the important system elements for the computation of the fractional geometric parameter.

In order to evaluate Q_{R8}, first let the vector from the ith to the jth spacecraft in the formation at true anomaly θ be denoted by $\mathbf{x}^{ij}(\theta)$. Without loss of generality, both V_{tet} and V_{ideal} can be evaluated by selecting the formation origin to be coincident with the location of Spacecraft 1, $\mathbf{x}_p^1$. The true tetrahedron is a fundamental structure, and its volume is mathematically simple to calculate as the scalar triple product of the three vectors from this origin to each of the other spacecraft:

$$V_{\text{tet}} = \frac{1}{6}\left\{\mathbf{x}^{41}(\theta) \cdot \left[\mathbf{x}^{31}(\theta) \times \mathbf{x}^{21}(\theta)\right]\right\} \tag{3.38}$$

The volume of a regular tetrahedron with each leg length equal to the mean of the leg lengths of the true tetrahedron is also computationally simple to derive. Denoting this mean leg length $\bar{L}$, the mean leg length of the originating tetrahedron can be computed as 1/6 the sum of all inter-spacecraft distances. For any two spacecraft i and j in the formation, let $d^{ij}(\theta) = \|\mathbf{x}^i(\theta) - \mathbf{x}^j(\theta)\| = \|\mathbf{x}^{ij}(\theta)\|$ be the separation distance. The mean leg length is then

$$\bar{L}(\theta) = \frac{1}{6}\sum_{i=2}^{4}\sum_{j=1}^{i-1} d^{ij}(\theta) \tag{3.39}$$

The ideal tetrahedron has a volume related only to this leg length:

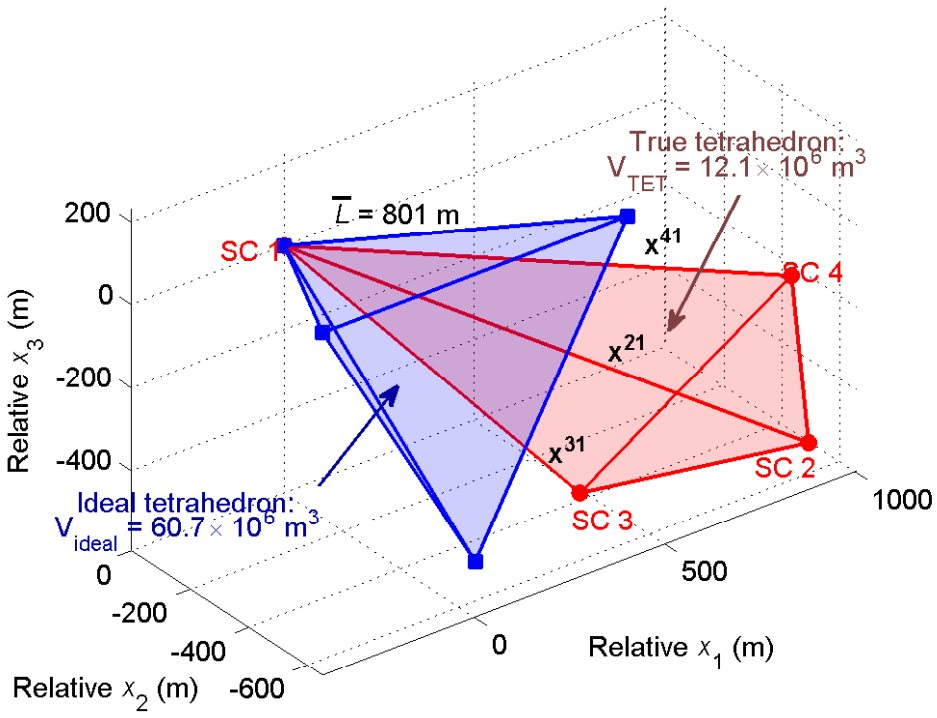

Figure 3.1: Illustration of the elements for computing the fractional geometric parameter. The true tetrahedron has the four spacecraft at its corners; the ideal tetrahedron is a regular tetrahedron of leg length $\bar{L}$. The ideal tetrahedron represents the largest volume that can be encompassed by a tetrahedron of that average leg length, such that $0 \leq Q_{R8} \leq 1$.

$$V_{\text{ideal}} = \frac{\sqrt{2}}{12}\bar{L}^3 = \frac{\sqrt{2}}{2592}\left[\sum_{i=2}^{4}\sum_{j=1}^{i-1} d^{ij}(\theta)\right]^3 \tag{3.40}$$

Combining Equations 3.38 and 3.40 for the true and ideal tetrahedron volumes, the fractional geometric factor is

$$Q_{R8} = \frac{432\ \mathbf{x}^{41}(\theta)\cdot\left[\mathbf{x}^{31}(\theta)\times\mathbf{x}^{21}(\theta)\right]}{\sqrt{2}\ \left[\sum_{i=2}^{4}\sum_{j=1}^{i-1} d^{ij}(\theta)\right]^3} \tag{3.41}$$

Note that this calculation has extremely low computational demands if the positions $\mathbf{x}^i(\theta)$, $i \in [1,2,3,4]$ are known. Such simplicity makes this metric highly useful for intensive analysis of the data-taking capabilities of a variety of formation parameterizations over an orbit.

While relevant to the MMS science objectives, the Q_{R8} parameter is defined only at a single point in the orbit; evaluation of formation capabilities, however, requires that this information be computed over the full orbit. To further evaluate the scientific efficacy of a parameterization Υ_{MMS} for the problem considered here, two additional considerations must be made. First, only those true anomalies θ at which the formation has a high quality factor, defined by $\tau \leq Q_{R8}(\theta) \leq 1$, are considered valuable data-taking points; this establishes a minimum threshold τ at which viable science data can be obtained. For MMS-like missions, τ is generally $\sim 0.6 - 0.7$. Second, a true anomaly $\theta = \theta_D$ is established which represents the point about which the most relevant science data is taken. Scientifically, this data-taking true anomaly $\theta = \theta_D$ lies within the *data-taking window*, given as the continuous set $\Theta_D = [\theta_D - \delta\theta_D^-, \theta_D + \delta\theta_D^+]$ *and* $Q_{R8}(\theta) \geq \tau \ \ \forall \ \ \theta \in \Theta_D$. For the subsequent optimization, a modified fractional geometric parameter can now be defined which encompasses both of these limits:

$$\tilde{Q}_{R8}(\theta) = \begin{cases} Q_{R8} & \text{for} \quad \theta \in \Theta_D \quad (Q_{R8} \geq \tau) \\ 0 & \text{for} \quad \theta \notin \Theta_D \quad (Q_{R8} < \tau) \end{cases} \tag{3.42}$$

Generally, τ is a mission-dependent threshold which incorporates communication and data-taking constraints. This represents a moderately well-defined tetrahedron for which reasonable magnetic field measurements can be easily resolved. For most formations, the values of $\delta\theta_D^-$ and $\delta\theta_D^+$ cannot be determined *a priori* but must be computed by determining $Q_{R8}(\theta)$ over a range of true anomalies about the desired data-taking true anomaly θ_D. Note that $\delta\theta_D^-$ and $\delta\theta_D^+$ are not symmetric about data-taking true anomaly θ_D unless centering parameter $p_1^i = 0, \ i \in [1, 2, 3, 4]$. Because this paper considers non-zero centering parameters, the more general formulation is retained.

The science cost is defined as an integrated average of the unforced, modified quality factor $\tilde{Q}_{R8}$ as it varies over one full orbit for the formation Υ_{MMS}:

$$J_{\text{sci}}(\Upsilon_{\text{MMS}}) = \frac{1}{P}\int_0^P \tilde{Q}_{R8}(\Upsilon_{\text{MMS}}, t)\, dt = \frac{1}{P}\int_{t(\theta_D - \delta\theta^-)}^{t(\theta_D + \delta\theta^+)} Q_{R8}(\Upsilon_{\text{MMS}}, t)\, dt \tag{3.43}$$

where P is the orbital period. Note that the integration is with respect to time rather than true anomaly, which accounts for the expression of both the limits of the data-taking window and the quality factor $\tilde{Q}_{R8}$ as functions of time. It is clear that maximizing the total *time* of the data-taking window depends on minimizing the relative spacecraft motion normal to the vector displacement of each spacecraft with respect to the formation center at data-taking true anomaly θ_D. Relative formation parameterizations which minimize this variation will typically provide optimal unforced relative orbits for data-taking.

The science cost J_{sci} given in Equation 3.43 assumes that $\tilde{Q}_{R8}(\Upsilon_{\text{MMS}}, \theta)$ is integrable on the orbit. However, the integral has no general closed-form solution, and the limits

of integration are, as noted previously, typically not known *a priori*. The science cost function must therefore be approximated numerically. Due to the discontinuity in Q_{R8} (Equation 3.42), this approximation is best performed by discretizing the orbital period P into m equal-time segments and linearly extrapolating based on the quality factor at each endpoint:

$$J_{\text{sci}}(\Upsilon) \approx \frac{1}{P} \sum_{j=1}^{m} \tilde{Q}_{R8}(\Upsilon_{\text{MMS}}, t_j) \Delta t \tag{3.44}$$

where $\Delta t = \frac{P}{m}$ and $t_j = t_{\theta_D - \delta\theta_D^-} + j\Delta t$. The true anomaly $\theta = \theta_j$ corresponds to time t_j and solves Kepler's equation at that point. As $m \to \infty$, Equation 3.44 approaches the integral science cost from Equation 3.43. Higher-order approximation techniques could also be used to calculate J_{sci}, at the cost of additional computation time. For most evaluations, Equation 3.44 is sufficient, though a higher-order interpolation is useful to determine the appropriate Δt as $Q_{R8} \to \tau$; this ensures that J_{sci} is not significantly overestimated if the quality factor varies sharply near this value. In this paper, the linear approximation in Equation 3.44 is used for the general cost function, and a fourth-order interpolation is used to determine the crossing time for $Q_{R8} = \tau$.

A final constraint is now imposed on the scientific cost in order to ensure that data can be taken for a minimum region about the desired data-taking true anomaly $\theta = \theta_D$. The constraint parameter $\delta\theta_{\text{sci}}$ and its corresponding set Θ_{sci} are introduced to determine whether a formation is *scientifically viable*:

$$\Theta_{\text{sci}} \equiv \theta \in [\theta_D - \delta\theta_{\text{sci}}, \theta_D + \delta\theta_{\text{sci}}] \equiv \Theta_{\text{sci}} \tag{3.45}$$

A scientifically viable formation is one for which $Q_{R8}(\theta) \geq \tau \ \forall \ \theta \ \in \ \Theta_{\text{sci}}$, such that $\Theta_{\text{sci}} \subset \Theta_D$. Note that, unlike the data-taking window, Θ_{sci} is symmetric about θ_D and is chosen by mission designers. Figure 3.2 illustrates the relationships between these

parameters for a viable formation. At the critical true anomaly $\theta = \theta_C$, $Q_{R8} \equiv 1$. For all points in Θ_{sci} — indicated by the desired data-taking true anomaly θ_D and windowing parameter $\delta\theta_{\text{sci}}$, $Q_{R8} \geq \tau$. The data-taking window Θ is also indicated in magenta for this formation.

3.4.3 Relative Spacecraft Constraints

Two additional constraints must be employed to complete the description of the efficacy of a formation for satisfying mission goals. These constraints are both on the distance between any two adjacent spacecraft in the formation, $d^{ij}(\theta) = \|\mathbf{x}^i(\theta) - \mathbf{x}^j(\theta)\| = \|\mathbf{x}^{ij}(\theta)\|$, $i \neq j$:

- d_{max}: The maximum separation distance between spacecraft for which data can be taken. For all true anomalies θ considered in the science cost J_{sci}, no two spacecraft may be separated by more than d_{max}. Formally, $d^{ij}(\theta) \leq d_{\text{max}}$ $\forall$ $\theta \in \Theta_{\text{sci}}$ and $\forall$ $(i, j) \in \{1, 2, 3, 4\}$. The maximum separation distance is typically 2-3 times the formation's nominal leg length L_{tet} and is chosen to ensure that only science data taken on a relevant scale be included in the science cost.

- d_{min}: The minimum separation distance allowed between spacecraft during data-taking. The constraint associated with this distance is $d^{ij}(\theta) > d_{\text{min}}$ $\forall$ $(i, j) \in \{1, 2, 3, 4\}$. at every true anomaly θ. For the problems considered here, violation of this constraint indicates solutions that pose a collision avoidance risk to the spacecraft and invalidates the viability of a formation.

Calculation of the six interspacecraft distances $d^{ij}(\theta)$ is one component of the calculation of J_{sci} at any true anomaly θ; thus, the relative spacecraft separation distance constraints are evaluated at each true anomaly used to compute the science cost function

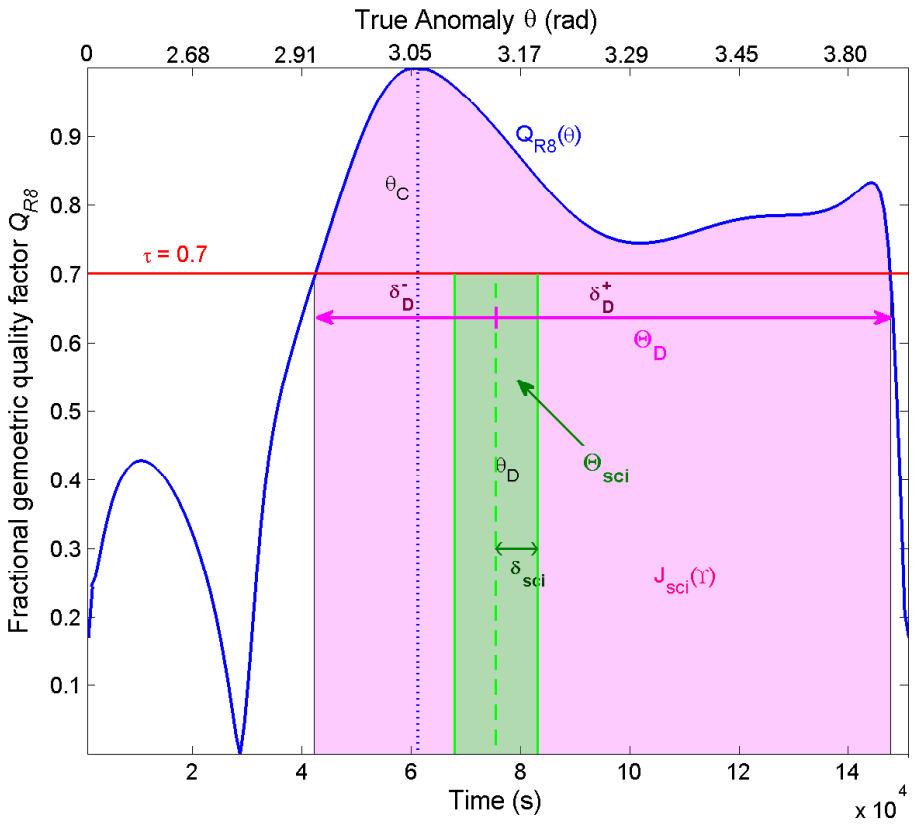

Figure 3.2: Quality factor Q_{R8} as a function of true anomaly and time for a formation about reference orbit $a = 61230.144$, $e = 0.875$. By definition, $Q_{R8} = 1$ at $\theta = \theta_C$ (blue vertical dotted line). The data-taking window $\Theta_D = [\theta_D - \delta\theta_D^-, \theta_D + \delta\theta_D^+]$ (magenta) is defined as the region about $\theta = \theta_D$ for which $Q_{R8} > \tau$, where $\tau = 0.7$ is the user-defined data-taking minimum (red horizontal line). The science cost $J_{\text{sci}}(\Upsilon_{\text{MMS}})$ is the integrated area over this region (shaded). In order for the formation to be viable, $\Theta_{\text{sci}} = [\theta_D - \delta\theta_{\text{sci}}, \theta_D + \delta\theta_{\text{sci}}] \subset \Theta_D$. Here, $\theta_D = \pi$ and $\delta\theta_{\text{sci}} = \pi/72$.

J_{sci}. Also, because relative orbits for eccentricities of $e \lesssim 0.9$ are subject to generally slow dynamics, it is sufficient to ensure that these constraints are satisfied at all evaluated points; interpolation between points is not normally necessary, as long as the step size $\Delta t \lesssim 0.01P$.

It is important to note that the constraints d_{min}, θ_D, and $\delta\theta_{\text{sci}}$ primarily determine whether a particular formation is viable for data-taking. On the other hand, the constraints τ and d_{max} primarily affect the magnitude of the science cost J_{sci}, though they can also play a role in determining viability. As an example, consider Figure 3.3. Here, $J_{\text{MMS}} = -J_{\text{sci}}$ is plotted for a formation with central parameterization $\Upsilon_{\text{MMS}}(0,0)$ for variations in the chosen value of the centering parameter p_1^4 along the horizontal axis and variations in centering parameter p_1^2 and p_1^3, with the constraint that $\delta p_{1,2} = -\delta p_{1,3}$, along the vertical axis; all other parameters in Υ_{MMS} are fixed. Constraints $\tau = 0.7$ and $d_{\text{max}} = 1000$m are fixed, as is the data-taking true anomaly $\theta_D = \pi$. The underlying cost J_{MMS} exhibits typical variations over the two-dimensional parametric free space in Υ_{MMS} for $\delta\theta_{\text{sci}} = \pi/72$ and minimum separation distance $d_{\text{min}} \leq 380$m. This is a typical and simplistic constrained formation scenario in which mission designers might explore the ability of the dynamics near $\theta = \theta_C$ to increase data-taking window through an increased separation distance of Spacecraft 2 and Spacecraft 3 near that critical true anomaly. As d_{min} increases, the viable region shrinks (vertical gray lines), in this case excluding the center region on the plot as viable formations until only small regions with large positive and negative variations in p_1^4 remain. Conversely, as $\delta\theta_{\text{sci}}$ increases (magenta lines), the outer sections of the plot are no longer viable. If the two vary in tandem, only those portions of the formation cost plot contained in the intersection of these smaller viable regions will be viable, such that for $\delta\theta_{\text{sci}} = \pi/24$ and $d_{\text{min}} = 420$m, the entire search space has been excluded from consideration. This sensitivity over a relatively small

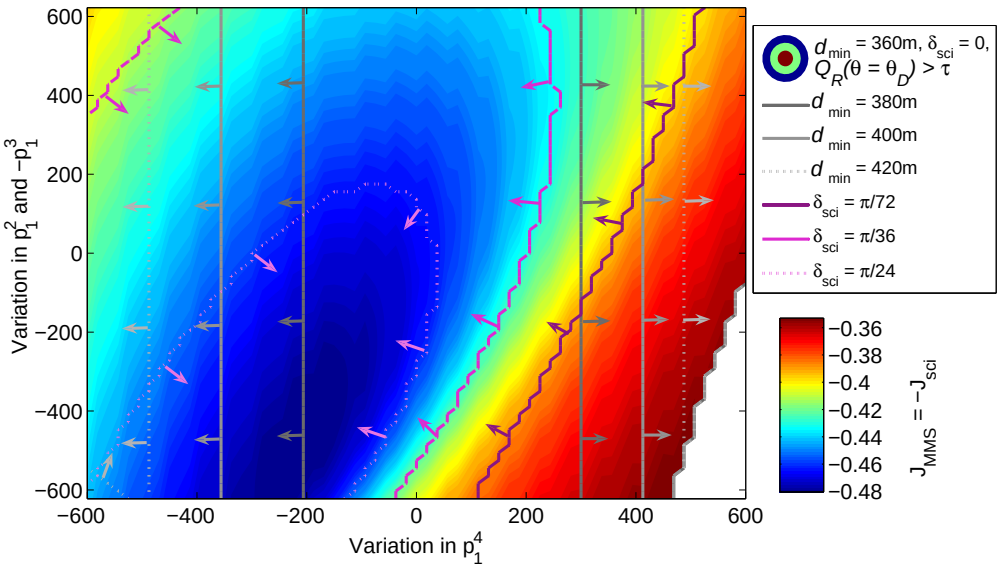

Figure 3.3: Contour plot of science cost $J_{\text{MMS}} = -J_{\text{sci}}$ for variations along two parametric directions, and the effect of $\delta\theta_{\text{sci}}$ and d_{min} on the viability of those costs. The gray enclosures show the viable regions for each value of d_{min}; magenta enclosures show viability along $\delta\theta_{\text{sci}}$; and arrows indicate which portion of the region is viable. Viable regions for increasing d_{min} begin to exclude the center, while viable regions for increasing $\delta\theta_{\text{sci}}$ exclude the edges. Formations of greatest scientific interest — and lowest formation cost — are in dark blue.

change in these constraint parameters highlights the importance of properly selecting the constraints based on mission requirements, and shows the trade-offs designers must make to maximize mission performance while minimizing risk.

3.4.4 Mixed Cost of Science and Fuel

The total cost for MMS formation maneuvers considered here can now be described as a combination of the fuel and scientific data-taking costs. The simplest cost function is

given by a linear combination of these. However, for formation maneuvers intended to initialize a formation, both the initial and final formations have an associated cost. The resultant general formulation allows each of these an independent weight:

$$J_{\text{MMS}}(\boldsymbol{\Upsilon}_0, \boldsymbol{\Upsilon}_F) = \alpha_{\text{fuel}} J_{\text{fuel}}(\boldsymbol{\Upsilon}_0, \boldsymbol{\Upsilon}_F) + \alpha_{\text{sci},0} J_{\text{sci}}(\boldsymbol{\Upsilon}_0) + \alpha_{\text{sci},F} J_{\text{sci}}(\boldsymbol{\Upsilon}_F) \tag{3.46}$$

Because the magnitudes of fuel cost and science cost differ, the relation $1/P$ for the scientific formulation can be readily drawn into the parameters $\alpha_{\text{sci},0}$ and $\alpha_{\text{sci},F}$ to yield

$$\begin{aligned} J_{\text{MMS}}(\boldsymbol{\Upsilon}_0, \boldsymbol{\Upsilon}_F) \quad = \quad & \alpha_{\text{fuel}} \left[\sum_{i=1}^{4} J^i_{\text{fuel}}(\boldsymbol{\Delta}^i_{s,0}, \boldsymbol{\Delta}^i_{s,F}) \right] + \\ & \alpha_{\text{sci},0} \left[\sum_{j=1}^{m} \tilde{Q}_{R8}(\boldsymbol{\Upsilon}_0, t_j) \Delta t \right] + \alpha_{\text{sci},F} \left[\sum_{j=1}^{m} \tilde{Q}_{R8}(\boldsymbol{\Upsilon}_F, t_j) \Delta t \right] \end{aligned} \tag{3.47}$$

In general, $\alpha_{\text{fuel},0}$ and $\alpha_{\text{fuel},F}$ are negative values, reflecting the benefits of a large science cost J_{sci} and the desire to *minimize* the value of the formation cost function J_{MMS}. For ease of comparison, the formation cost function can be compacted using the vector $\boldsymbol{\alpha}$ which defines the multiplying parameters contained in Equation 3.47 in the form $\boldsymbol{\alpha}_{\text{MMS}} = [\alpha_{\text{fuel}}, \alpha_{\text{sci},0}, \alpha_{\text{sci},F}]$. The formation cost is then simply

$$J_{\text{MMS}}(\boldsymbol{\Upsilon}_0, \boldsymbol{\Upsilon}_F) = \boldsymbol{\alpha}_{\text{MMS}} \begin{bmatrix} \sum_{i=1}^{4} J_{\text{fuel}}(\boldsymbol{\Delta}^i_{s,0}, \boldsymbol{\Delta}^i_{s,F}) \\ \sum_{j=1}^{m} \tilde{Q}_{R8}(\boldsymbol{\Upsilon}_0, t_j) \Delta t \\ \sum_{j=1}^{m} \tilde{Q}_{R8}(\boldsymbol{\Upsilon}_F, t_j) \Delta t \end{bmatrix} \tag{3.48}$$

The selection of an optimal formation transition is then dictated by the parameter sets $\{\boldsymbol{\Upsilon}_0, \boldsymbol{\Upsilon}_F\}$.

It is noted that these formation parameterizations can be further partitioned for a problem in which some elements are fixed and others are free as

$$\boldsymbol{\Upsilon}_0 = \{\boldsymbol{\Upsilon}_{\text{fixed},0} | \boldsymbol{\Upsilon}_{\text{free},0}\} \tag{3.49}$$

$$\boldsymbol{\Upsilon}_F = \{\boldsymbol{\Upsilon}_{\text{fixed},F} | \boldsymbol{\Upsilon}_{\text{free},F}\} \tag{3.50}$$

Selecting from among only the free parameters in the set, the problem is then cast as

$$\{\boldsymbol{\Upsilon}^*_{\text{free},0}, \boldsymbol{\Upsilon}^*_{\text{free},F}\} = \underset{\boldsymbol{\Upsilon}_{\text{free},0}, \boldsymbol{\Upsilon}_{\text{free},F}}{\text{argmin}} \left(\boldsymbol{\alpha}_{\text{MMS}} \begin{bmatrix} \sum_{i=1}^{4} J_{\text{fuel}}(\boldsymbol{\Delta}^i_{s,0}, \boldsymbol{\Delta}^i_{s,F}) \\ \sum_{j=1}^{m} \tilde{Q}_{R8}(\boldsymbol{\Upsilon}_0, t_j)\Delta t \\ \sum_{j=1}^{m} \tilde{Q}_{R8}(\boldsymbol{\Upsilon}_F, t_j)\Delta t \end{bmatrix} \right)$$

subject to:

$$\begin{aligned} d^{ij}(\theta) &\leq d_{\max} \; \forall \; i \neq j, \; (i, j) \in \{1, 2, 3, 4\}, \; \theta \in \Theta_D \\ d^{ij}(\theta) &> d_{\min} \; \forall \; i \neq j, \; (i, j) \in \{1, 2, 3, 4\} \\ Q_{R8}(\theta) &\geq \tau \; \forall \; \theta \in \Theta_{\text{sci}} \end{aligned} \tag{3.51}$$

This optimization trades the formation fuel cost and the scientific mission cost for both the initial and final formations.

The examples presented in this paper set $\alpha_{\text{sci},0} = 0$, optimizing only over the final parameterization for a known initial parameterization. This more accurately captures the MMS mission objectives, in which each formation maneuver results in a formation separation at which data-taking will occur. For this case, the weighting $\boldsymbol{\alpha}_{\text{MMS}}$ given in Equation 3.51 can be reduced to the simpler form $\boldsymbol{\alpha} = [\alpha_{\text{fuel}}, \alpha_{\text{sci},F}] \equiv [\alpha_{\text{fuel}}, \alpha_{\text{sci}}]$, and the formation optimization problem becomes

$$
\begin{aligned}
\boldsymbol{\Upsilon}^{*}_{\text{free}} &= \underset{\boldsymbol{\Upsilon}_{\text{free},F}}{\text{argmin}} \left(\boldsymbol{\alpha} \begin{bmatrix} \sum_{i=1}^{4} J_{\text{fuel}}(\boldsymbol{\Delta}_0^{s,i}, \boldsymbol{\Delta}_F^{s,i}) \\ \sum_{j=1}^{m} \tilde{Q}_{R8}(\boldsymbol{\Upsilon}_F, t_j)\Delta t \end{bmatrix} \right) \\
\text{subject to:} & \\
d^{ij}(\theta) &\leq d_{\max} \; \forall \; i \neq j, \; (i,j) \in \{1,2,3,4\}, \; \theta \in \Theta_D \\
d^{ij}(\theta) &> d_{\min} \; \forall \; i \neq j, \; (i,j) \in \{1,2,3,4\} \\
Q_{R8}(\theta) &\geq \tau \; \forall \; \theta \in \Theta_D \\
\Theta_{\text{sci}} &\subset \Theta_D
\end{aligned} \tag{3.52}
$$

3.5 Computational Methods for Mixed Cost Optimization

This work studies the space of near-optimal solutions to complex problems involving fuel and scientific costs for a tetrahedron formation about an eccentric reference orbit. Because the functional form of J_{MMS} is highly nonlinear in the optimization variables, a globally optimal solution is difficult to determine. The total cost function requires calculation of both the fuel cost for the desired relative orbit transit as well as the science cost associated with initial and final parameterizations. The former can be a computationally intensive problem under some conditions: on a Pentium 2, 1.0 GHz machine, the solution for one point can take up to five minutes if the problem is not properly initialized; with initialization, that computation time drops to $\lesssim 5$ seconds. In all cases, however, single-point calculation of $J_{\text{sci}}(\boldsymbol{\Upsilon})$ is achieved in less than 1/10 sec on the same machine.

In order to minimize the computation time required to find near-optimal solutions for the optimization problem posed in Equation 3.51, two techniques are presented in this section. The first reduction is a Monte Carlo search applied only to the science cost. This yields highly desirable data-taking formations as well as principal directions along

which a search for other scientifically preferable formations can best be performed. The second computational reduction is a bisecting multi-path search; this search can be applied to a grid of two varying parametric directions such that only a small number of formation cost computations is actually performed in determining the minimum on the grid. In tandem, these methods can significantly shrink the search space and reduce computational demands while converging on a near-optimal solution.

3.5.1 Principal Direction Determination

By far, the most computationally intensive part of the formation cost calculation is the determination of the fuel cost to transit between formations. The easiest way to reduce computational load, then, is to remove from consideration those transits which connect formations which result in poor scientific capabilities. This subsection describes a method for characterizing scientifically useful parameterizations using a Monte Carlo simulation, with the goal of determining good, locally linear search directions along which fuel costs may be calculated near a known formation parameterization with a high science cost.

Locally linear search directions can be obtained using known information about the relationship between optimization parameters and final cost. Consider a set of M scientific costs $\mathcal{J}_{\text{sci}} = [J^1_{\text{sci}}, \ldots, J^M_{\text{sci}}] = [J_{\text{sci}}(\boldsymbol{\Upsilon}^1), \ldots, J_{\text{sci}}(\boldsymbol{\Upsilon}^M]$; the associated sets $\boldsymbol{\Upsilon}^i,\ i = 1, \ldots, M$ can then be considered as row vectors containing the parametric values which define the formations associated with these costs and stacked to form

$$\boldsymbol{\mathcal{Y}}_{1:M} = [\boldsymbol{\Upsilon}^1, \ldots, \boldsymbol{\Upsilon}^M] \tag{3.53}$$

Without loss of generality, the problem is posed such that Spacecraft 1 lies on the reference orbit and $\mathbf{x}^1(\theta) = [0,\ 0,\ 0]^T\ \forall\ \theta$. Along with the four additional constraints

realized by fixing the relative positions of the formation elements at true anomaly $\theta = \theta_C$ and the requirement that each spacecraft reside in a stable relative orbit, a total of 13 of 24 formation parameters are constrained. The remaining free parameters include the formation true anomaly θ_C and formation rotation quaternion $\mathbf{q}$ at this critical true anomaly, along with the values of p_1^i and p_5^i for $i = 1, 2, 3$. The final set of 11 elements describes a formation of four spacecraft in stable relative orbits, forming a perfect tetrahedron at true anomaly $\theta = \theta_C$.

The locally linear assumption implies that there exists some vector $\boldsymbol{\beta}$ which maps each parameterization to each cost, or

$$\mathcal{Y}_{1:M}\,\boldsymbol{\beta} = \mathcal{J} + \boldsymbol{\xi} \tag{3.54}$$

where the vector $\boldsymbol{\xi}$ gives the deviation from linearity for a particular set of parameters.

The objective here is to use *local* linearity to improve optimization over cost with low computational effort; to that end, the approximation is sufficient if, for points with similar science costs, the nonlinear component of this equation is small relative to the linear portion — i.e., for each m-element, ordered subset of the original M parameterizations, $\xi^i / J^i_{\text{sci}} \lesssim 0.1 \;\forall\; i \in [k - m + 1, \ldots, k] \subset [1, \ldots, M]$. This is difficult to examine analytically, but the assumption can be validated using a Monte Carlo simulation in which a large number of randomly-selected points is considered under a specific set of viability constraints. For this problem, local linearity is considered as a function of science cost. As such, a set of Monte Carlo solutions can be ordered according to cost, and subsets of the resultant solutions used to find locally linear approximations.

As an example, consider an ordered set of $M = 10,000$ parameterizations, grouped into subsets with $m = 250$, each with maximum science cost J^k_{sci}. The MMS formation problem regarded here is a tetrahedron in which Spacecraft 1 lies on the reference orbit

($\mathbf{x}_c = \mathbf{x}^1 = [0,\ 0,\ 0]^T$) and all four spacecraft are in stable relative orbits ($p_4^i = 0,\ i \in \{1,2,3,4\}$); formation leg length is $L_{\text{tet}} = 750$ km; minimum separation distance is $d_{\min} = 500$ km; and maximum separation distance is $d_{\max} = 2L_{\text{tet}} = 1500$ km. The central data-taking true anomaly is at apogee ($\theta_D = \pi$), with a required science window of $\delta_{sci} = 0.917$ rad. Quaternions are chosen randomly through a uniform distribution of unit length four-vectors, and the other free parameters are selected from bounded sets: $\theta_C \in \theta_D \pm 20\delta_{sci}$, $p_1^i \in [-4L_{\text{tet}},\ 4L_{\text{tet}}]$, $p_5^i \in [-2L_{\text{tet}},\ 2L_{\text{tet}}]$, $i = \{2,3,4\}$. The percentagewise mean nonlinearity the standard deviation of this nonlinearity for the $m = 250$ points up to the point with maximum science value J_{sci}^k are shown in Figure 3.4 according to the maximum science value in the subset, J_{sci}^k. For increasing J_{sci}^k the deviation from linearity increases, but even for the set composed of the $m = 250$ highest-cost sampled points ($J_{\text{sci}}^k \sim 0.48$), the greatest nonlinearity is $\lesssim 10\%$ of the true science cost. Therefore, the locally linear approximation is assumed to be reasonable to describe the science cost as a function of parameterization, even for large science costs.

Considering only the locally linear portion of Equation 3.54, a singular value decomposition (SVD) of the parameterization matrix $\mathcal{Y}$ provides useful information for optimization search directions. Let each row of $\mathcal{Y}$ contain $M \times K$ elements, with each row corresponding to a set of parameter. The matrix representation of $\mathcal{Y}$ can be partitioned generally as:

$$\mathcal{Y} = U\Sigma V^T \tag{3.55}$$

where $U \in \mathbb{R}^{M\times M}$ is an orthonormal matrix, $\Sigma \in \mathbb{R}^{M\times K}$ holds the singular values along its leading diagonal, and $V \in \mathbb{R}^{K\times K}$ is an orthonormal matrix which contains the principal directions in the parametric space along which the linear relation holds. The size of these matrix is governed by the number of free parameters K used in the parameterization.

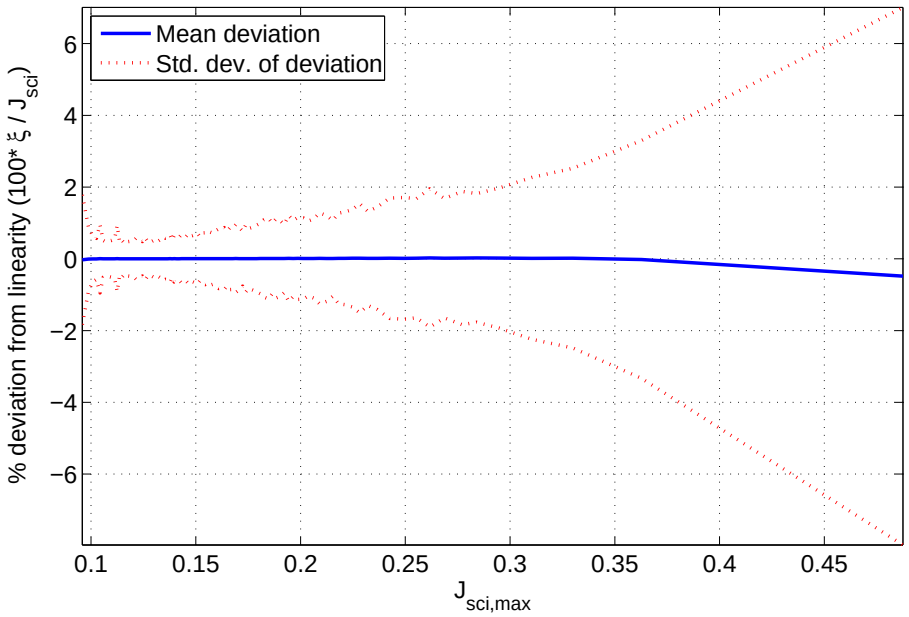

Figure 3.4: Monte Carlo analysis of $M = 10,000$ scientifically viable formations demonstrating the reasonableness of the linearity assumption. Percentagewise deviation from linearity of science cost is found by ordering the points by science cost, then evaluating mean and standard deviation of the nonlinear component for the $m = 250$ elements which satisfy $J^i_{\text{sci}} \leq J^k_{\text{sci}}, i \in [k-m, \ldots, k]$. At each $i \in [k-m, \ldots, k]$, the nonlinear residual vector is ξ^i / J^i_{sci}. Local linearity increases with increasing maximum set cost, but the standard deviation of this ratio remains within 10% of the true science cost even for those formations with largest J_{sci}.

The singular values are placed in descending along the leading diagonal of Σ, and the singular vectors are similarly ordered in V. The non-zero elements of Σ roughly indicate the weight of the associated parametric axis in the matrix V in determining both the value of J_{sci} and the viability of an orbit. Again, it is important to note that this decomposition provides useful information only in a locally linear sense, such that the rows of $\mathcal{Y}$ should correspond to those parameterizations which provide similar science costs.

The columns of the V, v_j for $j = [1, \ldots, K]$, indicate the key directions along which further viable solutions are likely to be found. Traversing parametric directions which are most represented in the high-science cost formations typically leads to improved optimization of the science cost while minimizing the likelihood of violating viability constraints. As an example, consider attempting to improve science cost using the Monte Carlo analysis performed previously. For that problem, there are $K = 16$ free parameters. In Figure 3.5, a central point with parameterization $\boldsymbol{\Upsilon}$ given by the parameterization corresponding to the maximum science cost — by definition in the ordered set J_{sci}^{M} — from the Monte Carlo search; call this parameterization $\boldsymbol{\Upsilon}^{M}$. The plot shows two attempts to improve on this science cost by searching along parametric directions. In each case, J_{sci} is found as a function of the linear variation of $\boldsymbol{\Upsilon}^{M}$ according to:

$$\boldsymbol{\Upsilon} = \boldsymbol{\Upsilon}^{M} + \psi_m \mathbf{v}_m + \psi_n \mathbf{v}_n \tag{3.56}$$

The multipliers ψ_m and ψ_n are scalings of the nth and mth columns of the matrix V. To show how these scalings can be used to the benefit of the overall science cost, consider the example of $L_{\text{tet}} = 500$ km, with $d_{\min} = 100$ km, $d_{\max} = 3L_{\text{tet}} = 1000$ km. As above, the central data-taking true anomaly is at apogee ($\theta_D = \pi$), with a required science window of $\delta_{sci} = 0.917$ rad. Quaternions are chosen randomly through a uniform distribution of unit length four-vectors, and the other free parameters are selected from

bounded sets: $\theta_C \in \theta_D \pm 20\delta_{sci}$, $p_1^i \in [-4L_{\text{tet}},\ 4L_{\text{tet}}]$, $p_5^i \in [-2L_{\text{tet}},\ 2L_{\text{tet}}]$, $i = \{2, 3, 4\}$. The $M = 10,000$ Monte Carlo parameterizations are ordered according to cost J_{sci}, and the matrix V is formed of the $m = 250$ parameterizations with highest data-taking capability. The central parameterization Υ^M is chosen to be the parameterization associated with the maximum science cost, $J_{\text{sci}}^{10000} = 0.578$, and $J(\Upsilon)$ is found for Υ varied along two sets of principal axes. Figure 3.5 shows the results of this operation for $m = 1$ and $n = 2$ (left), and $m = 5$ and $n = 6$ (right). It is clear that optimizing the principal directions associated with the largest singular values yields a much broader search space as well as greater improvements in science cost. The approach used in this paper explores variations in parameterization Υ^M which improve science cost J_{sci}^M for $m = 1$ and $n = 2$ only. This will allow more useful comparison of optimal parameterizations achieved for different vales of the mixed-metric weighting vector $\boldsymbol{\alpha}$.

3.5.2 Bisecting Multipath Search

The previous subsection addressed a method for determining locally linear search directions, based solely on science cost, in which improved science costs correlated with scientifically viable orbits could be found. However, the general form of the cost function J_{MMS} in Equation 3.48 includes both fuel and science contributions. Unfortunately, solving for fuel-optimal transits between parameterizations Υ_0 and Υ_F is not computationally trivial; determination of fuel cost J_{fuel} requires solving the minimum fuel maneuver for each spacecraft in the formation, each of which takes up to 3 minutes on a 1 GHz machine operating in Windows XP. Therefore, it is proposed here to use the two best *science-based* linear search directions found previously as a two-dimensional search space along which to scan for a locally optimal mission cost which incorporates both science and fuel. This subsection examines a bisecting multipath search technique

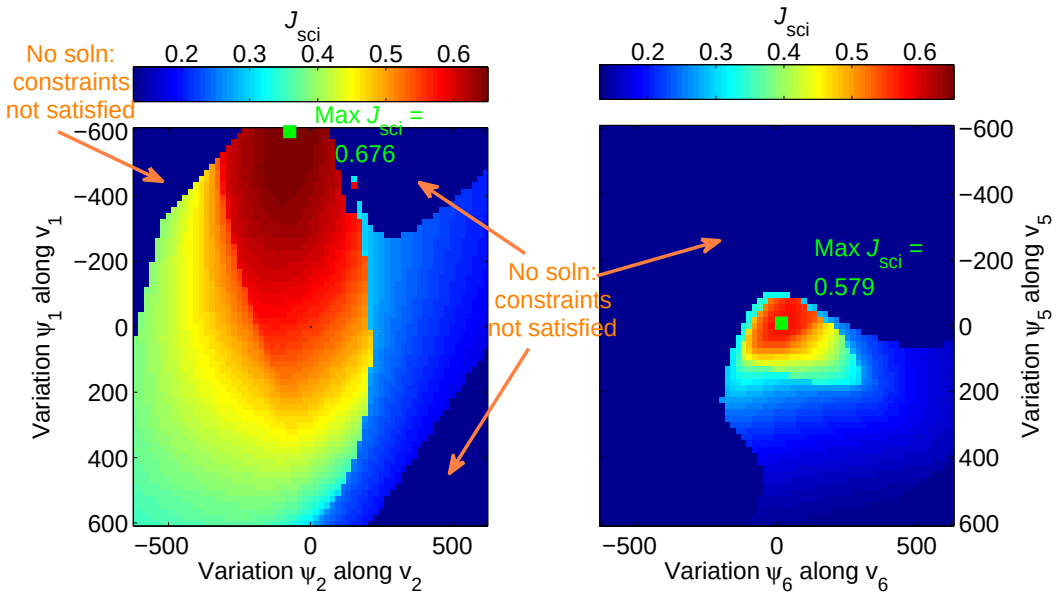

Figure 3.5: Comparative effect of singular value weight on the final determined science cost for a tetrahedron near apogee with leg length $L_{\text{tet}} = 500$ km with $d_{min} = 100$ km, $d_{max} = 1500$ km. Left: Parameterization varied along the two largest singular vectors, with maximum $J_{\text{sci}} = 0.676$ (green square), a 17 percent improvement over the nominal $(0, 0)$ cost of $J^M_{\text{sci}} = 0.578$. Right: The directions associated with the 5th and 6th singular values are varied, with significantly less flexibility before constraints are violated and little improvement (max $J_{\text{sci}} = 0.579$) over the nominal cost. The regions of darkest blue have no data due to constraint violations.

which allows swift traversal of such a two-dimensional parametric search space by sampling the space with $\left(2^N + 1\right) \times \left(2^N + 1\right) = S \times S$ grid points and finding the minimum on that grid. While this search does not necessarily find the grid space global minimum, the solution will always be near a local minimum and thus an optimistic — if not optimal — orbit option.

The bisecting multipath search is a stepwise narrowing of a full search space intended to converge on the region most likely to contain the grid's global minimum. A flowchart showing how the bisecting multipath search operates is shown in Figure 3.6. To simplify notation for this section, the subscript $()_{\text{MMS}}$ has been dropped from J_{MMS} in Equation 3.48. Let each point be referenced by its coordinates (m, n) on the search grid; the cost at point (m, n) is then given by $J(m, n)$. The bisecting multipath search is initialized by solving the cost function at the corners of each of the quadrants. The initial value of the maximum cost gradient in each direction can be chosen as the maximum gradient found using the solutions to these initial points.

At the kth step in the bisecting multipath procedure, the set $\mathbf{N}[k]$ holds the (m, n) pairs associated with the *solved* grid points; similarly, the set of *unsolved* grid pairs is contained in the set $\bar{\mathbf{N}}[k]$. As well, at the start of the kth step, a set of *active* grid points $\mathbf{N}_A[k] \in \bar{\mathbf{N}}[k]$ holds the (m, n) coordinates of the grid points which may be or may reside adjacent to the global minimum on the grid. In addition to these sets, the algorithm must retain the minimum cost found as of the kth search step, $J_{\min}[k]$ along with the maximum gradient along each direction, $\mathrm{d}J/\mathrm{d}n$ and $\mathrm{d}J/\mathrm{d}m$. These last two values are updated continuously throughout the search and are therefore independent of the search step k.

The search proceeds along directions of maximum likelihood in which a new minimum might be found, based on the current gradients, by operating on the set of active

points, $\mathbf{N}_A[k]$. For each point in this active set, three possibilities exist: (1) the point is a local minimum; (2) the point may reside adjacent to a local minimum; or (3) the point cannot reside adjacent to a local minimum given the current maximum gradient. If a point is determined to be a local minimum, it remains in the active set $\mathbf{N}_A[k+1]$. Those points which may lie adjacent to a local minimum are also retained in $\mathbf{N}_A[k+1]$, and a neighboring point is added to determine whether such an adjacent local minimum exists. Points which cannot lie adjacent to a local minimum are removed from the active set. The objective is to search the space until the set $\mathbf{N}_A[k+1] \subset \mathbf{N}_A[k]$, such that no additional points will be solved in the next step, suggesting that the only remaining points are on or adjacent to a local minima; if the grid space is sufficiently fine, the minimum of these local minima will be the vertex-constrained global minimum on the grid.

Let the ith point in the set $\mathbf{N}_A[k]$ be denoted (m_i, n_i), with its cost $J(m_i, n_i)$. The set of neighboring points to this ith point is given by $\mathbf{N}_{i,\text{nbr}}[k]$, and it initially consists of the solved, viable points neighboring (m_i, n_i) whose cost is less than $J(m_i, n_i)$. Mathematically, these points are such that, for $(m_j, n_j) \in \mathbf{N}_{i,\text{nbr}}[k]$, $(m_j, n_j) \in \mathbf{N}[k]$ and $J(m_j, n_j) < J(m_i, n_i)$, and either $m_j = m_i$ *or* $n_j = n_i$; as well, for all $(m, n) \in \mathbf{N}[k]$, no point resides between (m_i, n_i) and (m_j, n_j). This is described by:

$$(m_j, n_j) = \begin{cases} \left\{ \underset{(m_j,n_j)\in\mathbf{N}[k]}{\text{argmin}} \; |n_i - n_j| \;\text{ s.t. }\; \frac{n_i - n_j}{n_i - n} > 1 \right\} & \text{if } \; m = m_i = m_j \\ \left\{ \underset{(m_j,n_j)\in\mathbf{N}[k]}{\text{argmin}} \; |m_i - m_j| \;\text{ s.t. }\; \frac{m_i - m_j}{m_i - m} > 1 \right\} & \text{if } \; n = n_i = n_j \end{cases} \tag{3.57}$$

The points in $\mathbf{N}_{i,\text{nbr},0}[k]$ additionally must be such that the cost $J(m_j, n_j)$ satisfies all problem constraints and the point is viable. The definition is then:

$$\mathbf{N}_{i,\mathrm{nbr},0}[k] = \Big\{(m_j, n_j) \in \mathbf{N}[k] \;\; \text{s.t.} \;\; J(m_j, n_j) \;\; \text{viable}\Big\} \tag{3.58}$$

This neighboring set $\mathbf{N}_{i,\mathrm{nbr}}[k]$ initially contains up to four points. If this set $\mathbf{N}_{i,\mathrm{nbr},0}[k] = \emptyset$, the point is a local minimum in $\mathbf{N}[k]$, and (m_i, n_i) is retained in $\mathbf{N}_A[k+1]$, but no further evaluation is necessary on the neighboring points.

If $\mathbf{N}_{i,\mathrm{nbr},0}[k] \neq \emptyset$, each cost $J(m_j, n_j)$ is compared against the cost $J(m_i, n_i)$ to update the directional gradients according to

$$\begin{aligned} \frac{\mathrm{d}J}{\mathrm{d}n} &= \max\left\{\left\{\frac{J(m_i, n_i) - J(m_j, n_j)}{\left|n_i - n_j\right|} \;\; \text{if} \;\; n_i \neq n_j\right\}, \frac{\mathrm{d}J}{\mathrm{d}m}\right\} \\ \frac{\mathrm{d}J}{\mathrm{d}m} &= \max\left\{\left\{\frac{J(m_i, n_i) - J(m_j, n_j)}{\left|m_i - m_j\right|} \;\; \text{if} \;\; m_i \neq m_j\right\}, \frac{\mathrm{d}J}{\mathrm{d}m}\right\} \end{aligned} \tag{3.59}$$

It is now desired that a secondary set of neighboring points be constructed which will contain the possible optimal search directions. This secondary set, $\mathbf{N}_{i,\mathrm{nbr}}[k] \subset \mathbf{N}_{i,\mathrm{nbr},0}[k]$, is obtained by retaining only those points for which the cost can decrease from $J(m_i, n_i)$ to $J_{\min}[k]$ at the maximum gradient $\mathrm{d}J/\mathrm{d}n$ or $\mathrm{d}J/\mathrm{d}m$, then increase at that gradient or less to the neighboring cost $J(m_j, n_j)$. If the neighboring point has $m_j = m_i$, the point (m_j, n_j) is retained in $\mathbf{N}_{i,\mathrm{nbr}}[k]$ if

$$J(m_j, n_j) - J_{\min} < \frac{dJ}{dn}\left|n_j - n_i\right| - (J(m_i, n_i) - J_{\min}[k]) \tag{3.60}$$

Alternatively, if the neighboring point has $n_j = n_i$, the constraining inequality becomes:

$$J(m_j, n_j) - J_{\min} < \frac{dJ}{dm}\left|m_j - m_i\right| - (J(m_i, n_i) - J_{\min}[k]) \tag{3.61}$$

Points which do not satisfy these inequalities are not placed in $\mathbf{N}_{i,\mathrm{nbr}}[k]$. If $\mathbf{N}_{i,\mathrm{nbr}} = \emptyset$, no direction satisfies the inequalities in Equation 3.60 or 3.61 and the point (m_i, n_i) is not

a local minimum and does not reside adjacent to a global minimum, so it is not carried forward in the active set.

If, however, $\mathbf{N}_{i,\text{nbr}}[k] \neq \emptyset$, the neighboring point in the two optimal search directions, $(m_{j,\text{opt}}, n_{j,\text{opt}})$, is found by:

$$(m_{j,\text{opt}}, n_{j,\text{opt}}) = \underset{(m_j,n_j)\in\mathbf{N}_{i,\text{nbr}}[k]}{\text{argmax}} \frac{J(m_j, n_j) - J(m_i, n_i)}{|(m_j + n_j) - m_i - n_i|} \tag{3.62}$$

This defines the optimal search direction along which the bisecting multipath search proceeds from the point (m_i, n_i), and a point between (m_i, n_i) and (m_j, n_j), given by $(m_{\text{mp}}, n_{\text{mp}})$, is added to the active set for the next search step. This point is defined as the unsolved point $(m, n) \in \bar{\mathbf{N}}[k]$ nearest the midpoint between these solved points:

$$\begin{aligned}(m_{\text{mp}}, n_{\text{mp}}) \quad = \quad & \underset{(m,n)\in\bar{\mathbf{N}}[k]}{\text{argmin}} \left|m - \frac{m_{j,\text{opt}} + m_i}{2}\right| + \left|n - \frac{n_{j,\text{opt}} + n_i}{2}\right| \\ & \text{s.t.} \quad \frac{m_i - m_{j,\text{opt}}}{m_i - m} > 1 \quad \text{and} \quad \frac{n_i - n_{j,\text{opt}}}{n_i - n} > 1 \end{aligned} \tag{3.63}$$

Note that, if no gridpoint in $\bar{\mathbf{N}}[k]$ resides between (m_i, n_i) and (m_j, n_j), the constraining inequalities will not be satisfied by any point in $\bar{\mathbf{N}}[k]$. If $(m_{\text{mp}}, n_{\text{mp}})$ exists, it is added to the active set for the next search step, $\mathbf{N}_A[k+1]$, along with the generating point (m_i, n_i).

Special considerations must be made if a point (m_i, n_i) is found to be not scientifically viable. In this case, the set $\mathbf{N}_{i,\text{mp}}[k]$ is formed by taking the midpoints to all solved neighboring points. These are defined as the points which, for $(m_j, n_j) \in \mathbf{N}[k]$, $m_j = m_i$ or $n_j = n_i$ and no point in $\mathbf{N}[k]$ resides between (m_j, n_j) and (m_i, n_i). The set of midpoints is then defined as the set of $(m, n) \in \bar{\mathbf{N}}[k]$ which, for points (m_j, n_j) which satisfy Equation 3.57, satisfy the following:

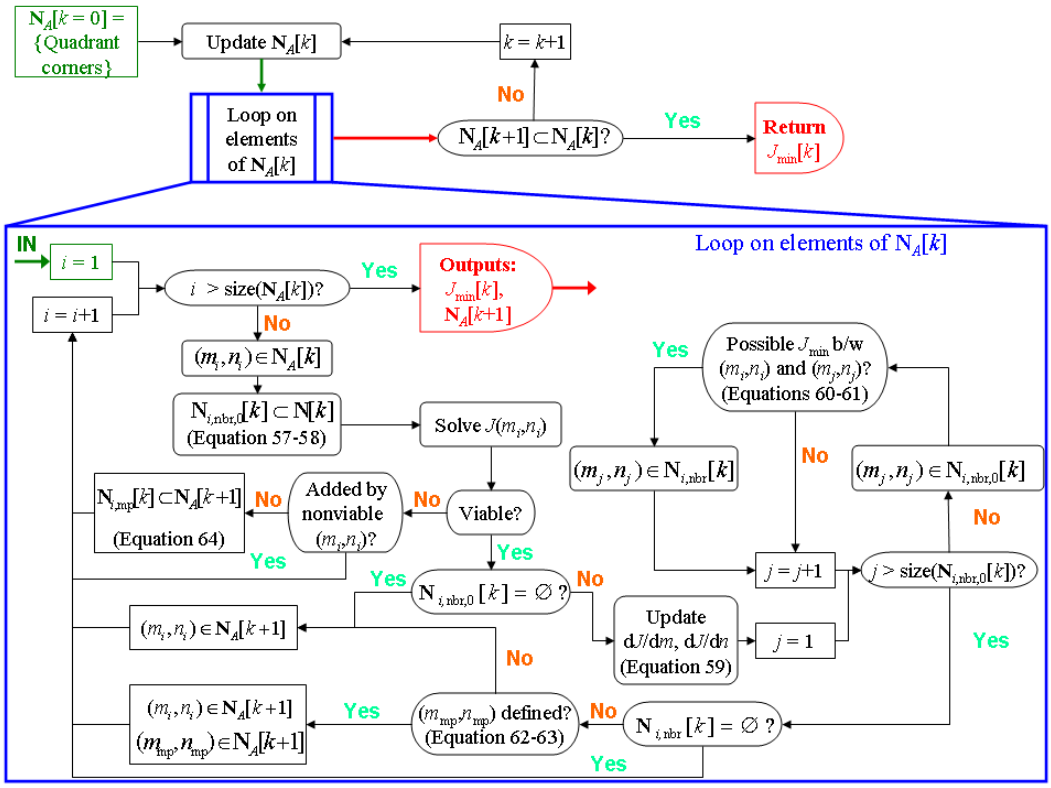

Figure 3.6: Flowchart showing the bisecting multipath search algorithm described in the text.

$$\mathbf{N}_{i,\mathrm{mp}}[k] = \left\{ \underset{(m,n)\in\bar{\mathbf{N}}[k]}{\operatorname{argmin}} \left| m - \frac{m_j + m_i}{2} \right| + \left| n - \frac{n_j + n_i}{2} \right|, \ (m_j, n_j) \in \mathbf{N}[k] \right\} \tag{3.64}$$

Note that up to four points can satisfy this inequality. Because the point (m_i, n_i) is not viable, if it was not activated by a nonviable point, all elements of the set $\mathbf{N}_{i,\mathrm{mp}}[k]$ are placed in the active search space for the next step, $\mathbf{N}_A[k+1]$. If the point was activated by a nonviable point, the point is not carried forward in $\mathbf{N}_A[k+1]$ and does not activate any more points. This allows a cursory probing of the nonviable region without greatly increasing the size of the active search space.

By disregarding those regions which do not maintain a low, near-minimum cost over

multiple search steps, the number of evaluations of J_{fuel} necessary to solve Equation 3.51 is significantly reduced, increasing the tractability of the optimization problem.

In order to demonstrate the bisecting multipath search operation, consider the case of a cost function given by

$$J(m,n) = 3(1-n)^2 e^{-n^2-(m+1)^2} - 10\left(\frac{n}{5} - n^3 - m^5\right)e^{-n^2-m^2} - \frac{1}{3}e^{-(n+1)^2-m^2} \tag{3.65}$$

and evaluated over the range $n \in [-3,3],\ m \in [-3,3]$. This cost function is an effective illustration because it has multiple local minima and maxima in this region. For this example, let $N = 4$, such that a 17×17 grid is employed to derive the solution; additionally, some regions are designated nonviable to show how the algorithm handles nonviable points. Figure 3.7 shows a visualization of the bisecting multipath search for four values of the iteration step k, with nonviable regions shown in white and all other points shaded according to cost $J(m,n)$. The minimum found at the final step, $k = 7$, is $J_{\min}[k] = -6.19$, which corresponds to the global grid minimum. The process evaluates just 43 of the 289 points on the grid — less than 15% — in one iteration. Two additional iterations using $N = 4$ and operating on a region 1/4 the size of the previous iteration retrieves a grid minimum of $J(m,n) = -6.55$, within 0.02% of the true global minimum; combined, the three iterations require just 111 computations.

The number of points, s, solved by the bisecting multipath search compared to the original order of the grid size, N, is generally difficult to determine and depends on the structure of the underlying cost function. However, for a continuous cost function with a continuous, smooth first derivative, s can be bounded by considering the best and worst cases. In the best case, the solution lies at an intermediate or edge point near the largest derivative in both directions; this problem is solved by a bisection along each direction, which requires $O(N)$ pointwise evaluations along each dimension, with S the grid length

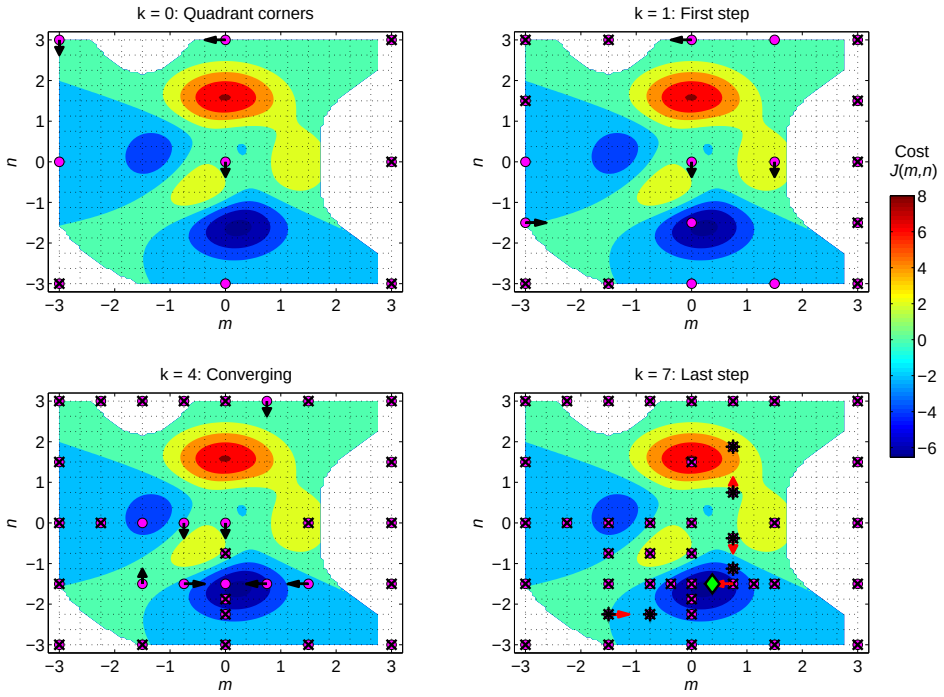

Figure 3.7: Illustration of the bisecting multi-path search algorithm applied to a sample cost function with nonviable regions. The optimization is initialized at $k = 0$ in the quadrant corners. Successive steps evaluate the cost $J(m, n)$ along maximally decreasing-cost directions from the points in the active set $\mathbf{N}_A[k]$, represented with black arrows for $k = 0, k = 1, k = 4$. Points which are crossed out have been evaluated but are either not viable or cannot lie adjacent to a global minimum. The procedure requires $k = 7$ steps. In the $k = 7$ panel, discarded points are shown with a star, while the red arrows give the search directions from $k = 6 \rightarrow k = 7$. The vertex-constrained global minimum (in this case, solved) is the green diamond in that panel.

along one side. Thus, the total solution requires $N^2 \lesssim s$ evaluations to find the solution, including initialization. The worst case has an interior solution near the region of the smallest derivative. Here, the number of points evaluated at each step is approximately constant and the size of $\mathbf{N}_A[k]$ does not decrease for increasing k, yielding $\frac{1}{2}S$ points in each direction, or $\frac{1}{4}S^2 \sim O(2^{2N})$ points required to find the optimal solution. The number of evaluations for any problem is then bounded by

$$N^2 \lesssim s \lesssim 2^{2N} \tag{3.66}$$

These bounds hold only for $N > 3$, as at least 9 points are guaranteed solved in the first step — the corners, edge midpoints, and center point of the search space. Note that if the underlying cost function is not smooth, discontinuities may inflate the estimate of the maximum gradient.

Additional refinement of the computed solution can be achieved near a solved minimum by producing a finer grid about this minimum and applying the same search method to that finer grid. This approach yields an iterative solution which improves on each new grid. In this case, a moderately coarse grid with a $N = 4$ or $N = 5$ is sufficient to identify the region near the minimum; finer grids operate over a much smaller span to allow for rapid convergence to a local minimum. Note that each grid refinement typically results in a greater number of total solutions on the grid space as the local gradient decreases, but for $N > 3$, the total number of solved points on multiple, coarse grids is always less than a single fine grid at the same resolution. Thus, moving from $N = 3$ to $N = 5$ is far more computationally intensive than refining the $N = 3$ grid at 4 times the resolution with a second $N = 3$ grid.

3.6 Magnetospheric Multiscale Mission Examples

The Magnetospheric Multiscale (MMS) mission demands a variety of formations using a reference orbit with constant semi-major axis a and eccentricity e. In particular, Phase II of the MMS mission is tasked with observing the reconnection of the magnetosphere behind the Earth at and near an apogee distance of 25 Re, with a 1.2 Re perigee crossing for data downlink. The Cluster mission[48] previously determined that the critical reconnection occurs at less than 10 km separation; however, the science of the MMS mission requires determination of the optimal tetrahedron separation distance at a single critical true anomaly in order to explore the reconnection phenomenon. For this phase specifically, the MMS mission includes a formation in which the baseline tetrahedron separation distance L_{tet} between adjacent members shrinks from 1000 km to 1 km in single-maneuver steps of 20-30% reduction, with several steps per month, and data-taking occurs at each separation. When this formation baseline leg length L_{tet} reaches a minimum of 1 km, the optimal leg length for exploring reconnection will be determined by ground controllers, and the formation will return to this leg length for the remainder of Phase II.

This section examines the proposed MMS mission in two ways, using the analytical techniques derived in the preceding sections. The first is an exploration of the variations in costs and parameterizations associated with single-step maneuvers of the tetrahedron formation. These steps are taken between two formation sets, and some general information about optimal transits involving both centered and near-optimal formations is inferred. The second examination is of the proposed MMS string of maneuvers; this series will show the global implications of multi-step formation changes, which include effects on a mission's fuel and data-taking profile, as well as the trade-offs that are made as the mission advances. All examples use the mixed-metric cost formulation given in

Equation 3.52, disregarding the initial science cost at the originating formation parameterization. However, this parameterization can be included in the final mission design if the simplified form solved here does not adequately address mission needs.

Before proceeding to these examples, however, several of the demands of the current MMS design are considered. The proposed mission plan attempts to make the region about apogee viable — $Q_{R8}(\theta) \geq 0.7$ for $\|\mathbf{R}\| > 16$ Re. This objective is not likely to be achieved by a passive formation for a variety of reasons. First, based on prior work involving MMS-like formations[16, 40], a tetrahedron can hold its shape near apogee for less than 30 percent of the total orbit time for a symmetric formation; increasing the percentage of total orbit time for which the formation is near-tetrahedral results in a lopsided geometric quality factor $Q_{R8}(\theta)$, similar to the lopsidedness of the Robert-Roux quality factor $Q_{\mathrm{RR}}(\theta)$ examined in that work. Second, while several papers have shown a multitude of formations with extended segments of the orbit in which a tetrahedron is largely maintained, [37, 40] none of these has approached the 16 Re demands of MMS for either of these quality factors, even when searching families of orbits with high scientific value. Finally, the geometric quality factor Q_{R8} tends to have a value that is less than the Robert-Roux quality factor Q_{RR} at any given true anomaly θ, suggesting that its use here will provide slightly degraded performance from even those results. While the goals of the MMS designers may be attainable using active control throughout the orbit to maintain the desired formation structure[37], that approach requires significant amounts of fuel and is unreasonable for the multi-step data-taking as proposed for MMS. This chapter instead attempts to rely solely on passive formations by compromising between the *goals* of the MMS mission and *stated desires* of the mission proposal. Along with the need for less overall fuel to complete the mission, these passive formations do not require intervention to be a viable data-taking platform, simplifying the overall mis-

sion design. For these reasons, in the following examples, the geometric quality factor $Q_{R8}(\theta)$ is utilized with a cutoff value $\tau = 0.6$ — lower than the stated desire of $\tau = 0.7$, but corresponding more nearly with $\tau = 0.7$ for the Robert-Roux quality factor; as well, formations for which $Q_{R8}(\theta)$ satisfies the mission objectives for a more reasonable 25% of the orbit time about apogee are considered viable.

For the examples given in this section, each spacecraft is assumed to be capable of on-off thrust along two orthogonal directions with a maximum thrust of 8×10^{-4} N/kg; this thrust is further assumed to be applied continuously with instantaneous activation and deactivation. The problem is considered for a geometric quality factor with cutoff $\tau = 0.6$. The minimum allowed interspacecraft distance for collision avoidance is $d_{\text{min}} = 500$ m, and the maximum interspacecraft distance considered for viable data scales with the formation leg length as $d_{\text{max}} = 2L_{\text{tet}}$, with the desired data-taking true anomaly at apogee ($\theta_D = \pi$) and a science window such that, about this point, 25% of the orbit time is viable ($\delta\theta_{\text{sci}} \approx 0.917$). The solution to the formation optimal maneuver cost problem given by Equation 3.52 is then found for variable $\alpha_{\text{fuel}} > 0$ and constant $\alpha_{\text{sci}} = -1/P$, where P is the orbital period, then again for $\boldsymbol{\alpha} = [0,\ 1]$ to obtain the optimal fuel-only cost. The fuel-only ($\alpha_{\text{sci}} = 0$) and science-only ($\alpha_{\text{fuel}} = 0$) costs represent limiting cases for the mixed-metric cost function. This allows an examination of all regions of the mixed-metric cost function. The science-optimal formation requires more fuel to transit to than any mixed-metric optimal formation, and the fuel-optimal transition results in a lower data-taking capability for the final formation than any mixed-metric optimal formation. It is relevant, then, to consider how the independent costs J_{fuel} and J_{sci} behave within the mixed-metric cost function J_{MMS} between these limiting cases, and consider the consequences for the resultant optimal mixed-metric parameterizations $\boldsymbol{\Upsilon}^*$. General rules can then be explored for optimal transits which can be applied to

similar problems.

3.6.1 Single-Step Formation Optimal Maneuvers

In order to better understand the features of the mixed-metric formation optimal cost problem, it is useful to look first at the problem of transiting between a fixed tetrahedron formation and a near-optimal formation. This problem is related to the formation initialization problem, where the MMS formation begins in a known state and maneuvers to a near-optimal formation. In this case, two scenarios are probed for the fixed tetrahedron. In the first scenario, the tetrahedron is transited from an *uninitialized* parameterization to a *near-optimal* parameterization of the same leg length L_{tet}, while the second explores a transit from a *Monte Carlo optimal* (MC optimal) parameterization to a *near-optimal* parameterization of a shorter leg length.

In the *uninitialized* state, the nominal formation parameterization is fully determined without regard to formation data-taking and with relaxed collision avoidance constraints. Uninitialized parameterizations are denoted Υ_{nom}. For this example, the initialized formation center resides at Spacecraft 1 only at the formation critical true anomaly $\theta = \theta_C$, with leg lengths scaled by L_{tet}; the formation parameterization set Υ has elements $p_1^i = 0$ and $p_5^i = 0.5L_{\text{tet}}$ for $i \in [1, 2, 3, 4]$, $\theta_C = \pi$, and $\underline{\mathbf{q}} = [1,\ 0,\ 0,\ 0]^T$ — i.e. the formation is unrotated and satisfies the tetrahedron element positions given in Table 3.1. A *Monte Carlo optimal* (MC optimal) formation is the parameterization Υ_{MC} which provides the greatest data-taking capabilities J_{sci} while satisfying collision avoidance and data-taking constraints presented in this chapter in Section 3.4.3.4.2-3.4.3, as found through a Monte Carlo simulation on the free parameters. The *near-optimal* parameterization is a stable formation which is a local solution to Equation 3.52. For the problems considered here, the nominal parameterization about which a locally optimal solution is found will be

Table 3.2: Pertinent elements of the example simulation given in the text: Problem constraints as well as fixed and free elements of the parameter set $\boldsymbol{\Upsilon}$.

$$\boldsymbol{\Upsilon}_{\text{fixed}} = \left\{ \mathbf{x}_c \quad \tfrac{1}{L_{\text{tet}}}\mathbf{x}_p^1 \quad p_4^1 \quad \tfrac{1}{L_{\text{tet}}}\mathbf{x}_p^2 \quad p_4^2 \quad \tfrac{1}{L_{\text{tet}}}\mathbf{x}_p^3 \quad p_4^3 \quad \tfrac{1}{L_{\text{tet}}}\mathbf{x}_p^4 \quad p_4^1 \right\}$$

$$\boldsymbol{\Upsilon}_{\text{MC,fixed}} = \left\{ \begin{pmatrix} 0 \\ 0 \\ 0 \end{pmatrix} \begin{pmatrix} 0 \\ 0 \\ 0 \end{pmatrix} \quad 0 \quad \begin{pmatrix} 0 \\ -\frac{2\sqrt{3}}{3\sqrt{2}} \\ -\frac{\sqrt{3}}{3} \end{pmatrix} \quad 0 \quad \begin{pmatrix} -\frac{1}{2} \\ -\frac{2\sqrt{3}}{3\sqrt{2}} \\ \frac{\sqrt{3}}{6} \end{pmatrix} \quad 0 \quad \begin{pmatrix} \frac{1}{2} \\ -\frac{2\sqrt{3}}{3\sqrt{2}} \\ \frac{\sqrt{3}}{6} \end{pmatrix} \quad 0 \right\}$$

$$\boldsymbol{\Upsilon}_{\text{free}} = \left\{ (q_\phi, \mathbf{q}) \quad \theta_C \quad (p_1^2, p_5^2) \quad (p_1^3, p_5^3) \quad (p_1^4, p_5^4) \right\}$$

Constraints:
$$\left\{ \begin{array}{ccc} L_{\text{tet}} \in [1000, 750, \ldots, 10] \text{ km}, & \delta_{\text{sci}} = 0.0917 \text{ rad}, & \tau = 0.6, \\ d_{\min} = 500 \text{ m}, & d_{\max} = 3L_{\text{tet}} & \end{array} \right\}$$

an MC optimal parameterization. The near-optimal parameterization must satisfy all collision avoidance and data-taking constraints, and is denoted $\boldsymbol{\Upsilon}^*$.

For the first scenario, consider the transition from an uninitialized formation parameterization to a near-optimal formation parameterization for two nominal formation leg lengths, $L_{\text{tet}} = 1000$ km and $L_{\text{tet}} = 500$ km; both the uninitialized and near-optimal tetrahedrons have this leg length at their respective critical true anomalies. The minimum costs J_{fuel} and J_{sci} obtained for all $\alpha_{\text{sci}} = -1/P$ for the two sample transits are shown in Figure 3.8. In Figure 3.8(a), the formation optimal fuel-only cost for the smaller maneuver is approximately 1/2 that of the fuel-only cost for the larger maneuver; however, the absolute difference in fuel cost between the science-only solution — in which the

fuel cost does not contribute to the formation cost J_{MMS} — and the fuel-only solution is only 10% smaller. This is particularly unusual given that the smaller formation maneuver converges more slowly on the fuel-only cost while the science cost simultaneously decreases. This decreasing science cost suggests that the fuel cost should be driving the solution more significantly, but it is evident that the fuel cost has effectively stagnated. This indicates that variations in J_{fuel} play a more significant role in the solutions for small α_{fuel} than would be expected for a formation whose total fuel cost is approximately half that of the larger formation performing a similar maneuver.

The science cost provides another valuable insight. The science cost J_{sci} for each leg length is approximately the same near $\alpha_{\text{fuel}} = 0$, but the cost for $L_{\text{tet}} = 1000$ km appears to converge suddenly on a final value for $\alpha_{\text{sci}} = -1/P$, while the science cost for the smaller tetrahedron continues to decline monotonically. However, the fuel-only case for $L_{\text{tet}} = 1000$ results in a science cost that is approximately 20% lower than the apparent converged value and 19% less than the fuel-only cost for the smaller tetrahedron. This is the result of a discontinuity in the science cost caused by the data-taking constraints, and illustrates how the choice of $\boldsymbol{\alpha}$ works with these constraints in determining mission value. In this case, the discontinuity is caused by a subtle change in the quality factor $Q_{R8}(\theta)$. Near the MC optimal formation, the quality factor has one local minimum and two local maxima over the continuous data-taking window about $\theta = \theta_D = \pi$. At the discontinuity (known computationally as a *shock*), the local minimum drops below $\tau = 0.6$, leading to the loss of a large portion of that data-taking window without violating any of the problem constraints. For the smaller formation, this decline in quality factor also leads to a constraint violation, such that the associated formations are nonviable. This behavior is rare in highly constrained problems but becomes more common as those constraints relax.

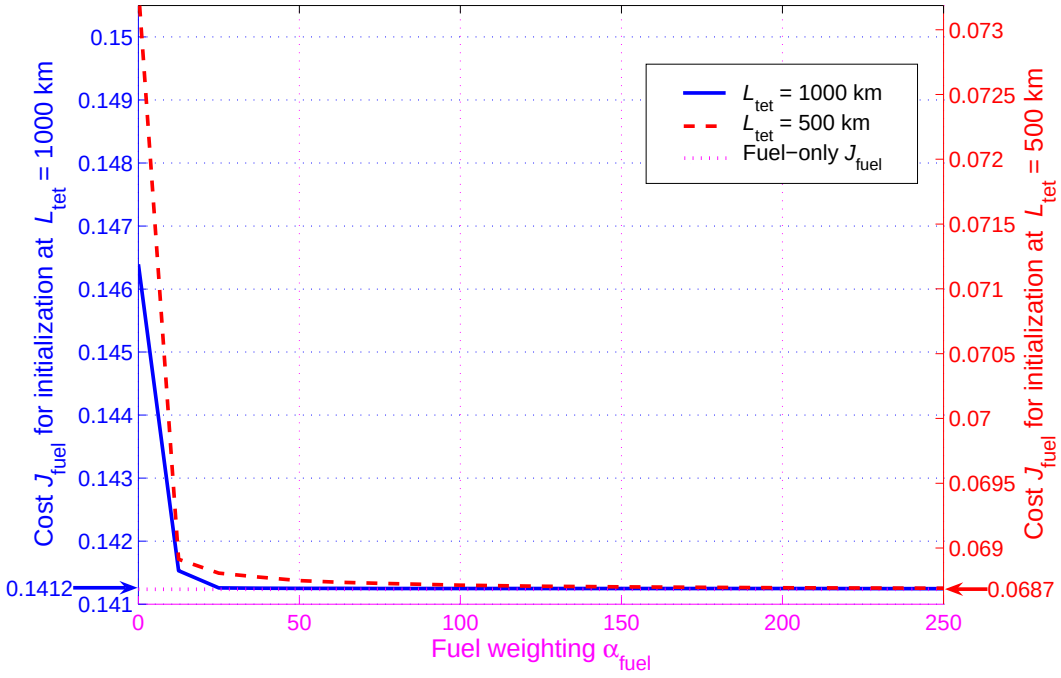

(a)

Figure 3.8: Fuel cost (a) and science cost (b) as a function of fuel cost weighting α_{fuel} for $\alpha_{\text{sci}} = -1/P$ at formation leg lengths of $L_{\text{tet}} = 1000$ km and $L_{\text{tet}} = 500$ km for a transition from an uninitialized state to a near-optimal formation parameterization. The blue solid line is associated with the left axes and the red dashed line is associated with the right axes. In (a) the dotted line indicates the best-case fuel cost at $\alpha_{\text{sci}} = 0$ for both formation leg lengths. In (b) the dotted line shows only the worst-case science cost of $J_{\text{sci}} = 0.587$ at $\alpha_{\text{sci}} = 0$ for leg length $L_{\text{tet}} = 500$ km; the corresponding cost for $L_{\text{tet}} = 1000$ km is $J_{\text{sci}} = 0.485$ and is off the plot (blue arrow).

Figure 3.8 (Continued)

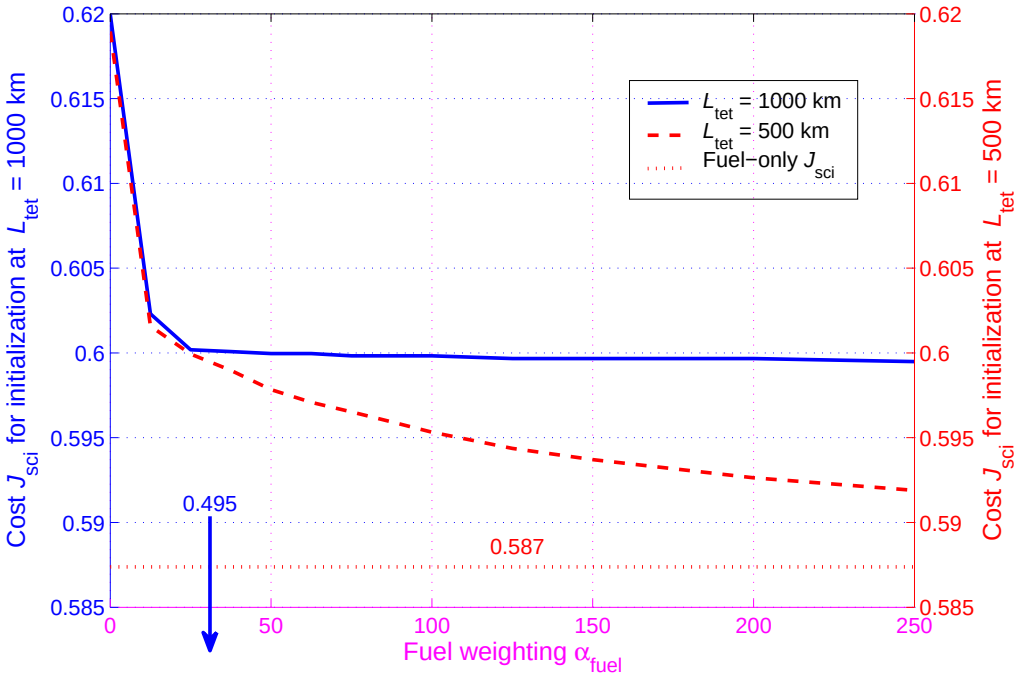

(b)

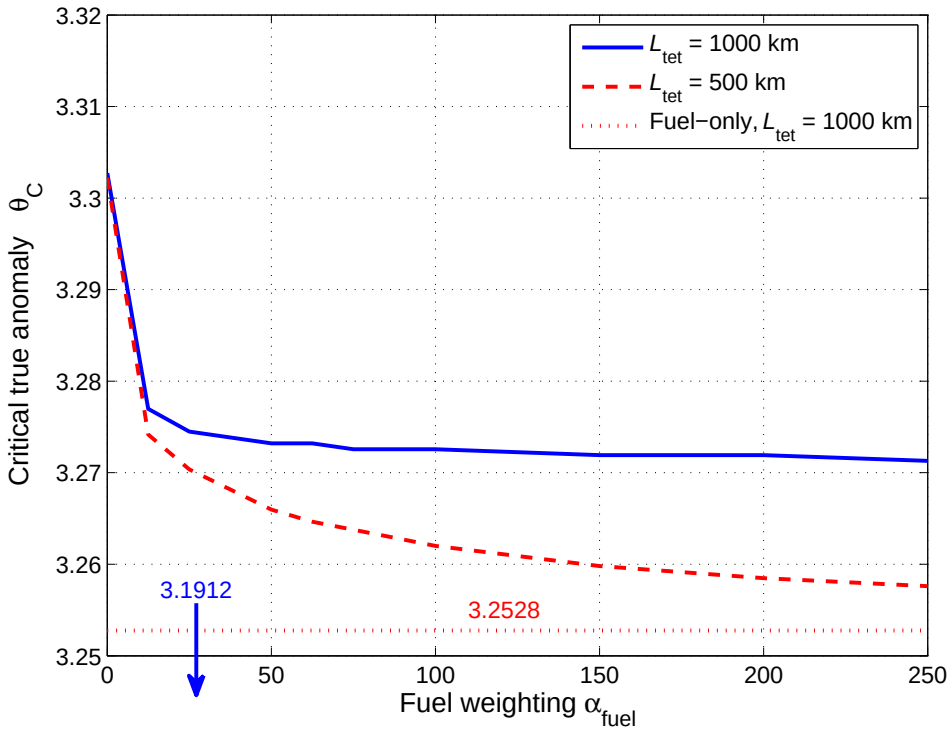

Figure 3.9: Critical true anomaly θ_C as a function of fuel weighting α_{fuel} for the initialization scenario for tetrahedron leg lengths of $L_{\text{tet}} = 1000$ km and $L_{\text{tet}} = 500$ km. This plot closely matches that of Figure 3.8(b), indicating that the data-taking capability is largely driven by the critical true anomaly for the selected formation.

The change in science cost J_{sci} for each formation leg length parallels the change in critical true anomaly θ_C at which the formation is a regular tetrahedron. This phenomenon is shown in Figure 3.9. Indeed, the parallel is not accidental, as the locally optimal solution J_{MMS} for the initialization problem quickly becomes dependent on fuel cost J_{fuel}. The critical true anomaly is a passive feature of the resultant tetrahedron which does not significantly correlate with fuel use. However, for the selected MC optimal parameterization Υ_{MC}, it is the primary driver for data-taking capability.

Now consider the second scenario, where the MC optimal formation Υ_{MC} with a

given tetrahedron leg length L_{tet} transits to a near-optimal formation Υ^* with leg length 25% shorter. This is closely related to the multiple-step MMS mission example considered in the next subsection. Here, however, only a single step is examined. The MC optimal formation parameterizations used in this example are scalings of those found for Υ_{MC} for the largest leg length, $L_{\text{tet}} = 1000$ km. The two cases considered are transitions L_{tet} : 1000 km $\rightarrow$ 750 km and L_{tet} : 500 km $\rightarrow$ 375 km. The central formation about which the search is conducted is therefore not guaranteed viable, but because the viable Monte Carlo search space is larger for the larger tetrahedron leg length, this MC optimal formation parameterization places the spacecraft near a parametric region that is likely to provide increased data-taking over that found through the more restrictive Monte Carlo search on the smaller tetrahedron leg length.

The minimum fuel and minimum science costs in transitioning from a MC optimal to a near-optimal formation exhibit vastly differing behavior from the initialization problem, as shown in Figure 3.10. In this case, because the MC optimal initial and final parameterizations are related, the general overall transitional cost is lower than for the initialization scenario. While this suggests that the science cost will preferentially dictate the optimal formation transition, the initial Monte Carlo formation is sufficiently specialized to provide significant data-taking that the transit fuel costs vary dramatically — for this problem, by a factor of more than 5 from the best to worst-case transition costs near the central parameterization for both leg lengths. By contrast, the science cost in each case varies by a factor of less than 2. As well, near the fuel minimum, the cost J_{fuel} is sensitive to small changes in the parameterization. This results in an incremental decrease in the total cost J_{MMS}, as the ratio of α_{sci} to α_{fuel} must significantly decrease to effect a change in the component costs. As in the initialization problem, convergence on the fuel-only solution is much quicker for the larger transition (L_{tet} : 1000

km $\rightarrow$ 750 km) than for the smaller transition (L_{tet} : 500 km $\rightarrow$ 375 km), but the science cost J_{sci} is only loosely correlated with the critical true anomaly θ_C.

For this and similar mission scenarios, the science and fuel costs are dictated by changes in the four single-spacecraft minimum fuel solutions. These single-spacecraft maneuvers effectively group a largely flat region of fuel cost into families of solutions in which almost all switching true anomalies have similar optimal values. Such families can reside near one another parametrically and exhibit strikingly different formation minimum fuel transit characteristics. The smaller transition is much more sensitive to this effect, with regions of fuel-optimal costs causing a high degree of nonlinearity near the global minimum. These families are shown in Figure 3.11, with groups distinguished by two or more of the spacecraft exhibiting clear changes in the optimal switch characteristics of at least two switching segments. This is overlaid on a plot of the total fuel cost, for a 33×33 grid for L_{tet} : 500 km $\rightarrow$ 375 km. Because this feature is generally not exhibited in the science cost J_{sci}, the total cost J_{MMS} decreases incrementally as it transitions from the region of lowest science cost to lowest fuel cost. Each incremental change represents a swift convergence on the local family minimum, with only negligible differences in Υ^* as a function of α_{fuel} discerned through additional iterations. This indicates that, for shorter transitions between solutions which reside near a minimum — either MC optimal or near-optimal parameterizations — a sparse number of fuel weightings α_{fuel} can be used to determine the critical behavior of the mixed-metric minimum cost function J_{MMS}.

3.6.2 Formation Optimal Maneuvers in Series

The previous subsection considered near-optimal, single steps which show the effects of varying fuel and science costs on formation capabilities. The features observed in those

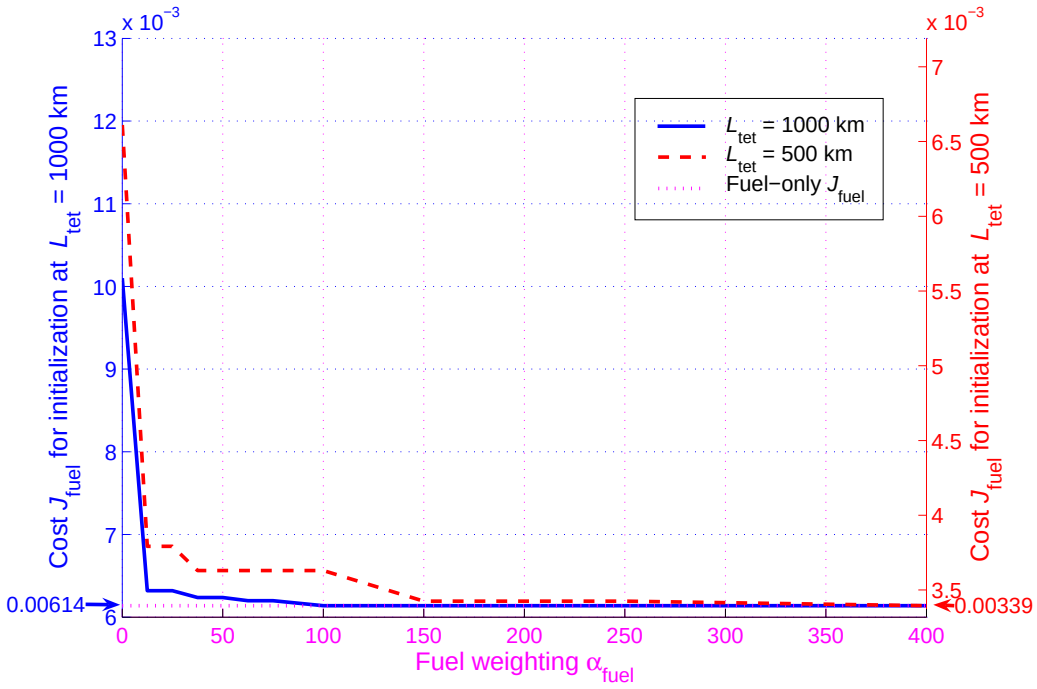

(a)

Figure 3.10: Costs associated with the transition from a Monte Carlo optimal formation parameterization to a near-optimal parameterization of smaller leg length. In (*a*), fuel cost J_{fuel} is shown for increasing α_{fuel} and fixed $\alpha_{\text{sci}} = -1/P$ for the transitions from L_{tet} : 1000 km $\rightarrow$ 750 km and L_{tet} : 500 km $\rightarrow$ 375 km. In (*b*), the same is shown for the associated science cost, J_{sci}. In each case, the blue solid line is associated with the left axes and the red dashed line is associated with the right axes. In (a) the single dotted line indicates the best-case fuel cost at $\alpha_{\text{sci}} = 0$ for both formation leg lengths.

Figure 3.11 (Continued)

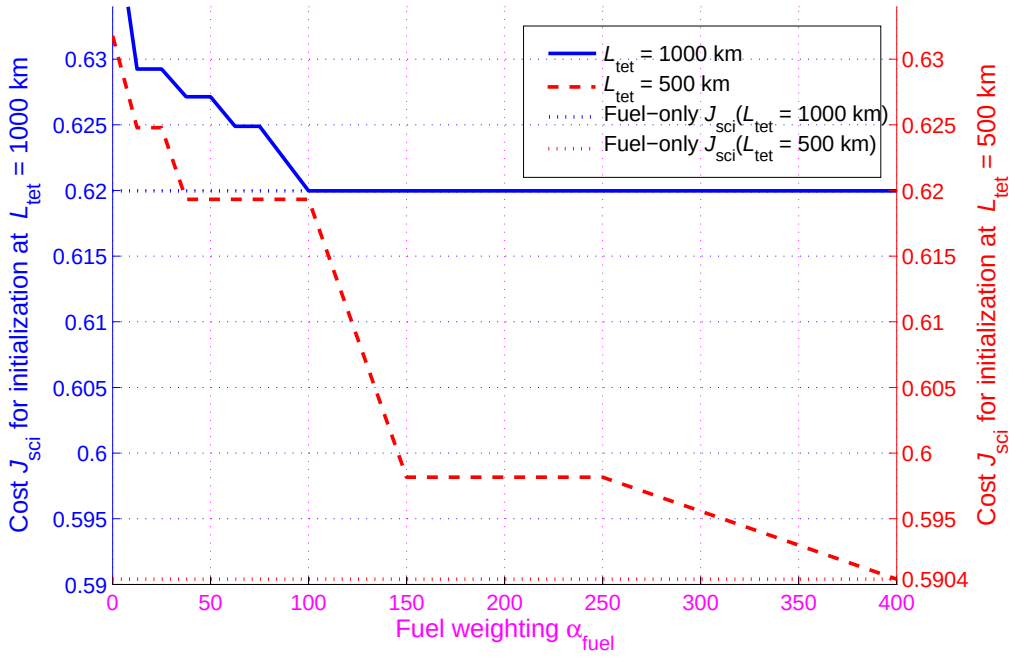

(b)

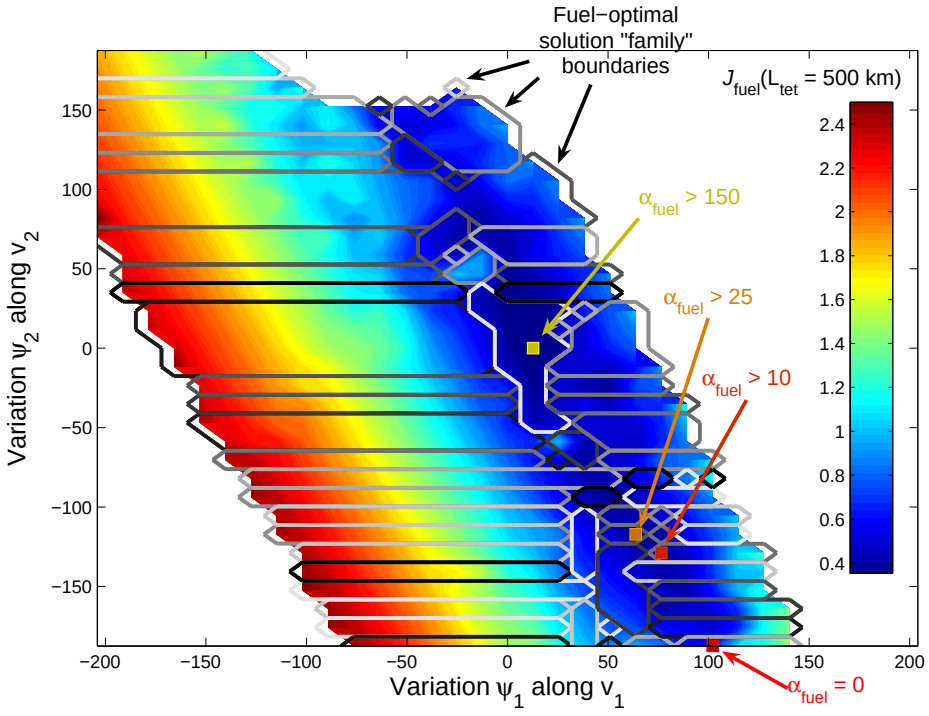

Figure 3.11: Locally small variations in parameterization can result in large changes in the fuel cost J_{fuel}. Families of solutions are outlined to show where the structure of the formation maneuver changes, distinguished by two or more spacecraft in the formation showing clear variations in at least two switching segments. The fuel cost can shift significantly across these boundaries due to large changes in the single-spacecraft minimum fuel solutions. This sensitivity causes the formation cost (squares) to vary incrementally rather than smoothly with α_{fuel}. The numbers indicate lower bounds on α_{fuel} for which the mixed-metric optimal J_{MMS} resides near the point. Further iterations resolve only small differences in solved parameterization which minimizes J_{MMS} near these points.

scenarios offer a general backdrop upon which to consider a series of maneuvers between MMS formations. This subsection examines the trade-offs which come with planning a complete mission using the mixed-metric cost function and show how the techniques described in the text can be used to develop a near-optimal maneuvering profile for the MMS mission.

The example considered in this subsection is modeled after the MMS-desired transitions from $L_{\text{tet}} = 1000$ km to $L_{\text{tet}} = 75$ km by decreasing the formation separation by 25% at each step — i.e., for an initial tetrahedron leg length $L_{\text{tet},0}$, a transit of $L_{\text{tet}} : L_{\text{tet},0} \rightarrow 0.75L_{\text{tet},0}$. While the MMS problem provides for optimal transitions down to $L_{\text{tet}} = 10$ km, computational precision for solving the minimum-fuel problem for a spacecraft with sufficient thrust to transit on the order of hundreds of kilometers in a single orbit is incapable of obtaining resolution which allows calculation of fuel-optimal solutions for transitions of less than approximately 25 km for the same spacecraft. As such, the data considered here examines transitions of at least 25 km, with the shortest resultant formation tetrahedron leg length $L_{\text{tet}} = 75$ km. As before, each parameterization Υ is partitioned into free and fixed parameters. Again, each element of the formation must be in a stable relative orbit ($p_4^i = 0,\ i \in [1, 2, 3, 4]$) and is centered about Spacecraft 1 at $\mathbf{x}_c = [0,\ 0,\ 0]^T$; the nominal initial relative positions of the spacecraft are as given in Table 3.1. A summary of these constraints and the resultant elements of Υ_{fixed} are provided in Table 3.2, along with these initial relative positions, as well as indicating the parameters are then left in the set Υ_{free}.

As in the single-step case, a Monte Carlo analysis is performed, and the parameterization corresponding to the lowest science cost for the formation leg length $L_{\text{tet}} = 1000$ km is chosen as the search space center. Note that, because an independent Monte Carlo analysis has been performed for this subsection, the optimal search directions and MC

Table 3.3: Free parameters in the set $\Upsilon^*_{\text{free}}(L_{\text{tet}} = 1000 \text{ km})$ which yield the scientifically maximal individual spacecraft formation solved by the Monte Carlo simulation for a stable formation of leg length $L_{\text{tet}} = 1000$ km (a). The resultant single-spacecraft parameter elements p^i_j are given in (b). Fixed parameters $\Upsilon^*_{\text{fixed}}(L_{\text{tet}} = 1000 \text{ km})$ for this problem are given in Table 3.2.

$\Upsilon_{\text{free}} = \{$	$(q_\phi, \mathbf{q})$	θ_C	(p^2_1, p^2_5)	(p^3_1, p^3_5)	$(p^4_1, p^4_5)\ \}$
$\Upsilon^*_{\text{free}}(L_{\text{tet}}) =$	$\begin{pmatrix} 157.129° \\ 0.7278 \\ 0.2440 \\ 0.6435 \end{pmatrix}$	3.3477	$\begin{pmatrix} 3935.19 \\ 38.5931 \end{pmatrix}$	$\begin{pmatrix} 2021.77 \\ -10.2121 \end{pmatrix}$	$\begin{pmatrix} 3064.49 \\ -113.556 \end{pmatrix}$

(a)

	Formation element i			
	$i = 1$	$i = 2$	$i = 3$	$i = 4$
p^i_1	0	3935.19	2021.77	3064.49
p^i_2	0	4032.9	2026.63	3160.94
p^i_3	0	103.113	7.2197	-379.826
p^i_4	0	0	0	0
p^i_5	0	38.5931	-10.2121	-113.556
p^i_6	0	37.4361	105.645	36.4195

(b)

optimal parameterization for each step in this process are not identical to those in the second previous subsection. Near-optimal mixed-metric parameterizations are obtained for the optimal formation cost J_{MMS} at each formation leg length by varying the final formation parameterization along the principal directions obtained from the Monte Carlo search. The bisecting multipath search is used with $N = 4$ — a 17×17 grid — over three iterations, with each refinement operating on a space 1/5 the original size. As in the previous examples, variations in parameterizations must be limited in order to successfully initiate the search. Prior to optimization, it is determined that, for the science-only cost, this corresponds to variations in the local search space along each parametric search direction about the MC optimal parameterization Υ_{MC} which allow for changes in p_1^i and p_5^i on the order of 1/3 the tetrahedron leg length.

This search is performed for several combinations of fuel and science weighting. Here, science weighting is held constant at $\alpha_{\text{sci}} = -1/P$ while $\alpha_{\text{fuel}} \in \{0,\ 27,\ 80,\ 320\}$ are considered, then the fuel-only case, which can be considered using $\boldsymbol{\alpha} = [0,\ \alpha_{\text{fuel}}]$ for any non-zero α_{fuel}, is solved. These examples probe the salient features of the mixed-metric cost J_{MMS}, including fuel-only and science-only weightings, for transitions which span leg length changes of more than 25 km. For all weightings $\boldsymbol{\alpha}$, the formation parameterization at each step must be viable, even if $\alpha_{\text{sci}} = 0$ in the mixed-metric cost J_{MMS}. In this way, intermediate parameterizations are all constrained by Equation 3.52. This guarantees that collision avoidance, spacecraft separation, and minimum data-taking window constraints are always accommodated even if the total data-taking capabilities of each formation are no longer of concern.

Similar to the single-step maneuver problem, a Monte Carlo simulation is performed to find a set of formations with high science cost for each relative spacecraft formation separation distance $L_{\text{tet}} \in [1000,\ 750,\ \ldots\ , 100,\ 75]$. This Monte Carlo data is used to

derive the two principal directions along which to search for the mixed-metric optimal solution to Equation 3.47, using parameterizations near the central parameterization according to Equation 3.56, for each $\boldsymbol{\alpha}$ and at each nominal tetrahedron leg length. This implies that the solved near-optimal parameterizations $\boldsymbol{\Upsilon}^*$ will be a function of both leg length and $\boldsymbol{\alpha}$. The initial parameterization is a near-optimal parameterization for $\boldsymbol{\alpha} = [-1/P, 0]$, denoted $\boldsymbol{\Upsilon}^*(L_{\text{tet}} = 1000 \text{ km})$, and is obtained by searching near the MC optimal parameterization $\boldsymbol{\Upsilon}_{\text{MC}}$ at that leg length along the two principal directions. This process replicates the initialization problem presented in the previous subsection. The intermediate and final parameterizations in this multi-step analysis provide general information which is useful for any chosen initial formation parameterization among those with large science cost at the largest leg length, $L_{\text{tet}} = 1000$ km. The initial parameterization, including the elements of the set $\boldsymbol{\Upsilon}^*_{\text{free}}(L_{\text{tet}} = 1000 \text{ km})$ and the single-spacecraft parameter elements p^i_j which describe the relative orbits or each spacecraft in the formation, is given in Table 3.3.

At each intermediate formation leg length, the initial parameterization used to derive a solution varies, depending on the previous solved formation optimal parameterization. It is therefore instructive to examine scientific efficacy and fuel independently, as well as in the context of these intermediate parameterizations. Figure 3.12 shows the variation in MMS data-taking capabilities over both $\boldsymbol{\alpha}$ and L_{tet} for the final formation parameterization, while Figure 3.13 shows the corresponding total formation transition costs, partitioned by spacecraft. It is unsurprising that, for the formations for which $\alpha_{\text{fuel}} = 0$, the science cost J_{sci} decreases slightly as the principal direction search probes in different MC optimal directions based on formation leg length; at each iteration, the data-taking capabilities are guaranteed to be no less than those cost at the current step so long as the formation remains viable. However, these improvements are minimal for $L_{\text{tet}} < 422$ km,

indicating the local parametric search space has been thoroughly probed.

For mixed-metric J_{MMS}, the relative weights of fuel and science dictate the large-scale behavior of the constituent costs only for the largest transitions. This is not true for the smaller transitions, which exhibit variations in J_{sci} and J_{fuel} which are partly a function of the solved formation-optimal parameterizations for all prior transitions. In Figure 3.13, the single-spacecraft fuel cost J^i_{fuel} is shown to differ significantly for some spacecraft in successive formation transits for which the fuel and science weightings remain constant. Because the transitions considered here are minimum-fuel over the formation, these single-spacecraft costs are accompanied in an individual transit by a corresponding decrease in cost incurred by another spacecraft. This can result in parametric changes which are adverse for subsequent transits. For example, with $\boldsymbol{\alpha} = [-1/P,\ 27]$, the burden on Spacecraft 2 is large, while the fuel-only case transfers some of this burden to Spacecraft 4. This shuffling of switch times saves ~ 1000 seconds of thrust application over each of the first four steps for the $\alpha_{\text{sci}} = 0$ case. However, the near-optimal solution for $\alpha_{\text{fuel}} > 27$ also shifts the formation into a new region during the transition L_{tet}: 422 km $\rightarrow$ 316 km, with both Spacecraft 2 and Spacecraft 4 incurring significant increases in fuel cost. This is a result of the local space of viable science formations constricting as a more fuel efficient path is chosen across these large initial steps. Subsequent formation transitions become *more* fuel-intensive than fuel-optimal formation transitions with larger α_{sci}. In this example, the pure fuel weighting outperforms the transitions for all $\alpha_{\text{sci}} = -1/P$ down to $L_{\text{tet}} = 422$ km by as much as 25%; however, the multi-step fuel cost to reach $L_{\text{tet}} = 316$ km results in a lower total fuel expenditure for $\alpha_{\text{fuel}} = 80$.

The science cost exhibits similarly undesirable behavior as a result of these fuel cost effects. In the worst case for a mixed-metric formulation, for $\boldsymbol{\alpha} = [-1/P,\ 320]$, the parameterization obtained for the mixed-metric optimal transition L_{tet} : 134 km $\rightarrow$ 100

km provides 32% smaller J_{sci} than the optimal formation obtained for $\boldsymbol{\alpha} = [-1/P,\ 0]$; the viewing time for the latter is 80% of the full orbit time, while the former gathers data for just 64% of each orbit. This decline in effectiveness is reflected in the near-optimal intermediate parameterization solutions $\boldsymbol{\Upsilon}^*$, which change in subtle but meaningful ways with $\boldsymbol{\alpha}$ and L_{tet}.

The most apparent of these is in formation rotation angle q_ϕ, which is highly dependent on the choice of $\boldsymbol{\alpha}$. In Figure 3.14(a), this angle is shown as a function of α_{sci} and the tetrahedron formation leg length. In this case, an increasing dependence on J_{fuel} alters the final rotation change by almost 6°, with variations in q_ϕ correlating well with a decline in science cost J_{sci}. It is important to note that this relationship is not entirely predictive, so that, for the final formation transition $L_{\text{tet}} = 100$ km $\rightarrow 75$ km with $\boldsymbol{\alpha} = [-1/P,\ 320]$, $J_{\text{sci}} = 0.5059$ increases even as the near-optimal formation rotation angle decreases. In this case, the solved parameter set $\boldsymbol{\Upsilon}^*$ for the fuel-weighted solution has significantly diverged from the solved parameter sets for smaller α_{fuel}. This parametric divergence is reflected more apparently in Figure 3.14(b), which indicates the critical true anomaly dips from $\theta_C \sim 3.32$ to $\theta_C \approx 3.26$ — a change of almost five hours and slightly less than 7% of the total orbit time — resulting in a critical true anomaly less than that of the solved fuel-only formation transitions. These changes drastically impact the data-taking capabilities of the formation. This region of significant change in θ_C also corresponds to the region in which fuel costs increase most significantly for large fuel weighting α_{fuel} in J_{MMS}. Taken together, these factors suggest for mission design purposes that, if the data-taking capability of the formation appears to suffer significantly over a multi-step problem, a parametric change is occurring. Because these parametric changes are often accompanied by increased overall fuel cost for successive transits, a slightly lower fuel cost weighting α_{fuel} may provide a solution which uses

only a small amount more fuel for a single transit but yields significant gains in both fuel and scientific data-taking over the long term.

For MMS mission planners, these observations regarding both fuel and science cost will enhance opportunities for generating tetrahedron formations which provide expansive data-taking capabilities while satisfying a realizable set of formation constraints and expending minimal fuel during transitions. This example illustrates several ways in which near-optimal formation parameterizations vary as the formation transits between orbits; understanding these variations, as well as their relationship with relative formation dynamics and problem constraints, is critical for evaluating similar tetrahedron-based multi-spacecraft missions.

3.7 Conclusions

The Magnetospheric Multiscale Mission is a four-spacecraft tetrahedron tasked with taking three-dimensional measurements of the Earth's magnetic field. This chapter studied the trade between the scientific goals of the tetrahedron in the context of mission constraints such as fuel use and collision avoidance concerns. A variety of elements were introduced to accomplish this task, with the objective of easing mission planning.

Relative formation dynamics near an elliptical orbit were introduced, and the optimization constraints using Hamilton-Jacobi-Bellman methods were established for repositioning a single spacecraft in this space. A useful parametric formulation for evaluating scientific data-taking capabilities of a tetrahedron formation was then provided. By partitioning the space into free and fixed parametric sets for useful data-taking, the problem was reduced from 24 variables relating single-spacecraft relative formation parameters to 16 variables, which are more easily visualized and manipulated to change the formation's utility. Near-linearization of these parameters was shown for scientific

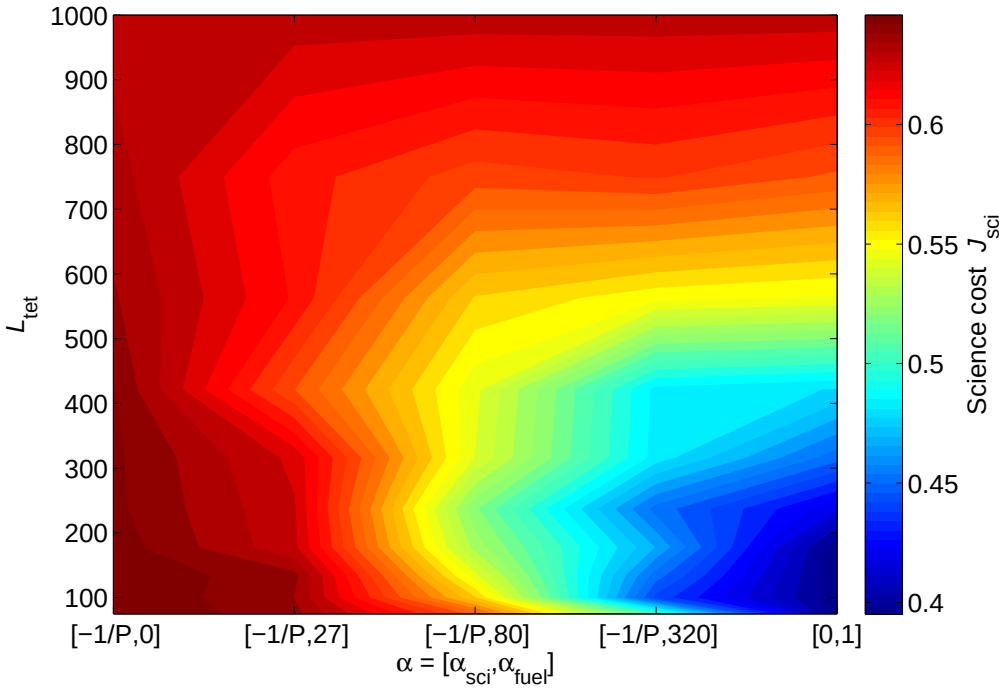

Figure 3.12: Science component of the formation cost J_{MMS} for the range of mixed-metric costs and tetrahedron formation leg lengths searched in the text. For problems in which both α_{fuel} and α_{sci} are non-zero, the fuel cost to complete large formation maneuvers initially allows for lower data-taking capabilities; at a critical leg length, the low cost of all formation maneuvers among the searched parametric variations allows for significant data-taking improvement.

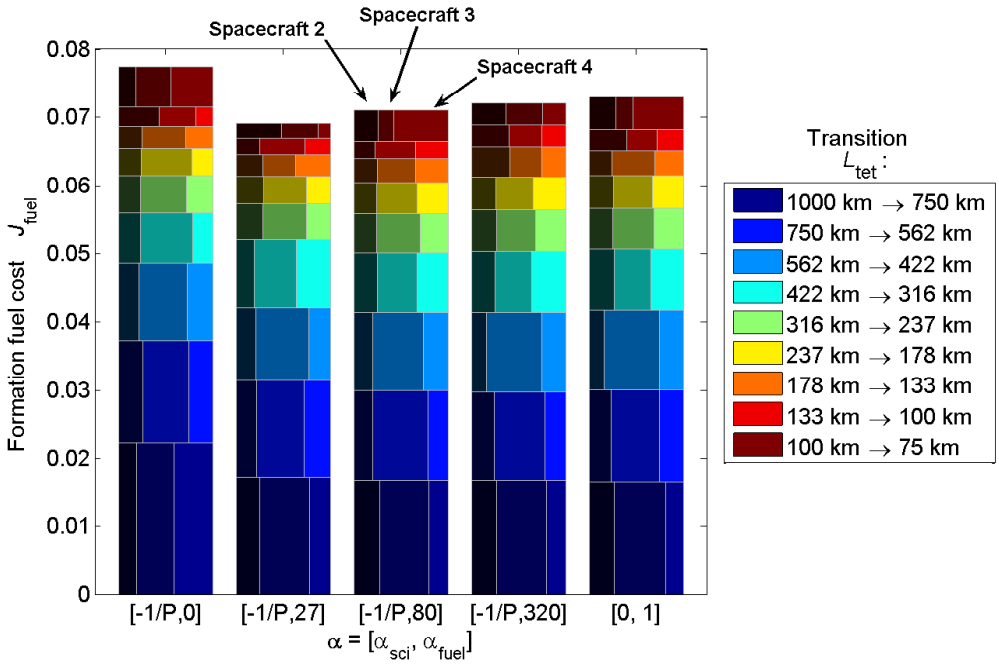

Figure 3.13: Fuel component of the formation cost J_{MMS} for the complete transition from $L_{\text{tet}} = 1000$ km to $L_{\text{tet}} = 75$ km. The horizontal partitions indicate fuel cost to complete each transition step, while the vertical partitions give the cost incurred by each spacecraft in that transition. Equal-area regions for single-spacecraft fuel cost indicate equal fuel use during transitions. For large transits, J_{fuel} shrinks as fuel weighting increases; however, these short-term decreases in fuel cost drive the formation to a region in which single-step fuel costs increase for transitions with large α_{fuel} after L_{tet} : 422 km → 316 km.

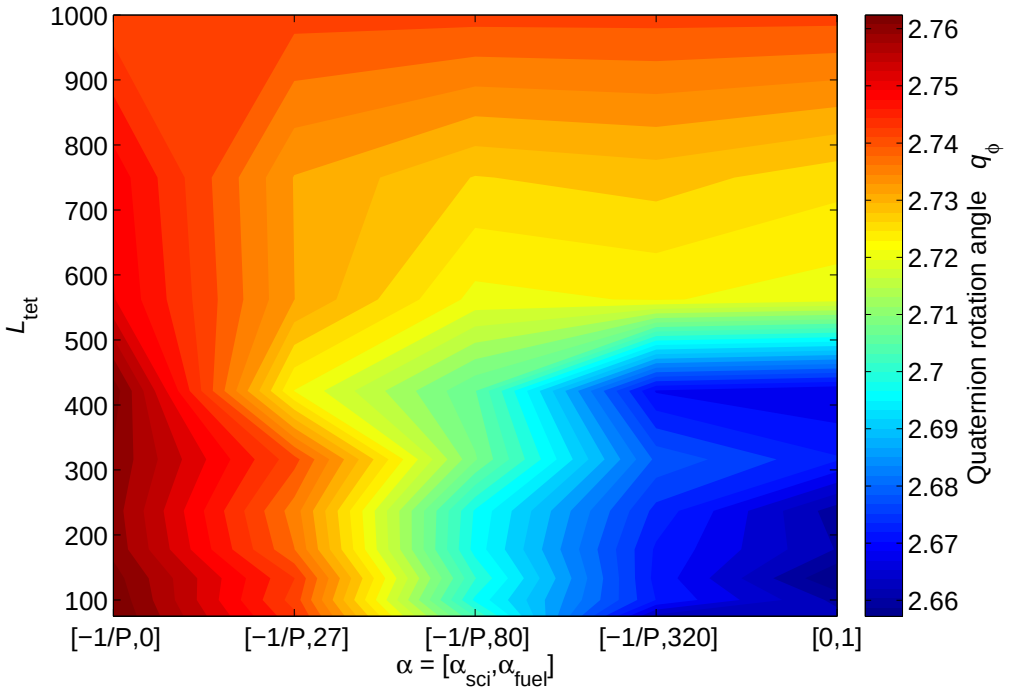

(a)

Figure 3.14: Quaternion rotation angle q_ϕ (a) and critical true anomaly θ_C (b) as a function of formation leg length L_{tet} and science weighting α_{sci}. (a) The formation rotation angle is up to 6° higher for the most effective data-taking formations than for the significantly fuel-weighted formations, with angle variations roughly corresponding to variations in J_{sci}. (b) This is related to a shift in the parametric solution, reflected in the critical true anomaly changing abruptly. The region of declining science value (marked) has critical true anomaly θ_C which is significantly different from the consistently high-J_{sci} formation parameterizations elsewhere.

Figure 3.14 (Continued)

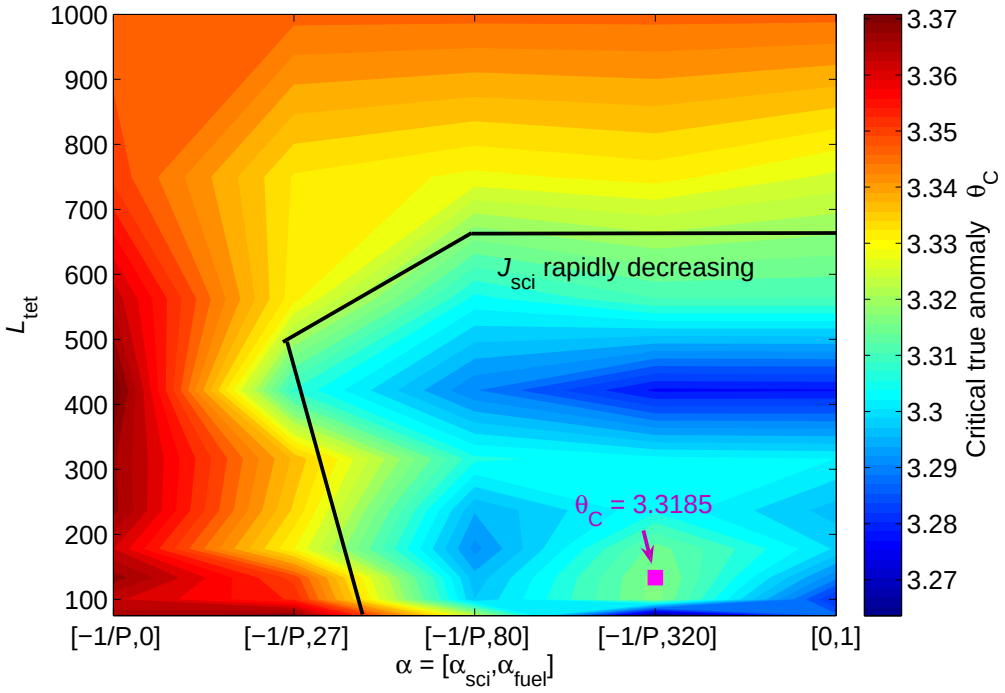

(b)

capabilities for a constrained problem of an MMS-like tetrahedron formation, and an easily implemented parametric direction search over a two-dimensional space was employed to evaluate a mixed-metric cost function involving both transitional fuel use and formation science data-taking.

By applying these methods to an MMS example, several features of both the formation and optimal solution for both single-step and multiple-step solutions were examined. In general, it was found that the inclusion of fuel cost in the mixed-metric cost function results in speedy convergence to the fuel-only solution for loosely constrained problems. As well, mission planners must exhibit caution if fuel cost is a primary mission driver in a series of transits, as viable formations at adjacent steps can be vastly different, and the fuel expenditure can increase rapidly. The results from these examples should act as a useful working blueprint for mission planning which will allow the MMS team to efficiently and effectively explore the Earth's magnetosphere.

Chapter 4: Formation Optimal Maneuvers under Inertial Attitude Dynamics

Abstract

A technique for generating optimal maneuvers for realistic thruster placements on rotating spacecraft in formations is developed. The approach uses linear programming optimization to initialize a Hamilton-Jacobi-Bellman optimization. The linear programming solution develops a fast and accurate solution for the discretized problem; the subsequent Hamilton-Jacobi-Bellman optimization minimizes the true continuous cost (such as formation fuel use). A Schur decomposition and singular value decomposition are employed to enhance the speed and robustness of the Hamilton-Jacobi-Bellman optimization. The resultant technique scales well with the number of thruster switches and is generally applicable to spacecraft whose inertial frame dynamics are known over one or more orbits. The approach is evaluated in simulation on a two-spacecraft cooperative inspection mission. Analysis is performed on a variety of potential strategies for choosing reference centers, stabilizing relative orbits, and decreasing orbit separation distance, showing excellent performance in both solution accuracy and fuel use while reducing computation time compared to traditional approaches.

4.1 Introduction

Autonomous satellite formations represent a means of accomplishing advanced mission objectives while reducing cost and extending mission life, and both NASA and the Department of Defense have shown interest in the continuing success of this technology[1, 3, 4, 17]. Missions range from Earth and deep space science to space-based radar, and

current defense research focuses on on-orbit docking and inspection. However, several challenges facing satellite clusters must be resolved, including fleet-wide communication, fault detection and tolerance issues, collision avoidance methods, and effective path planning and control in the presence of disturbances. This paper focuses on the last of these concerns by presenting a problem-solving methodology which can be applied to a wide range of planning and control scenarios.

Planning and control are often partitioned into two distinct modes, though the dynamics employed are typically similar, if not identical[22]. Formation maneuvering is considered the moving of the cluster of spacecraft from one desired formation to another. Formation keeping is a mode in which the spacecraft are controlled to remain in their current formation to within a specified tolerance in the presence of disturbances. Each of these problems must be fully understood — and the systems properly integrated — if autonomous satellite formations are to succeed in future missions. This paper addresses formation keeping when attitude constraints are present, a problem of particular relevance to inspection and docking missions[49].

Both formation keeping and close formation maneuvering rely on dynamics in a linearized relative reference frame. A review of both theoretical and practical solutions and applications for a single spacecraft in this frame is given in [20] and [21]. However, higher-order orbit descriptions[5, 50] and alternative linearizations[51] have also been used in some applications. One technique for controlling motion in the relative frame is the convex optimization approach developed by Tillerson *et al*[22, 23], in which the trajectory is discretized with true anomaly and a linear programming (LP) method employed to generate an optimal trajectory; this discretization can be applied to both formation keeping and formation maneuvering[41]. Due to constraints on the problem formulation, however, the LP method can be computationally intensive for long-term

or highly constrained problems. Hamilton-Jacobi-Bellman (HJB) optimality conditions have also been successfully used to develop time and fuel optimal maneuvers in the relative reference frame[16, 41]. This method guarantees that necessary conditions for optimality are satisfied and is most useful for solving problems in the relative reference frame about eccentric orbits when the optimization algorithm is initialized in the neighborhood of the optimal solution.

Algorithms for formation maneuvering using either of these methods have typically required the assumption that thrust can be generated in any direction[52, 53]. Planning methodologies with attitude constraints have been developed for systems near Lagrange points[54, 55], where slower, symmetric dynamics can be used advantageously. These techniques do not readily apply to the highly eccentric orbits demanded by missions such as Magnetospheric Multiscale[1]. One approach to circumventing this issue is to control thruster pointing during the maneuver, which was recently explored by Hall and Ross[56]. This method is largely intended for long-duration, minimum-time maneuvers with constant thrust and does not work well for spin-stabilized spacecraft or those in close proximity.

Formation maneuvering with attitude dynamics is closely associated with autonomous rendezvous and docking, which has a long history in the literature[6, 57, 58]. Much work on these missions has focused on vision systems, thruster control techniques, or mode switching and power allotment[59, 60, 61]. Some control and planning alternatives have also been explored which seek to limit fuel use in the presence of path constraints, but body dynamics are simplified in the interests of computability[62].

This paper explores a realistic formation maneuvering problem in which a spacecraft has multiple thrusters and undergoes attitude variations which are dynamically significant and predictable during maneuvering. For most small spacecraft, available

thrust is confined to specific directions and is subject to the kinematics of the spacecraft body. This paper develops a novel technique for formation maneuvering with attitude constraints by implementing a mixed linear programming/Hamilton-Jacobi-Bellman optimization scheme which utilizes a paired Schur decomposition and singular value decomposition to generate near-optimal maneuvers in the relative reference frame. This technique utilizes the benefits of both planning methodologies, namely the initializability of the LP method and the optimality and scalability of the HJB method. The approach can be applied to formations by including both spacecraft among the constraints, and a variety of problems can be probed which maximize mission life and effectiveness. The algorithm developed here is parallelizable across a cluster and scalable to larger problems, including those spanning multiple orbits. Unlike LP alone, the computation time of the mixed LP-*M*/HJB algorithm is approximately constant for a large class of problems, and the solution is not subject to discretization errors. Similarly, in contrast to the separate HJB formulation, initialization is easier, where a nearby solution which best satisfies state and costate constraints will nearly always be found, often in less time than using standard initializations of HJB.

Testing of this approach is performed on problems specific to the requirements of a proposed inspection mission in which attitude constraints are an important component. Sponsored by the Air Force Research Laboratory, the Cornell University NanoSat project (CU Sat) is a two-spacecraft inspection mission which demands both formation acquisition and long-term formation maintenance, as well as a variety of on-orbit maneuvers[15]. The spacecraft are spin-stabilized and typically operate within 50 meters of one another. Accessibility and testing of the technologies required for the completion of the CU Sat mission has been highly scrutinized in recent literature[36, 63], and CU Sat offers an opportunity to perform on-orbit verification of several autonomous

systems, including formation maneuvering algorithms.

The paper is presented in three parts. Section 4.2 introduces the formation maneuvering problem with attitude constraints and describes the dynamics necessary to generate near-optimal maneuvers in both HJB and LP formulations. Section 4.3 discusses both the Hamilton-Jacobi-Bellman and linear programming techniques, illustrating their application and advantages and disadvantages for use on the problem at hand. This section then describes the mixed formulation which can be used to solve problems in a way which takes advantage of the best properties of each. In Section 4.4, the specifications of the CU Sat mission are discussed. The combined technique is then employed on a variety of examples which relate to this mission.

4.2 Problem Definition

Consider a spacecraft undergoing relative motion with respect to a reference orbit which is subject to the dynamics of a gravitational field. Additionally, suppose this spacecraft has a finite number of thrusters which are fixed on the spacecraft body but not with respect to the inertial frame. The purpose of this work is to efficiently determine a fuel optimal maneuvering strategy for moving this spacecraft between two points in the relative reference frame.

The need for attitude constraints is inherent in the notion of thrusters whose positions are time-dependent. In order to solve this problem, three elements must be considered: (1) gravitational dynamics of the spacecraft in the relative reference frame; (2) rotational dynamics of the body frame with respect to the relative reference frame; and (3) planning strategies typically using optimization tools. This paper primarily focuses on the first and third of these elements while assuming the spacecraft undergoes a prescribed rotation. However, the methods described are flexible enough to incorporate any variety

of time-dependent spacecraft motion. The addition of torque effects by the thrusters on the spacecraft body rotation creates a significantly more complex problem which the current formulation can handle, but with an added computational expense.

4.2.1 Relative Dynamics

Determination of optimal planning maneuvers with attitude constraints depends on a description of the spacecraft's state in proximity to a known elliptical reference orbit. The dynamics governing a body in motion near such an orbit are given in [14], [29], and [30]. Generally, the equations of motion for a satellite with thrust-to-mass ratio **u** near a reference orbit which is in a general force field $f(\mathbf{R})$ are given by

$$\ddot{\mathbf{r}} = -f(\mathbf{R})\mathbf{r} - f'(\mathbf{R})\left(\frac{\mathbf{R}\cdot\mathbf{r}}{|\mathbf{R}|}\right)\mathbf{R} + \mathbf{u} \tag{4.1}$$

where $\mathbf{R} \in \mathbb{R}^{3\times1}$ is the position of a reference satellite with respect to gravitational body and $\mathbf{r} \in \mathbb{R}^{3\times1}$ is the relative position of the spacecraft from this reference, such that $|\mathbf{r}| \ll |\mathbf{R}|$.

Transforming via the angular velocity of the reference orbit, the relative dynamics can be linearized as a function of the reference orbit true anomaly θ rather than time. Humi[30] introduces the transformed coordinate $\mathbf{z}(\theta) = [y_1 \quad v_1 \quad y_2 \quad v_2 \quad y_3 \quad v_3]^T$ and shows

$$\mathbf{z}'(\theta) = \begin{bmatrix} 0 & 1 & 0 & 0 & 0 & 0 \\ 0 & 0 & 0 & 2 & 0 & 0 \\ 0 & 0 & 0 & 1 & 0 & 0 \\ 0 & -2 & G[\omega(\theta)] & 0 & 0 & 0 \\ 0 & 0 & 0 & 0 & 0 & 1 \\ 0 & 0 & 0 & 0 & -1 & 0 \end{bmatrix} \mathbf{z}(\theta) + \omega(\theta)^{-\frac{3}{2}} \begin{bmatrix} 0 & 0 & 0 \\ 1 & 0 & 0 \\ 0 & 0 & 0 \\ 0 & 1 & 0 \\ 0 & 0 & 0 \\ 0 & 0 & 1 \end{bmatrix} \mathbf{u}(\theta) \quad (4.2)$$

where $(\cdot)'$ denotes differentiation with respect to true anomaly. This is a linear system that can be written

$$\mathbf{z}'(\theta) = A(\theta)\mathbf{z}(\theta) + B(\theta)\mathbf{u}(\theta) \quad (4.3)$$

The solution to this linear system is

$$\mathbf{z}(\theta) = \Phi(\theta)\Phi^{-1}(\theta_0)\mathbf{z}(\theta_0) + \Phi(\theta)\mathbf{Q}[\theta_0, \theta] \quad (4.4)$$

Closed-form solutions for the fundamental matrix solution $\Phi(\theta)$ and its inverse are as given by Carter[13]. The vector $\mathbf{Q}[\theta_0, \theta]$ is the thrust effect vector

$$\mathbf{Q}[\theta_0, \theta] = \int_{\theta_0}^{\theta} \Phi^{-1}(\tau)B(\tau)\mathbf{u}\, d\tau \quad (4.5)$$

and can be solved in closed-form as given by Zanon and Campbell[41]. This solution is valid for elliptical orbits ($0 \leq e < 1$), though its precision falls off as $e \to 1$.

The system can be described in the relative reference frame by

$$x_1(\theta) = \frac{p_1}{\rho(\theta)} + \left(\frac{1}{\rho(\theta)} + 1\right)(ep_2 \cos\theta + p_3 \sin\theta) + p_4\left[2e\tilde{J}(\theta)\rho(\theta)\right] \quad (4.6)$$

$$x_2(\theta) = p_3 \cos\theta - ep_2 \sin\theta - p_4\left[\frac{e\cos\theta}{\rho(\theta)^2} - 2e^2\tilde{J}(\theta)\right] \quad (4.7)$$

$$x_3(\theta) = p_5\frac{\sin\theta}{\rho(\theta)} + p_6\frac{\cos\theta}{\rho(\theta)} \quad (4.8)$$

where $\rho(\theta) = 1 + e\cos\theta$ and

$$\tilde{J}(\theta) = \frac{\sin\theta}{\rho(\theta)} - 3e(1-e^2)^{-\frac{5}{2}}\left[\frac{E}{2} - \frac{1}{2}\sin E\cos E - \frac{e}{3}\sin E^3\right] \tag{4.9}$$

with E the eccentric anomaly. In angular velocity-weighted $\mathbf{z}$ coordinates, where $\mathbf{y} = \omega(\theta)^{\frac{1}{2}}\mathbf{x}(\theta)$ and using $\omega(\theta) = \frac{\rho(\theta)^2}{C^2}$, this can be written simply in terms of the fundamental matrix solution:

$$\mathbf{z}(\theta) = \Phi(\theta)C^{-1}\begin{bmatrix} -ep_2 \\ -p_3 \\ p_4 - ep_3 \\ p_1 \\ ---- \\ p_6 \\ p_5 \end{bmatrix} \tag{4.10}$$

The relative frame definition shows the effects of parameter p_1, which gives the center of the motion; the pair (p_2, p_3), which define an effective radius to the in-plane motion; and a radius-defining pair (p_5, p_6) for the cross axis. Figure 4.1 illustrates the formation parameter definitions in the relative reference frame $\mathbf{x}^R$. A *stable orbit* is defined as one for which $\mathbf{z}(\theta) = \mathbf{z}(\theta + 2\pi)$ for all true anomalies θ. For these orbits, the sixth parameter p_4, which defines the instability of the system, is identically 0. For unstable orbits, p_4 may take any value.

4.2.2 Satellite Rotations

The gravitational dynamics relative to a reference orbit outlined in the previous section are sufficient to describe the state of the origin of a body axis coordinate frame, but they do not capture the motion of the axes themselves. In particular, most optimal planners

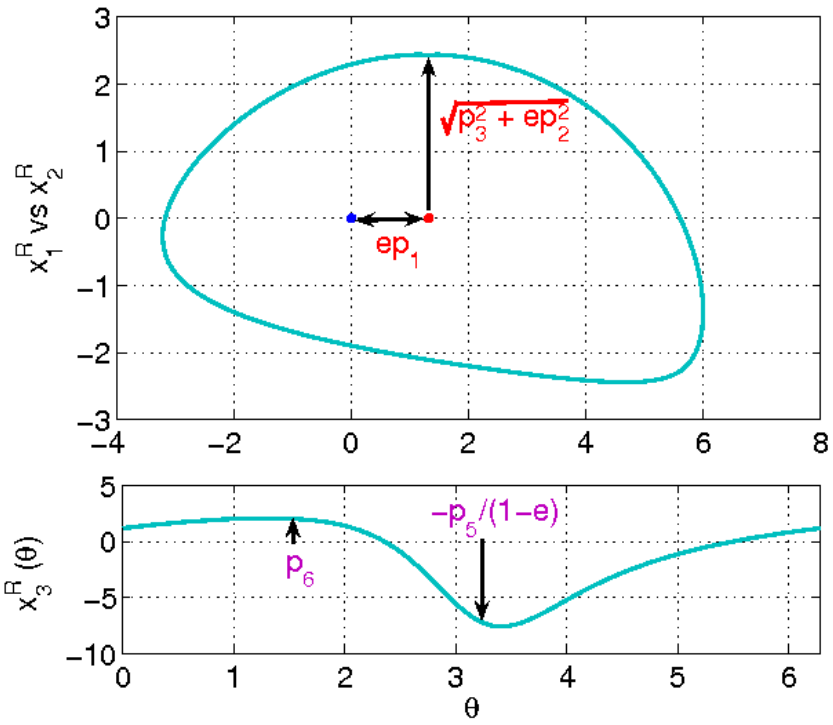

Figure 4.1: Conceptual definitions of the stable parameter set **P** as they relate to relative reference true anomaly θ. The superscript R refers to the relative reference frame (see Figure 4.2). The planar center is located at ep_1, the approximate ellipse radius for planar motion is $\sqrt{p_3^2 + (ep_2)^2}$. In the cross axis, a combination of p_5 and p_6 governs the motion.

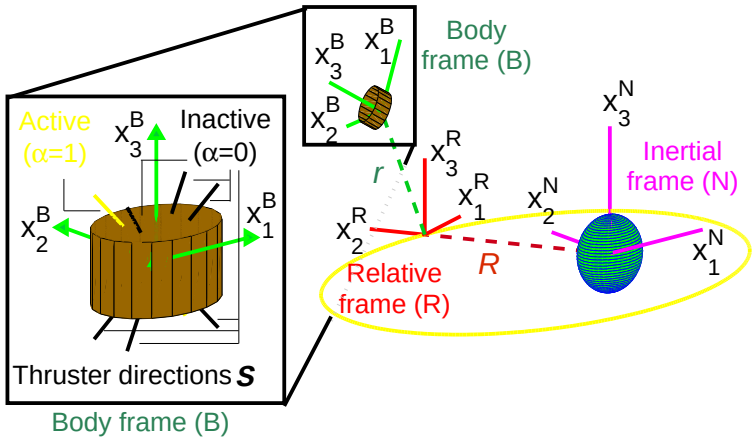

Figure 4.2: The relevant coordinate frames for the problem definition are the body frame (*B*) in which the spacecraft thrusters are defined; the relative orbit reference frame (*R*) from which the spacecraft's motion in the gravitational field is considered; and the inertial frame (*N*) centered about the Earth.

do not account for spacecraft rotations which affect the magnitude and direction of the thrust effects. Because these are bound to the internal dynamics of the spacecraft, it is necessary to incorporate them into the planning methodology.

Consider a spacecraft as shown in Figure 4.2. The spacecraft position is defined about a gravitational center as $\mathbf{x}^N$, or in proximity to a reference orbit as $\mathbf{x}^R$. The spacecraft has m discrete thrusters with maximum thrust-to-mass output u_{max} which are located independent of the relative reference axes and fixed in the body frame with directions $\mathbf{x}^B_{1-m}$; it is further assumed that the body axes exhibit some form of rotational motion with respect to the relative coordinate frame, and that this rotation is known *a priori*. Practically, this typically means a separate controller is used to maintain a specified attitude or rotation rate, which is a common occurrence. In this case, the 3×1 thrust

vector $\mathbf{u}(\theta)$ is written as

$$\mathbf{u}(\theta) = T(\theta)\mathcal{S}\boldsymbol{\alpha}(\theta) \tag{4.11}$$

where the $3\times m$ matrix $\mathcal{S}$ is the body frame direction of the applied force from each thruster:

$$\mathcal{S} = [s_1 \; s_2 \; \ldots \; s_m] \tag{4.12}$$

The $m \times 1$ vector $\boldsymbol{\alpha}$ then indicates the thrust applied by each thruster, bounded by $[0, |u_{max}|]$. The matrix $T(\theta) \in \mathbb{R}^{3\times3}$ is a three-axis rotation matrix defining the orientation of the spacecraft body with respect to the linearized reference coordinate frame. If T is only known as a function of time, the relation with true anomaly is found through

$$\omega_n t = E - e\sin E \tag{4.13}$$

$$\cos E = \frac{\cos\theta + e}{1 + e\cos\theta}$$

$$\sin E = \frac{\sqrt{1-e^2}\sin\theta}{1 + e\cos\theta} \tag{4.14}$$

where ω_n is the reference orbit mean motion or natural frequency, e is the reference eccentricity, and E is the eccentric anomaly of the reference orbit.

Due to the time-varying nature of the matrix $T(\theta)$, the thrust integral $\mathbf{Q}$ in Equation 4.4 cannot in general be computed in closed form. However, as shown in [16], an approximation of the integrands can be defined using a piecewise polynomial spline to approximate the integrand of the thrust effect integral. Because polynomials are readily integrated, a sufficiently good approximation to this integrand yields a good approximation to the integral itself. For the purposes of this discussion, it is assumed that $\boldsymbol{\alpha}(\theta)$ is piecewise constant, such that the unmultiplied spline integral becomes

$$Q[\theta_{j-}, \theta_{j+}] \approx \int_{\theta_{j-}}^{\theta_{j+}} \Phi^{-1}(\theta) B(\theta) T(\theta) d\theta \tag{4.15}$$

This is a 6×3 matrix for which the actual thrust effect over some interval $[\theta_1, \theta_2]$ is found by

$$\mathbf{Q}[\theta_{j-}, \theta_{j+}] = Q[\theta_{j-}, \theta_{j+}] \mathcal{S} \boldsymbol{\alpha}_j \tag{4.16}$$

For $T(\theta) = I$, which corresponds to axial thruster pointing, Q can be found in closed form using the equations derived in [41]. Comparative studies of this closed-form result with those given by spline approximations show that a piecewise polynomial utilizing 256 intermediate points yields a solution accurate to $\lesssim 10^{-5}$m in final position error for planning on maneuvers traversing 100m in one orbit at eccentricites of $e = 0.8$. A complete discussion of the properties of spline interpolations can be found in [31] and [32].

If the time-varying function $\boldsymbol{\alpha}(\theta)$ is taken to be piecewise constant with n_p segments, the state equation can then be recast in a more general form as

$$\mathbf{z}(\theta) = \Phi(\theta)\Phi^{-1}(\theta_0)\mathbf{z}(\theta_0) + \Phi(\theta) \sum_{j=1}^{n_p} Q[\theta_{j-}, \theta_{j+}] \mathcal{S} \boldsymbol{\alpha}_j \tag{4.17}$$

This corresponds to a series of thrust applications in which all time dependencies are resolved in the spline integral Q. Further specifying this as a set of switches performed by each thruster, the state equation becomes

$$\mathbf{z}(\theta) = \Phi(\theta)\Phi^{-1}(\theta_0)\mathbf{z}(\theta_0) + \Phi(\theta) \sum_{i=1}^{m} \sum_{j=1}^{n_{p,i}} Q[\theta_{i,j-}, \theta_{i,j+}] \mathbf{s}_i \boldsymbol{\alpha}_{i,j} \tag{4.18}$$

where $\mathbf{s}_i$ is the ith column of $\mathcal{S}$ and gives the body frame position of the ith thruster. Notice that n_p is potentially different for each thruster, as each thruster switches indepen-

dently of the others. As well, the spline integral Q can be generated for any time-varying attitude over any number of orbits.

4.3 Fuel Optimal Planners with Attitude Constraints

Minimizing a fuel cost is appropriate during both formation maneuvering and formation keeping. The minimum fuel cost function is generally given as

$$J_{F,u} = \int_{\theta_0}^{\theta_F} |\mathbf{u}(\theta)|\omega(\theta)^{-1}\, d\theta \tag{4.19}$$

with $\omega(\theta)$ relating the time and true anomaly differentials:

$$dt = \sqrt{\frac{a^3}{\mu}}\frac{(1-e^2)^{\frac{3}{2}}}{\rho(\theta)^2}\, d\theta = \omega(\theta)^{-1}\, d\theta \tag{4.20}$$

When multiple thrusters whose positions are not fixed in the relative reference frame are available, this may not capture the desired cost for a maneuver. The more general cost function considered here is

$$J_F = \int_{\theta_0}^{\theta_F} |\boldsymbol{\alpha}(\theta)|\omega(\theta)^{-1}\, d\theta \tag{4.21}$$

with $\boldsymbol{\alpha}(\theta)$ defined in Equation 4.11. In the case where no active thruster generates a force along any axis which opposes that generated by any other active thruster along that axis, Equation 4.21 reduces to Equation 4.19.

Solving for thrust profiles using this cost function allows several solution approaches. One method assumes a thrust profile and solves using Hamilton-Jacobi-Bellman (HJB) optimality conditions. This technique has the advantage of finding the locally optimal point — and often a globally optimal point — if the optimization converges; it also

scales well with maneuver type, including variations in thruster performance, eccentricity, number of spacecraft, and available thrust[16]. The primary disadvantage of HJB, however, is that a poor initial guess will often lead to convergence to a point which is not globally optimal; this becomes an issue for more complex maneuvers such as those proposed here with attitude constraints. A second method for solving minimum fuel problems discretizes the temporal space and solves for the thrust using a linear programming (LP) technique[64, 23]. The LP method easily incorporates inequality and equality constraints, and advances in LP solvers have led to relatively speedy solution times for a large class of problems. However, the method does not scale well computationally, particularly as more points are added to account for maneuver length, eccentricity, and thruster performance, or as the number of available thrusters and spacecraft increases.

It is proposed here to develop a formation planning methodology that integrates the HJB and LP solution techniques into a more useful solver which retains most of the advantages of each, with few of the disadvantages. The proposed mixed LP-*M*/HJB solution approach scales better computationally than LP while retaining its allowances for equality and inequality constraints. The proposed mixed LP-*M*/HJB algorithm also retains the optimality guarantees of HJB while providing an effective initialization. The remainder of this section presents the LP and HJB planner solutions, followed by the unique, mixed LP-*M*/HJB planning methodology.

4.3.1 Hamilton-Jacobi-Bellman Optimization

Similar to the optimal planner developed by Zanon and Campbell[16], the Hamilton-Jacobi-Bellman solutions considered here assume *bang-off-bang* thrust, beginning at true anomaly θ_0 and ending at true anomaly θ_F. This constraint also exists inherently in many applications such as CU Sat, which uses pulsed-plasma thrusters (PPTs) in-

capable of partial thrusting[25]. The optimal Hamilton-Jacobi-Bellman method begins by augmenting the cost function given in Equation 4.21 with the dynamics and thrust definitions using Lagrange multipliers:

$$\begin{aligned} J_F &= \int_\theta \Big(|\boldsymbol{\alpha}(\theta)|\omega(\theta)^{-1} + \boldsymbol{\lambda}_1(\theta)^T \left[\mathbf{z}'(\theta) - A(\theta)\mathbf{z}(\theta) - B(\theta)\mathbf{u}(\theta)\right] + \\ &\qquad \boldsymbol{\lambda}_2(\theta)^T \left[\mathbf{u}(\theta) - T(\theta)\mathcal{S}\boldsymbol{\alpha}(\theta)\right] \Big)\, d\theta \end{aligned} \tag{4.22}$$

Taking the variation with respect to both $\boldsymbol{\alpha}$ and $\mathbf{u}$ yields the following necessary conditions:

$$\boldsymbol{\lambda}_2^T(\theta) = \boldsymbol{\lambda}_1^T(\theta)B(\theta) \;\; \forall\, \theta \tag{4.23}$$

$$\boldsymbol{\lambda}_1'(\theta) = -A^T(\theta)\boldsymbol{\lambda}_1(\theta) \;\; \forall\, \theta \tag{4.24}$$

$$\begin{aligned} \boldsymbol{\lambda}_2^T(\theta)T(\theta)\mathbf{s}_i &= -\omega(\theta)^{-1} \;\; \forall\, \theta = \{\theta^*_{i,j-}, \theta^*_{i,j+}\}, \\ &\qquad i = \text{index of switching thruster} \end{aligned} \tag{4.25}$$

where $\theta^*_{i,j-}$ represents the true anomaly at which the jth segment of the ith thruster begins and $\theta^*_{i,j+}$ is the true anomaly at which this segment ends. As before, $\mathbf{s}_i$ is the body frame direction vector associated with that thruster. Notice that the same condition must be satisfied when the thruster turns on or off, which means these conditions are not sufficient for optimality. However, Equation 4.25 need not be satisfied at the endpoints $\theta = \{\theta_0, \theta_F\}$ of the period in which the maneuver occurs. The series of switches must also result in the desired final state from Equation 4.18. Solving Equations 4.23-4.25 for $\boldsymbol{\lambda}_1$ and setting $\boldsymbol{\lambda} = \boldsymbol{\lambda}_1$, this reduces to

$$\boldsymbol{\lambda}'(\theta) = -A^T(\theta)\boldsymbol{\lambda}(\theta) \quad \forall\, \theta \tag{4.26}$$

$$\boldsymbol{\lambda}^T(\theta)B(\theta)T(\theta)|u_{max,i}|s_i = -\omega(\theta)^{-1} \quad \forall\, \theta = \{\theta^*_{i,j-}, \theta^*_{i,j+}\} \tag{4.27}$$

Solving Equation 4.26, the value of $\boldsymbol{\lambda}(\theta)$ at any true anomaly is related to the initial value of $\boldsymbol{\lambda}_0$ by

$$\boldsymbol{\lambda}(\theta) = \Psi(\theta)\Psi^{-1}(\theta_0)\boldsymbol{\lambda}_0 \tag{4.28}$$

with $\Psi(\theta)$ and its inverse as given by Carter[13] and $\boldsymbol{\lambda}(\theta) \in \mathbb{R}^{6\times 1}$.

For a maneuver with $n_p^s = \sum_{i=1}^{m} n_{p,i}$ switches, it is then possible to write the switching relations from Equation 4.27 in compact matrix form as

$$K(\theta^*_{1,1-}, \theta^*_{1,1+}, \ldots, \theta^*_{m,n_{p,m}-}, \theta^*_{m,n_{p,m}+})\boldsymbol{\lambda}_0 = \boldsymbol{\Omega}(\theta^*_{1,1-}, \theta^*_{1,1+}, \ldots, \theta^*_{m,n_{p,m}-}, \theta^*_{m,n_{p,m}+}) \tag{4.29}$$

where K is then an $2n_p^s \times 6$ matrix and $\boldsymbol{\Omega}$ is a column vector with $2n_p^s$ elements. Each set of $2n_{p,i}$ block rows of this matrix relation is associated with the switches for one thruster. The jth row of the ith block of the matrix K is given by two rows:

$$K_{i,j} = \begin{bmatrix} \mathbf{s}_i^T T^T(\theta^*_{i,j-})B^T(\theta^*_{i,j-})\Psi^T(\theta^*_{i,j-})\Psi^{-T}(\theta_0) \\ \mathbf{s}_i^T T^T(\theta^*_{i,j+})B^T(\theta^*_{i,j+})\Psi^T(\theta^*_{i,j+})\Psi^{-T}(\theta_0) \end{bmatrix} |u_{max,i}| \tag{4.30}$$

Likewise, the jth element of $\boldsymbol{\Omega}$ associated with the block belonging to the ith thruster is the pair $\boldsymbol{\Omega}_{i,j} = \left[-\omega(\theta^*_{i,j-})^{-1},\ -\omega(\theta^*_{i,j+})^{-1}\right]^T$. If either $\theta^*_{i,j-} = \theta_0$ or $\theta^*_{i,j+} = \theta_F$, the corresponding row of K may be set to six zeros, along with the proper element of $\boldsymbol{\Omega}$.

For maneuvers that last less than one orbit in length and for which $T(\theta) = I$, $n_p^s \leq 6$[16, 18]. In general, however, $n_p^s > 6$, resulting in an overdetermined system which must be solved numerically. The solutions presented here use the Schur decomposition to find a numerically stable value for the vector $\boldsymbol{\lambda}_0$, then compute a singular value decomposition to isolate the linearly independent rows and ensure the costate equations are satisfied to desired precision.

For the remainder of this discussion, dependence of K and Ω on the switch times $\boldsymbol{\Theta} = \{\theta^*_{1,1-}, \cdots, \theta^*_{m,n_{p,m}+}\}$ is implied for the sake of simplicity. Pre-multiplying Equation 4.29 by K^T results in

$$K^T K \boldsymbol{\lambda}_0 = K^T \boldsymbol{\Omega} \tag{4.31}$$

Taking a Schur decomposition of the matrix $K^T K$ results in orthonormal matrix $Q \in \mathbb{R}^{6\times6}$ and diagonal matrix $D \in \mathbb{R}^{6\times6}$ such that

$$QDQ^T \boldsymbol{\lambda}_0 = K^T \boldsymbol{\Omega} \tag{4.32}$$

This is similar to finding a pseudo-inverse of $K^T K$, but the diagonal D holds on the eigenvalues of the system. This is then inverted to solve for $\boldsymbol{\lambda}_0$:

$$\boldsymbol{\lambda}_0 = QD^{-1}Q^T K^T \boldsymbol{\Omega} \tag{4.33}$$

This is useful for iterative solving of the costate equation for a $\boldsymbol{\lambda_0}$ while satisfying the constraints because, as shown by Wielandt and Hoffman[65], if the matrix K varies by a small amount, the variation in eigenvalues in D found through the Schur decomposition will be bounded by $||K||^2$. Even when the matrix D is nearly singular, this limits the variations in the value of $\boldsymbol{\lambda}_0$ for successive steps in an iterative solver, allowing numerically stable calculation of a Jacobian and Hessian.

The value determined for $\boldsymbol{\lambda}_0$ (Equation 4.33) using a Schur factorization can then be used to solve for the switching true anomalies in Equation 4.29. Performing a singular value decomposition on the left-hand side of Equation 4.29 yields

$$U\Sigma V^T \boldsymbol{\lambda}_0 = \boldsymbol{\Omega} \tag{4.34}$$

where $U \in \mathbb{R}^{2n_p^s \times 2n_p^s}$ and $V \in \mathbb{R}^{6\times 6}$ are orthonormal matrices and $\Sigma \in \mathbb{R}^{2n_p^s \times 6}$ holds the six singular values of the matrix K along its top diagonal. Substituting the initial condition of the costate based on the Schur decomposition, multiplying by U^T, and collecting the terms yields

$$\Sigma V^T Q D^{-1} Q^T K^T \boldsymbol{\Omega} = U^T \boldsymbol{\Omega} \tag{4.35}$$

It is noted that the matrix D must be invertible in this equation. If it is not, the HJB solution does not have six linearly independent relations, and the vector $\boldsymbol{\lambda}_0$ is much harder to determine or does not exist.

In an iterative solver, the objective is to satisfy Equation 4.35 to within numerical precision. The kth step of the iteration results in a residual vector $\boldsymbol{\delta}_k$, such that

$$(\Sigma_k V_k^T Q_k D_k^{-1} Q_k^T K_k^T - U_k^T)\boldsymbol{\Omega}_k = \boldsymbol{\delta}_k \tag{4.36}$$

This formulation can be used in any optimization procedure in which an input vector ($\not\leq$) is used to drive the residual vector $\boldsymbol{\delta} \to 0$. As long as D_k is invertible, the computed value of $\boldsymbol{\lambda}_{0,k}$ varies continuously for small changes in the set of switch true anomalies $\boldsymbol{\Theta}$. This property aids — but does not guarantee — convergence to the optimal true anomaly set $\boldsymbol{\Theta}^*$ in most off-the-shelf solvers.

4.3.2 Linear Programming Optimization

The optimal linear programming (LP) approach first discretizes the control input with M segments over true anomalies $\{\theta_1, \theta_2, ..., \theta_M\}$. Stacking control segments from m thrusters at each of the M true anomalies yields a vector of length $h = m \cdot M$. This is represented as

$$\boldsymbol{\aleph} = [\boldsymbol{\alpha}(\theta_1)^T \;\; \boldsymbol{\alpha}(\theta_2)^T \;\; ... \;\; \boldsymbol{\alpha}(\theta_M)^T]^T \;\in\; \mathbb{R}^{h\times 1} \tag{4.37}$$

Assuming that each discrete segment is of temporal width Δt, the fuel cost function from Equation 4.21 can be approximated as

$$J_F \approx \boldsymbol{\xi}^T \boldsymbol{\aleph} \Delta t \tag{4.38}$$

where $\boldsymbol{\xi} \in \mathbb{R}^{h\times 1}$ is a selection matrix between the m thrusters at all time steps defined such that $\boldsymbol{\xi}(i) \in [0,\ 1]\ \forall\ i \in [1, ..., h]$.

For each discrete segment in time, an associated thrust effect integral $\mathcal{Q}[\theta_{j-}, \theta_{j+}]$ can be calculated according to Equation 4.15. In order to accommodate non-axial thrusters, this integral must be multiplied by the matrix $\mathcal{S}$ to obtain the thrust which can be generated by each thruster over the given interval. The total thrust effect is then given by $\boldsymbol{\mathcal{Q}}_{\mathcal{S}} \in \mathbb{R}^{6\times h}$ as

$$\boldsymbol{\mathcal{Q}}_{\mathcal{S}} = [\mathcal{Q}[\theta_0, \theta_1]\mathcal{S} \;\; \mathcal{Q}[\theta_1, \theta_2]\mathcal{S} \;\; ... \;\; \mathcal{Q}[\theta_{M-1}, \theta_F]\mathcal{S}] \tag{4.39}$$

Because spacecraft typically operate with all thrusters capable of equal output, it is assumed here that each thruster has the same maximum available thrust, such that $|u_{max,i}| = |u_{max}|$. The thruster vector is then normalized as $\bar{\boldsymbol{\aleph}} = \boldsymbol{\aleph}/|u_{max}|$, and the LP optimization problem can be cast as

$$\min_{\bar{\boldsymbol{\aleph}}} \boldsymbol{\xi}^T \bar{\boldsymbol{\aleph}} \tag{4.40}$$

subject to the constraints

$$\boldsymbol{\mathcal{Q}}_{\mathcal{S}}\bar{\boldsymbol{\aleph}} = \Phi(\theta_F)^{-1}\mathbf{z}(\theta_F) - \Phi(\theta_0)^{-1}\mathbf{z}(\theta_0) \tag{4.41}$$

$$\begin{bmatrix} I_{h\times h} \\ -I_{h\times h} \end{bmatrix}\bar{\boldsymbol{\aleph}} \leq \begin{bmatrix} \mathbf{1}_{h\times 1} \\ \mathbf{0}_{h\times 1} \end{bmatrix} \tag{4.42}$$

The constraint in Equation 4.41 requires the dynamics from Equation 4.18, while the constraint in Equation 4.42 enforces the bounded, piecewise constant nature of the thrusts.

The proposed LP method assumes that the control thrusts are bounded rather than *on-off* thrust, such that elements of $\bar{\boldsymbol{\aleph}}$ may take any value on $[0,\ 1]$. Formulating the problem using mixed-integer linear programming allows enforcement of the *on-off* condition, but at the expense of computation. For small thrust limits and long maneuver times, the bounded LP provides a good approximation of the solution, and a thresholding function can be used to ensure thrusts are simply 0 or 1. This is appropriate here because the LP is used to provide an initial guess for the HJB solver, which then refines the switch times to provide a near-optimal thrust profile. Numerically, a typical choice is to enforce the restriction

$$\begin{aligned} \bar{\boldsymbol{\aleph}}_i &= 1 \qquad \text{if } \boldsymbol{\aleph}_i > \epsilon \\ \bar{\boldsymbol{\aleph}}_i &= 0 \qquad \text{otherwise} \end{aligned} \tag{4.43}$$

This construction is useful for converting thrusts obtained using the LP technique into switch true anomalies which can be utilized as an initialization for the mixed LP-M/HJB technique.

To summarize, an LP solution is found by discretizing the time window into M segments, then stacking the thrust vector $\boldsymbol{\alpha}$ associated with each segment into the larger

vector $\bar{\aleph}$. The potential thrust effect for each segment is given by the matrix $\boldsymbol{Q}_{\mathcal{S}}$. The LP then solves the resultant problem with both constraints on the state equality and the available thrust inequality. The final solution vector is then thresholded to construct a feasible space of vectors in which thrusters are either on or off. This provides a near-optimal solution to the fuel optimal *on-off* thruster problem, yielding accurate solutions without requiring a high level of computation. This problem can be solved identically over one or multiple orbits, though solution precision declines as the number of orbits increases.

4.3.3 Integrated LP-*M*/HJB Algorithm Realization

Solving the HJB and LP problems can easily be accomplished by encoding the problem into a compact form for use with standard solving methods, such as those provided in MATLAB or other off-the-shelf software. As noted, the computation time and memory of the LP solver scales as the number of true anomaly points M and the number of thrusters m increases. However, a variety of tools exist which allow this problem to be solved for less memory-intensive scenarios[66]. The HJB formulation, by contrast, can be solved using standard gradient search algorithms or a more complex damped (Levenberg-Marquardt) method, but only local optimality is guaranteed. To ensure global optimality, a better initial guess is required. The goal of a mixed LP-*M*/HJB algorithm is to incorporate the advantages of both solution approaches — fast computation, readily available solution techniques, global optimality, and structured *on-off* solutions — while minimizing the disadvantages — high memory bandwidth and poor performance away from a good initial guess.

The mixed LP-*M*/HJB algorithm utilizes the LP technique to construct an initial switching true anomaly set $\boldsymbol{\Theta}_0$ which can be used in a solver in conjunction with the

state and costate constraints of the HJB problem to generate an optimal solution. The set $\boldsymbol{\Theta}_0$ gives the true anomalies at which thrusters turn on or off, according to the LP solution. This can be accomplished by re-stacking the vector $\bar{\boldsymbol{\aleph}}$ into an $m \times M + 2$ matrix:

$$\tilde{\boldsymbol{\aleph}} = \left[\mathbf{0}_{m\times 1} \;\; \bar{\boldsymbol{\aleph}}(1:m) \;\; \bar{\boldsymbol{\aleph}}(m+1:2m) \;\; \cdots \;\; \bar{\boldsymbol{\aleph}}(h-m+1:h) \;\; \mathbf{0}_{m\times 1}\right] \tag{4.44}$$

Defining a span of columns of $\tilde{\boldsymbol{\aleph}}$ from the k_1 entry to the k_2 entry as $\tilde{\boldsymbol{\aleph}}_{k_1:k_2}$, the difference across columns is

$$\Delta\tilde{\boldsymbol{\aleph}} = \tilde{\boldsymbol{\aleph}}_{2:M+2} - \tilde{\boldsymbol{\aleph}}_{1:M+1} \tag{4.45}$$

The matrix $\Delta\tilde{\boldsymbol{\aleph}} \in \gg \times \mathbb{M} + \nVdash$. The columns of this difference matrix can then be associated with the true anomalies $\{\theta_0, \cdots, \theta_M\}$, and the switching set $\boldsymbol{\Theta}_0$ is given by the elements of $\Delta\tilde{\boldsymbol{\aleph}}$ as follows. The set

$$\boldsymbol{\Theta}_0 = \{\boldsymbol{\theta}_1, \cdots, \boldsymbol{\theta}_m\} \tag{4.46}$$

where each subset $\boldsymbol{\theta}_i$ contains the $n_{p,i}$ pairs of switching true anomalies for the ith thruster. The first element of the jth such pair, $\theta_{i,j-}$, corresponds to the true anomaly associated with the jth instance of 1 in the ith row of matrix $\Delta\tilde{\boldsymbol{\aleph}}$; the second element corresponds to the jth instance of -1 in the ith row of matrix $\Delta\tilde{\boldsymbol{\aleph}}$. It is important to note that any nonzero elements in a row of $\Delta\tilde{\boldsymbol{\aleph}}$ always occur first as a 1, then as a -1.

The mixed LP-M/HJB algorithm for solving fuel optimal maneuvers with attitude constraints is presented in Figure 4.3; the algorithm is shown with the typical problem parameters, indicating the flexibility which exists in the choice of parameters to achieve a mission objective. This algorithm solves the LP problem using a computationally

reasonable discretization M to obtain an initial guess for the HJB solution, which can then be readily calculated to produce near-optimal thrust profiles very quickly.

User-defined variables which affect performance are M, the number of discrete points to solve in the LP initialization; ϵ, the value at which an LP element is considered as a possible thrust point in the HJB initialization; b, the number of iterations allowed for HJB convergence; and δt, the minimum step size allowed in the HJB solver. This step size can be assigned to a value significantly smaller than the discretization step, leading to a more precise *on-off* solution than would otherwise be available, but also potentially leading to longer convergence times. As shorthand for comparison and use, the LP with M discretization points will be referred to as LP-M; similarly, the mixed LP-M/HJB technique which uses M points in the LP initialization will be referred to as LP-M/HJB.

4.3.4 Benchmark Comparisons of HJB, LP, and Mixed LP-M/HJB

In order to elucidate the differences between HJB, LP, and mixed LP-M/HJB, as well as the benefits of the mixed LP-M/HJB algorithm, a benchmark problem is defined and simulated. Notationally, the cost associated with a particular method is referred to as $J_F(\cdot)$, where $\cdot$ is the method in question. The error in the converted relative reference frame associated with a solution is defined by

Initialize reference orbit parameters (a, e, μ)

Known: θ_0, θ_F, desired final state $\mathbf{z}(\theta_F)$

Initialize relative orbit parameterization $\mathbf{P}(\theta_0) = [p_1, ..., p_6]_0$

for each variation in final parameterization $\mathbf{P}(\theta_F) = [p_1, ..., p_6]_F$

Define spline integral over $[\theta_0, \theta_F]$ (Equation 4.15)

Solve LP:

Discretize span $[\theta_0, \theta_F]$ into M segments

Construct $\boldsymbol{Q}_{\mathcal{S}}$ and constraints (Equations 4.41 and 4.42)

Solve Equation 4.40 with constraints to find $\bar{\boldsymbol{\aleph}}$

Convert $\bar{\boldsymbol{\aleph}}$ to *on-off* thrusts using tolerance ϵ (Equation 4.43)

Construct initial switching set $\boldsymbol{\Theta}_0 = \{\theta_{1,1-}, \theta_{1,1+}, \cdots, \theta_{m,n_{p,m}-}, \theta_{m,n_{p,m}+}\}$

(Equations 4.44-4.46)

Optimize using HJB Equations 4.18 and 4.29 near $\boldsymbol{\Theta}_0$

Step to next possible final parameterization

end

Figure 4.3: Pseudo-code for the integrated LP-*M*/HJB for one spacecraft.

$$\Delta|\mathbf{z}_p(\theta_F)| = \left\| \begin{bmatrix} 1 & 0 & 0 & 0 & 0 & 0 \\ 0 & 0 & 1 & 0 & 0 & 0 \\ 0 & 0 & 0 & 0 & 1 & 0 \end{bmatrix} \mathbf{z}_{converged}(\theta_F) \right| - \left\| \begin{bmatrix} 1 & 0 & 0 & 0 & 0 & 0 \\ 0 & 0 & 1 & 0 & 0 & 0 \\ 0 & 0 & 0 & 0 & 1 & 0 \end{bmatrix} \mathbf{z}_{desired}(\theta_F) \right| \quad (4.47)$$

As noted previously, the general goal is of the new algorithm is to incorporate the scalability of the HJB algorithm with the robustness of LP. A good initial guess for converging to a solution which satisfies the HJB equations is generally difficult to obtain, but the LP can provide a good starting point for almost all cases.

Figure 4.4 shows a comparison of the computation time and performance for the LP and mixed LP-M/HJB solvers for a test case of a maneuver in which the spacecraft is rotating at a constant rate of 2 rev/orbit about a reference orbit with perigee distance a_p = 700 km with eccentricity $e = 0.4$. The spacecraft move from a 12 m radial separation to 25 m radial separation in half an orbit. Performance can be evaluated in a variety of ways. The left plot compares the computation time of the converged solutions using only linear programming with those obtained using the mixed LP-M/HJB. Each vertical line represents a different value of M (see caption); the point on the right projects the linear program discretization number M which requires the same computation time as the mixed technique to solve. The right plot shows the converged precision with respect to the LP-4000/HJB solution, with the projected point indicating the discretization M required for the LP solution to match the precision of the mixed solution. The arrows in the center show whether the extra computation time used by the mixed LP-M/HJB algorithm has resulted in a solution with improved precision over LP alone. Upward

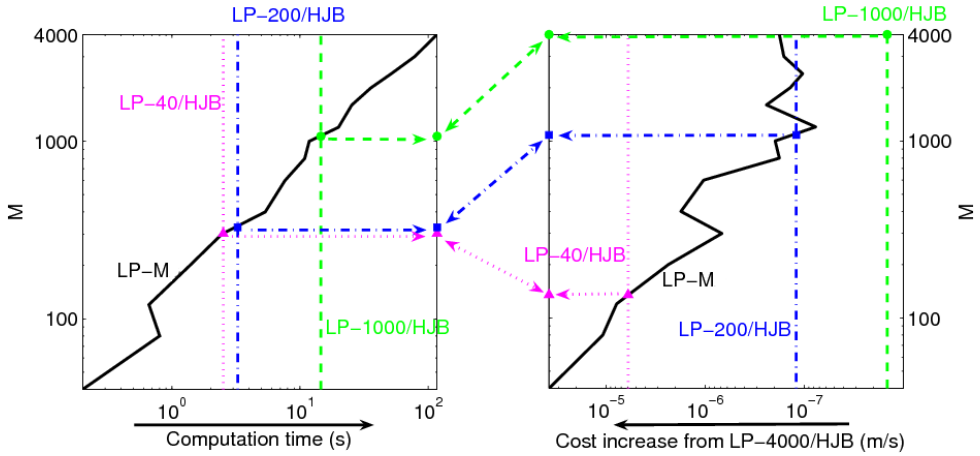

Figure 4.4: Comparison of computation time and precision for eccentricity $e = 0.4$ for the test case of 2 rev/orbit rotation rate and perigee altitude $a_p = 700$ km. (*L*eft) Computation time for increasing M for the LP as compared with computation time for LP-40/HJB (magenta), LP-200/HJB (blue), and LP-1000-HJB (green). Projected points show the discretization which could be achieved by LP alone for the computation time taken by each LP-M/HJB solution. (*R*ight Increase in converged fuel cost from LP-4000/HJB for the same example. The projected points indicate the discretization required to achieve identical precision as each LP-M/HJB solution. If the line in the middle slants upward, the computation time is shorter to obtain equivalent precision; a downward slant indicates increased computation time to obtain equivalent precision.

slanting lines indicate that the precision improves with respect to computation time, while downward slanting lines indicate the precision decreases for the same computation time. As M increases past 40, the mixed LP-M/HJB algorithm quickly obtains a solution which is more precise than LP only for the same computation time. Likewise, as M increases, the computation time for LP-M/HJB approaches that of LP-M. This illustrates the ability of the mixed LP-M/HJB algorithm to resolve solutions more quickly than LP for relatively small discretization number M.

It is notable that the improvements made by the mixed LP-M/HJB algorithm are dependent on a good initialization obtained by the LP. In Figure 4.5, the scenario is evaluated over a range of eccentricities with $a_p = 700$ km, this time with LP initializations of 40, 200, 1000, and 4000. In the upper plot, it is apparent that the LP technique has difficulty resolving exact solutions for large eccentricities, and the mixed LP-M/HJB solution outperforms LP alone in almost all cases. Similarly, as eccentricity increases, for small M, LP fails to approach a solution, which prevents the LP-M/HJB technique from obtaining an initial guess; this leads to the failures indicated in the figure. The lower plot illustrates how the final error associated with the rounded LP-M solution compares with the error from the LP-M/HJB solution: in all cases, the mixed LP-M/HJB algorithm converges to a normative pseudo-position $\lesssim 10^{-3}$, but for large e, the rounded LP solution results in a significant errors $\sim 10^{3}$. This shows that LP has difficulty converging to the *b*ang-off-bang solution structure, achieving instead steadily worsening costs which rely on partial thrusting.

4.4 Applications to CU Sat

The Cornell University NanoSat project proposes to place two spacecraft in nearby orbits for the purposes of inspection of one another such that a three-dimensional image of each spacecraft can be reconstructed on the ground[15]. This mission is a demonstration of a variety of autonomous formation technologies, including autonomous formation keeping and maneuvering. The spacecraft will reside in low-Earth orbit, limiting altitude to a maximum of 1200 km and eccentricity to $e \lesssim 0.1$. The spacecraft are spin-stabilized with a spin rate of near 1°/sec. Because of the demands of the problem, accounting for thruster rotation is important for planning. Each spacecraft is equipped with eight PPT thrusters capable of producing 60 μN and has a mass of approximately

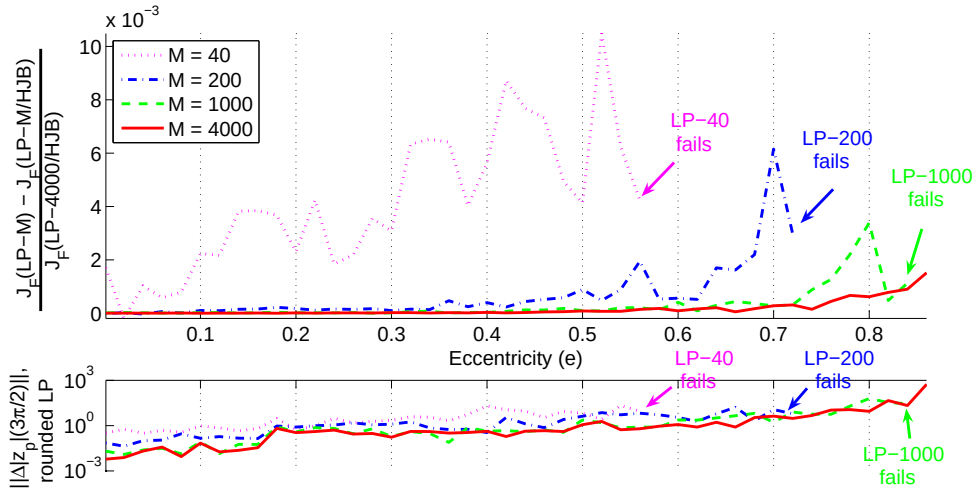

Figure 4.5: Comparison of converged solutions for LP-M/HJB and LP for $M = 40$ (magenta), $M = 200$ (blue), $M = 1000$ (green) and $M = 4000$ (red) for the test case of a 2 rev/orbit rotation, fixed perigee distance $a_p = 700$ km, and increasing eccentricity. (*T*op) Difference between LP-M converged fuel cost and LP-M/HJB converged fuel cost. For small M, the LP fails to converge to any solution when a certain eccentricity is reached; for large M and large eccentricity, the LP-M/HJB solution begins to noticeably outperform the LP with equivalent discretization. (*B*ottom) As eccentricity increases, the rounded solutions become exponentially less precise.

21 kg.

During the mission, the two spacecraft separate on-orbit and must subsequently maneuver into a stable formation before maneuvering again into a position to complete the inspection mission tasks. This section of the paper considers several problems in which one or both spacecraft complete a different maneuver; consideration is given to both single-spacecraft and formation costs, as defined in this paper. The mixed LP-M/HJB technique is applied to each of these problems in order to solve for the near-optimal thrust profiles for the sample maneuvers. Because the spacecraft are unlikely to significantly change spin rates during or after maneuvering, it is assumed that each CU Sat spacecraft maintains a spin rate of 1°/sec through the use of its attitude control system, which is designed to minimize deviations from this nominal rate.

The initial conditions used for computation for all problems in this section are given in the tables in Appendix D. All reconfigurations considered here are performed during the time period $\theta \in [0, \frac{3\pi}{2}]$, which allows for error-correction in the last quarter of the orbit and ensures that collision avoidance measures can be employed if necessary. Three simulations are presented. In the first simulation, one spacecraft (*leader*) is taken as the reference center, and the other (*follower*) stabilizes its orbit with respect to the reference, resulting in a leader-follower formation. The second example demonstrates a maneuver where the follower spacecraft moves from leader-follower into a three-dimensional relative orbit such that images can be taken. In the final simulation, a varying reference center location is considered in the formation maneuver optimization, where fuel optimal maneuvers are generated for both spacecraft, with evaluations of both single-spacecraft fuel cost and formation fuel cost. For each example, $M = 800$ is used to adequately capture the problem dynamics without significantly increasing computation time.

Figure 4.6: Artist's conception of the CU Sat mission. The mission proposes to place two spacecraft 10-20m apart in an inspection mission in which each spacecraft photographs the other from all sides. Each spacecraft rotates to ensure frequent photographic opportunities during each orbit.

4.4.1 Entering a Leader-Follower Formation

CU Sat's design indicates that separation will occur normal to the orbital plane; the dynamics of the problem suggest that the resulting orbits will be *unstable* with respect to one another — i.e. the relative path of either spacecraft with respect to the other will not repeat. Before the primary inspection portion of the mission, the CU Sat mission specifies that the spacecraft will move into a leader-follower formation from an unstable formation caused by the initial deployment. A two-stage process is proposed for this maneuver: (1) transiting the desired follower spacecraft into a stable relative orbit (*stabilization*); and (2) transiting from this stable relative orbit into a leader-follower formation (*acquisition*). This two-stage process is appropriate because the instability achieved during separation will make damping of the cross-axis motion prior to stabilization exceedingly difficult if not impossible. Initial conditions are chosen to be representative of an orbit-normal separation with a small ($\lesssim 5\%$) disturbance, and results presented in this paper are typical for such disturbances.

Table 4.1 shows the initial conditions $p_{(\cdot),0}$ for the unstable relative orbit. While only one set of initial conditions is shown, simulations over a range of appropriate initial conditions by the authors have yielded similar results. For the two-stage maneuver, there are many degrees of freedom which could be optimized as part of the stabilization portion of the problem. In this example, two parameters are allowed to remain free while the others are constrained: formation centering parameter $p_{1,st}$, which is required for any formation that does not undergo relative rotation, and planar displacement parameter $p_{3,st}$, which captures the relative displacement along the radial direction. The coupling of $p_{2,st}$ and $p_{3,st}$ is not necessary, but it simplifies the planar dynamics by damping the motion which is already present, rather than drastically altering it. The stabilized cross-axis parameters $p_{5,st}$ and $p_{6,st}$ are selected as the midpoint between the unstable initial

Table 4.1: Parameters for stabilization and acquisition

	Initial condition $(p_{(\cdot),0})$	Stabilization $(p_{(\cdot),st})$	Acquisition $(p_{(\cdot),ac})$
p_1	28.909	$p_{1,st}$	12.5
p_2	-45.252	$\frac{45.252}{3.5293} p_{3,st}$	0
p_3	-3.5293	$p_{3,st}$	0
p_4	-0.90229	0	0
p_5	501.24	$\frac{501.24}{2}$	0
p_6	-207.62	$\frac{-207.62}{2}$	0
Reference	$\mu = 3.986012 \times 10^{-5}$ km^3/s^2		
	$a = 7078.931$ km , $e = 0.04$		

condition and the desired leader-follower state, such that thrusts are preferentially selected to complete the primary objective of stabilizing the planar orbit. It is important to note that in this application neither the stabilization or acquisition stage can be completed in a single orbit because of the limited available thrust. Due to this limitation, a final free parameter considered here is given by

$$O = \frac{\theta_{F,man} - \theta_0}{2\pi} \tag{4.48}$$

where $\theta_{F,man}$ is the first true anomaly after the maneuver is complete such that

$$\theta_{F,man} \text{mod } 2\pi = \theta_0 \tag{4.49}$$

The quantity O defines the number of full orbits over which a stage takes place. For this example, maneuvering during each orbit remains constrained to $\theta \in [0, \frac{3\pi}{2}]$ such that

corrective thrusts can be performed after each orbit; however, such a constraint is not necessary.

It is clear, then, that the initial acquisition point (the start of the second stage) is identical to the final stabilization point (the end of the first stage), and each stage may be completed over a subset of the total O number of orbits:

$$O = O_{st} + O_{ac} \tag{4.50}$$

After the completion of any full orbit in which the final parameterization is unstable, the parameterization must be recalculated for true anomaly $\theta \in [0, 2\pi]$ to ensure drift is accounted for. Note that no such reparameterization is required for full orbits which result in a stable parameterization, as stable parameterizations are invariant with true anomaly. The objective in this section is to determine the optimal maneuvering strategy to successfully — and safely — complete the two-stage scenario.

For this simulation, the desired final parameterization after both stages places the spacecraft 13 m apart at true anomaly $\theta = \pi$; note that this corresponds to $p_1 \approx 12.5$. The optimization then probes the allowed intermediate stage parameters $(p_{1,st}, p_{3,st})$ which minimize the required fuel. It necessarily does not consider any value of $p_{1,st}$ or $p_{3,st}$ which may endanger the spacecraft. In particular, it is suggested here that the spacecraft should not move within 10 m of one another at any point in their respective orbits, or during maneuvering once stabilization has been achieved. By constraining the parameters $(p_{5,st}, p_{6,st})$ to be those given in Table 4.1, and further constraining the centering parameter be in the range $p_{1,0} = 28.5 \leq p_{1,st} \leq 12.5 \approx p_{1,ac}$, this prevents the interspacecraft distance from exceeding 10 m by constraining $p_{3,st} \lesssim 1.75$.

In order to understand the sensitivities associated with the stabilization (first) stage alone, a multi-stage mission optimization is defined as

$$\min_{\mathcal{O}} \min_{(p_{3,st}, p_{1,st})} J_{fuel,st} \tag{4.51}$$

Figure 4.7 compares the fuel cost computed using Equation 4.21 for the stabilization stage over the allowed optimization parameter space $(p_{3,st}, p_{1,st})$ for multi-step maneuvers requiring $\mathcal{O}_{st} \in [17, 42]$. Given a defined $\mathcal{O}_{st}$, the minimum cost occurs at the stabilization point $(p_{3,st}, p_{1,st}) = (p_{3,max}, p_{1,0})$. A global minimum fuel cost occurs for $\mathcal{O}_{st,min} = 27$. Preserving the formation center $p_{1,0}$ simply minimizes the energy required to change the orbit. Likewise, forcing an increase in $p_{3,st}$ reduces the relative planar drift across successive orbits; this allows successive maneuvers to better force $p_{4,st} \to 0$ by reducing orbit-to-orbit variations in this parameter. However, such variations depend on the maneuver being sufficiently short, such that the drift associated with the instability does not dominate the stabilization thrust. Additionally, this scenario shows that changes to along-track p_1 are more costly than variations in radial p_3, particularly when performed in conjunction with stabilization near the minimum final true anomaly.

The acquisition stage begins at the stabilization point and ends with a leader-follower formation with $p_{1,ac} = 12.5$ and $p_{i,ac} = 0$ for $i \in \{2, ..., 6\}$; this parameterization results in the desired minimum separation of 12 m between the spacecraft at true anomaly $\theta = \pi$. This problem is cast similar to the prior example as the multi-stage optimization of

$$\min_{\mathcal{O}_{ac}} \min_{(p_{1,st}, p_{3,st})} J_{fuel,ac} \tag{4.52}$$

Figure 4.8 shows the fuel cost as a function of the stabilization parameters $(p_{1,st}, p_{3,st})$ for four maneuver lengths $(\mathcal{O}_{ac} \in \{16, 18, 20, 22\})$ for the acquisition stage. The minimum in this set requires the most orbits to complete, with $\mathcal{O}_{ac}$ largely determining the stage fuel use. However, as the allowed number of orbits increases, the fuel cost of varying $p_{3,st}$ becomes a less important factor in determining the minimum fuel solution, a result

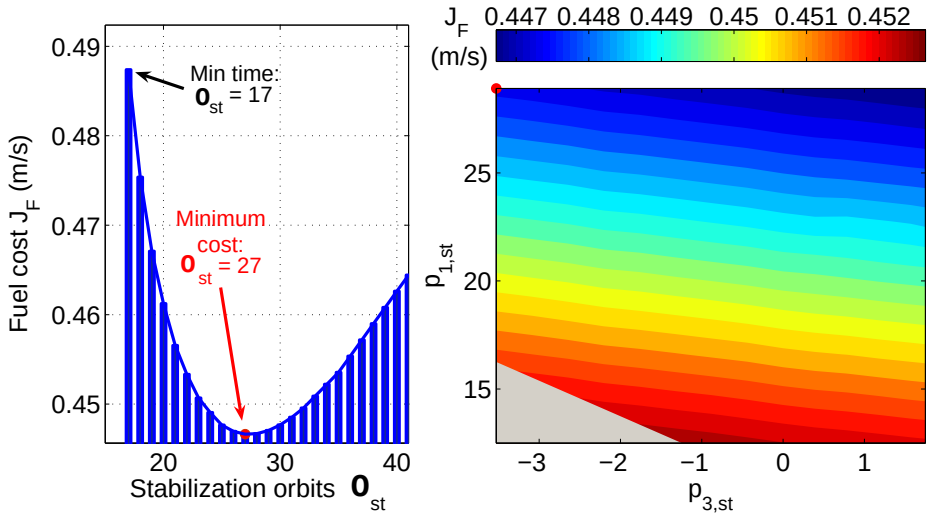

Figure 4.7: (Left) Minimum fuel cost to stabilize the relative orbit over the allowed parameters ($p_{3,st}$, $p_{1,st}$) for several maneuver lengths (O_{st}). (Right) Fuel cost to stabilize the relative orbit over the allowed parameters ($p_{3,st}$, $p_{1,st}$) for $O = 27$. The minimum is at ($p_{3,st}$, $p_{1,st}$) = ($p_{3,max}$, $p_{1,0}$) and represents the global minimum for this parameter space for any number of orbits. Changes in O have no effect on the position of the minimum or the amount of fuel cost variation across the parameter space, which is limited for safety. The purple dot marks the initial condition.

of the longer maneuver time allowing relative motion to be more slowly damped for the same amount of fuel.

The leader-follower formation problem is now considered as an optimization over both stages, stabilization and acquisition. This is defined by

$$\min_{\mathcal{O}} \min_{(p_{1,st}, p_{3,st})} J_{\text{fuel}}, \quad \mathcal{O} = \mathcal{O}_{ac} + \mathcal{O}_{st} \tag{4.53}$$

Figure 4.9 gives the minimum fuel cost over the range of allowed optimization parameters for different maneuver lengths $\mathcal{O}$, separated into the stabilization stage length ($\mathcal{O}_{st}$) and acquisition stage length ($\mathcal{O}_{ac}$). Diagonal lines and open dots indicate fixed maneuver lengths $\mathcal{O} = \mathcal{O}_{st} + \mathcal{O}_{ac}$. The minimum cost for each $\mathcal{O}$ is given by a solid dot. For small $\mathcal{O}$, the optimal strategy is to enforce as short a stabilization stage as possible, as the fuel savings achieved by slightly increasing $\mathcal{O}_{st}$ are significantly less than those achieved by corresponding increases in $\mathcal{O}_{ac}$. For longer maneuver times $\mathcal{O}$, this strategy is supplanted by one in which the stabilization stage is performed near its fuel optimal number of orbits $\mathcal{O}_{st}$ while the stabilization occupies the remaining allowed maneuver period. These results also indicate that a longer maneuver time can result in a significant fuel savings only if most of the additional orbits are devoted to acquisition. The minimum for all orbit numbers is achieved for stabilization parameterization $(p_{1,st}, p_{3,st}) = (p_{1,0}, 1.75)$. This is a by-product of the strong dependence of the stabilization fuel cost and weak dependence of the acquisition fuel cost on stabilization parameterization. In addition, while a larger $p_{3,st}$ does provide for a smaller fuel cost, the resultant formation does not provide adequate safety margins for spacecraft separation.

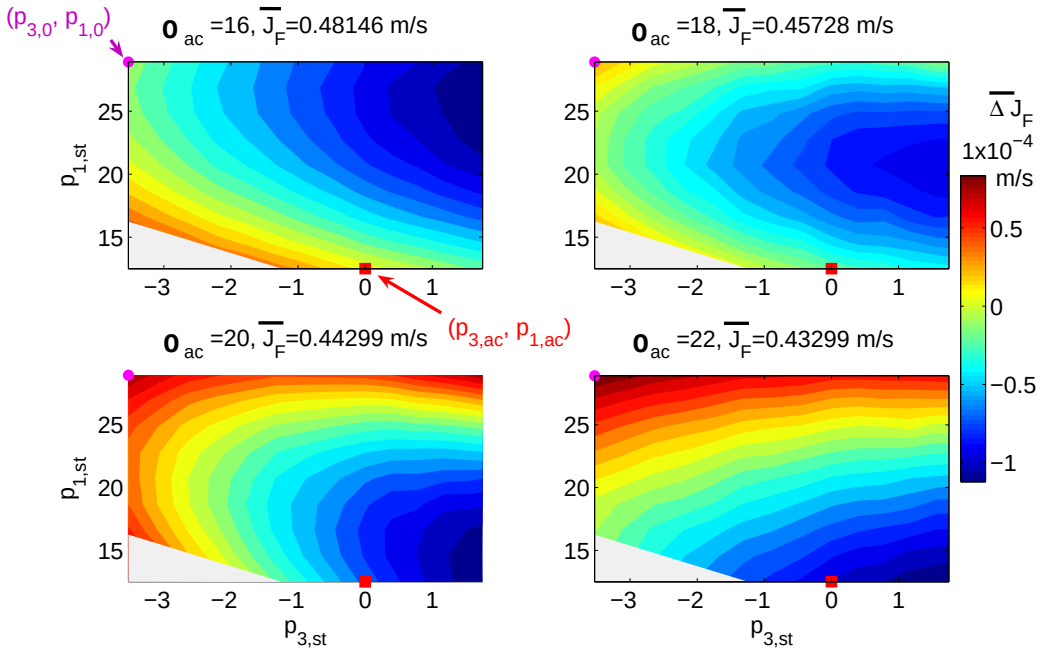

Figure 4.8: Comparative cost to perform the acquisition stage of the maneuver as a function of stabilization parameters $p_{1,st}$ and $p_{3,st}$ for increasing number of allowed orbits O_{ac}. As O_{ac} increases, the relative dependence on $p_{1,0}$ increases, but the absolute cost decreases much more significantly.

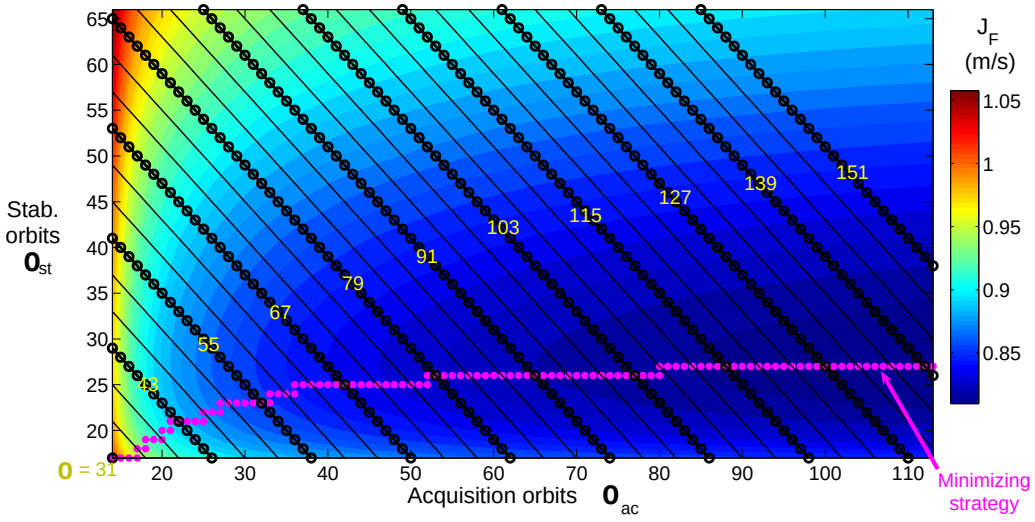

Figure 4.9: Minimum fuel cost to perform both the stabilization and acquisition stages of the maneuver to establish a leader-follower formation as it varies with orbit numbers O_{st} and O_{ac}. The diagonal lines and open dots are isotemporal, where $O = O_{st} + O_{ac}$ is constant. A closed dot indicates a minimum for a certain O.

4.4.2 Initiating Relative Motion About Each Spacecraft: Single-Spacecraft Maneuver

With the spacecraft established in a stable leader-follower formation, the mission objectives can be achieved only through additional maneuvering. In particular, it is necessary that the two spacecraft take up motions relative to each other in order to generate a useful set of photographs for inspection. Again, the scenario considered here fixes one spacecraft (leader) while allowing the other (follower) to move into a stable relative orbit centered around the leader. Because the maneuver is small, this transit can be performed in a single orbit. The optimization must constrain $p_1 = 0$ in order to create a centered orbit, as required for inspection. To simplify this formation optimization problem, two additional constraints are employed, as shown in Table 4.2: a separation of 12 m is

achieved at true anomaly $\theta_C = \pi$; and $\dot{x}_3^R(\theta_C) = 0$. The desired final position then resides on a 12-meter sphere about the leader at the critical true anomaly $\theta = \theta_C$. The choice of θ_C in this case allows the spacecraft to maneuver to the desired point as it approaches apogee, where slow orbital dynamics will allow for viewing and photographing over a range of true anomalies about $\theta = \pi$ with little variation in separation distance.

The final formation parameterization is now defined for the optimization problem. Defining the vector connecting the leader to the follower as $\Delta\mathbf{x}^R = \mathbf{x}_{FOLL}^R - \mathbf{x}_{LEAD}^R$, the constraint that the relative distance between the spacecraft lie on a sphere is given by $||\Delta\mathbf{x}^R|| = \varrho$, where ϱ is the separation distance. This condition constrains the vector $\Delta\mathbf{x}^R$ to a sphere centered about the leader spacecraft. Positions on this sphere can be defined in spherical coordinates via an azimuthal angle ϕ measured from the against-track vector for the reference leader spacecraft, $\hat{x}_1^R$, and an elevation angle ν measured from a plane parallel to the $\hat{x}_1^R - \hat{x}_2^R$ plane, in which the leader spacecraft resides, at height $x_{3,LEAD}^R$. The Cartesian coordinate analogues for the elements of $\Delta\mathbf{x}^R$ are

$$\Delta x_1^R = \varrho \cos\phi \cos\nu \tag{4.54}$$

$$\Delta x_2^R = \varrho \sin\phi \cos\nu \tag{4.55}$$

$$\Delta x_3^R = \varrho \sin\nu \tag{4.56}$$

The optimization problem addressed by this example is then given as

$$\min_{(\phi,\nu)} J_{\text{fuel}} \tag{4.57}$$

Figure 4.10 shows the cost to maneuver to the set of possible final angles ϕ_{sph} and ν_{sph} from a 13 m leader-follower formation at critical true anomaly $\theta_C = \pi$ to a relative orbit in which the leader spacecraft resides at the origin and the follower spacecraft has

Table 4.2: Parameters for stabilization and acquisition

	Leader-follower ($p_{(\cdot),lf}$)	Relative motion ($p_{(\cdot),sph}$)
p_1	12.5	0
p_4	0	0
θ_C	π	π
$\dot{x}_3^R$	0	0
ϕ	0	ϕ_{sph}
ν	0	ν_{sph}
Reference	$\mu = 3.986012 \times 10^{-5}$ km^3/s^2	
	$a = 7078.931$ km , $e = 0.04$	

$\varrho = 12$ m at $\theta_C = \pi$. The three-dimensional surface this creates is also shown.

As shown, this optimization problem results in cost contours with multiple local minima. The global minimum occurs for a final parameterization in which the spacecraft is at $\nu_{sph} \approx 8^\circ$ and $\phi_{sph} \approx 0^\circ$ at $\theta = \theta_C$. At this location, the cross-axis variation is small while the change in parameter p_3 is minimized. Because inclination changes are generally costly, the low cost associated with limiting such cross-axis motion is reasonable. The slight elevation associated with this minimum is due to the thruster placements and body rotation; for a non-rotating spacecraft with axial thrusters, the fuel cost would be symmetric about $\nu = 0$. The maximum is for the spacecraft to transition to $\phi_{sph} \approx 135^\circ$ — approximately azimuthally normal to the minimum — with a small cross-axis displacement. In this region, the fuel required to increase p_3 to meet the problem constraints is more significant than the general cost increase associated with

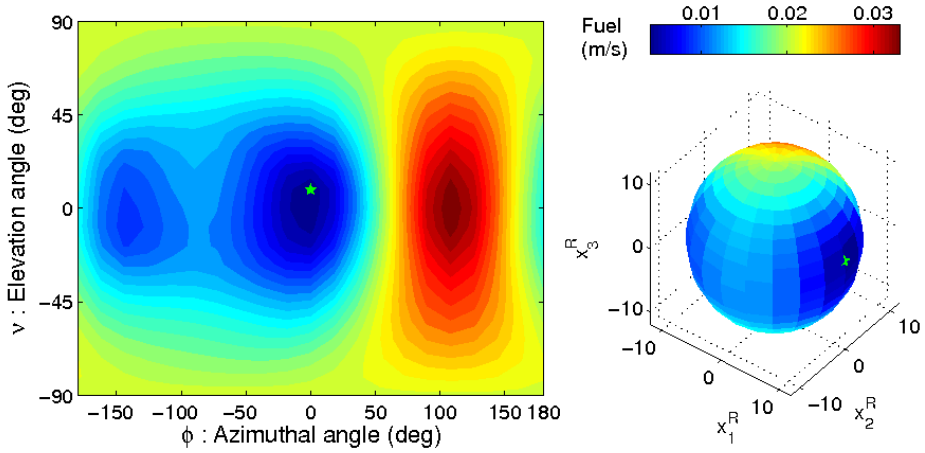

Figure 4.10: Fuel cost for moving from a leader-follower formation to a relative orbit which passes through a sphere at distance $\varrho = 12$ m about the reference center at $\theta_C = \pi$. The plot is projected onto a flat surface in spherical coordinates, with the minimum point as indicated by the green star.

a variation in cross-axis parameters. This example demonstrates the importance for spacecraft designers to consider the possible effects of thruster placements, in addition to other factors, during each phase of the mission, and it illustrates how the theory developed in this paper can be used in conjunction with the spacecraft design process to motivate both thruster placements and formation selection.

4.4.3 Initiating Two-Spacecraft Relative Motion

Because both spacecraft in the CU Sat formation are identical, allowing one spacecraft to perform all maneuvers does not make efficient use of the available resources. In order to reduce the burden on each spacecraft, maneuvers should be considered in context of mission objectives and mission lifetime, which typically require fuel expenditure from both spacecraft. This example considers the maneuver in which the spacecraft move

from leader-follower to a relative motion about one another, similar to the example in Section IV.B, with alternative formation centers.

The selection of a global formation center can have significant effects on the use of resources in a cluster of spacecraft, including fuel, computational effort, and communication bandwidth. The CU Sat mission will utilize carrier phase differential GPS to determine relative position and velocity to sub-millimeter accuracy; thus, with the absolute orbital data from either spacecraft with respect to the Earth, the formation center can be defined anywhere along a line connecting the spacecraft. For large formations, a complex scheme must often be used to determine the formation center[67]. However, the CU Sat pair can take advantage of the CDGPS capabilities and assign the formation center between the two spacecraft at a fractional distance, greatly simplifying the formation center selection problem.

Similar to the single-spacecraft maneuver in the previous subsection, constraints of a 12-meter separation at $\theta_C = \pi$ and $\dot{x}_3^R(\theta_C) = 0$ are imposed. An additional third constraint is added to this problem which enforces that each spacecraft resides at the endpoint of a 12-meter line passing through the reference center at true anomaly $\theta = \theta_C$. This center is defined by the fraction ν and positions in the inertial frame as

$$\mathbf{R} = \nu\mathbf{R}_{FOLL} + (1-\nu)\mathbf{R}_{LEAD} \tag{4.58}$$

This section examines the effect of varying ν on the cost to the spacecraft individually as well as the cost to the formation as a whole.

The full optimization problem for the mission is given as

$$\min_{\nu} \min_{(\phi,\nu)} J_{fuel,lead}(\nu,\phi,\nu) + J_{fuel,foll}(\nu,\phi,\nu) \tag{4.59}$$

The multi-stage optimization can then be extended to optimizing over ν, the formation

center location. In general, increasing ν has little effect on the location of the fuel-optimal final relative locations of the spacecraft at true anomaly $\theta = \pi$. The optimal strategy always places the follower spacecraft near azimuthal angle $\phi \approx 0^\circ$ and elevation angle $\nu \approx 8^\circ$. Slight variations appear in these values as ν varies due to the differences in rotations between the two spacecraft.

While the angles describing the fuel optimal parameterizations of the two spacecraft with respect to one another do not vary significantly with ν, the value of that minimum does change, as shown in red in Figure 4.11. The formation fuel use for this maneuver — defined as the sum of the fuel used by the two spacecraft in completing the maneuver — achieves a minimum when the spacecraft partition the work equally between one another, which leads to a fuel savings of approximately 8 percent for the formation. It is notable, however, that the cost borne by the leader spacecraft varies almost linearly with ν; in situations where absolute fuel use or fraction of total fuel use by only one member of the formation pair is the primary consideration, the optimal maneuvering strategy for both formation members can be quickly established. Similar fuel-saving results occur in the formation keeping problem if both spacecraft are tasked to transit during the maneuvers. The method and results presented here will allow such flexibility to be used on CU Sat-like missions to maximize resource potential in achieving objectives.

4.5 Conclusions

A novel algorithm for solving general minimum fuel problems for spacecraft with attitude dynamics in a relative reference frame using linear programming in conjunction with Hamilton-Jacobi-Bellman optimality conditions has been presented. The method scales better computationally than LP while providing the solution guarantees of a numerical HJB solution. The mixed LP-M/HJB algorithm can be used to solve a variety of

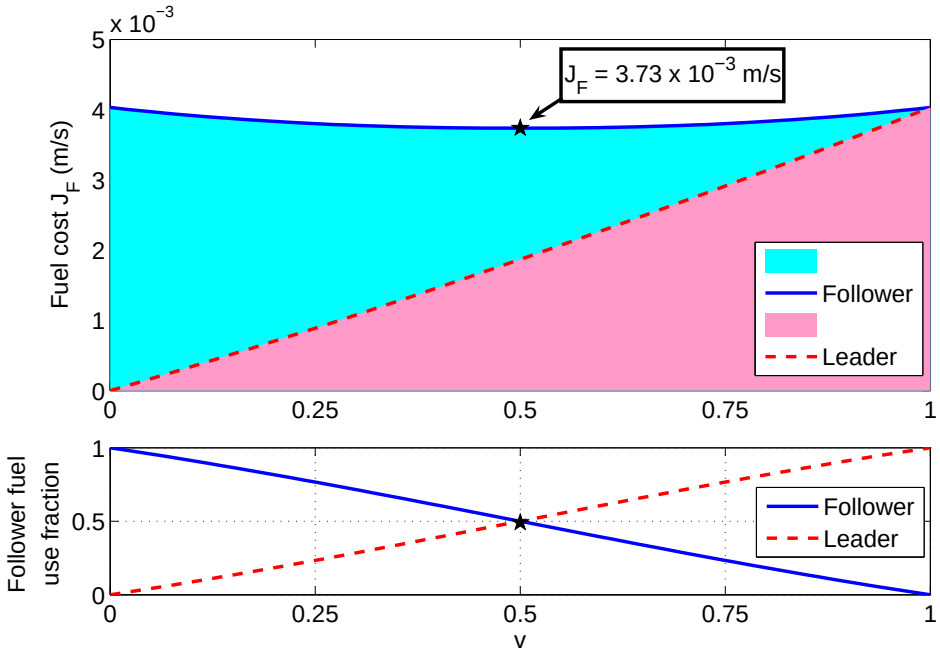

Figure 4.11: (*Top*) Total minimum formation fuel cost compared to individual fuel use as v varies: leader contribution in red, follower contribution in blue. The global minimum of $v = 1/2$ using the given simulation parameters is marked with a black star. (*Bottom*) Fraction of total fuel used by leader spacecraft in achieving the minimum formation fuel cost (minimum point marked for reference).

complex problems in which HJB constraints are known but no initial guess is available. Because the method does not rely on discretization of the dynamics, it efficiently uses memory and processer time and scales well with important system parameters, such as eccentricity and number of orbits.

The mixed LP-*M*/HJB method is applied here to the particular problem of a spacecraft formation which operates in a realistic space environment with known attitude dynamics. These dynamics were then used in conjunction with the combined LP-*M*/HJB algorithm to solve several examples involving the Cornell University NanoSat project.

Optimal formation maneuvers have been generated for modes which take the spacecraft from initial separation to stable relative orbits and data-taking. As well, different formation centers were considered, including the cost to both the formation and the individual spacecraft. Such information will be useful to CU Sat operators and those designing missions with similar goals, both as a tool for pre-launch analysis of strategies in the context of mission objectives and mission life, as well as on-orbit decision-making for achieving specific mission objectives.

Chapter 5: Conclusions and Closing Remarks

Hamilton-Jacobi-Bellman optimization can be employed to solve for optimal trajectories for spacecraft formation maneuvers in a variety of environments. This paper has explored several of these applications to show applications for these optimal or near-optimal solutions to the spacecraft formation minimum fuel problem. The primary focus has been on those methods of constraining the formation maneuver problem for realistic mission needs, including both the two-element CU Sat mission as well as the MMS tetrahedron. These tools can aid in the design and development of those and other, similar missions involving multiple spacecraft operating in close proximity.

The development of these solutions relies primarily on the closed-form solution to the relative orbit dynamics equation derived by Carter and Humi[11, 12, 13]. These closed-form, time-varying solutions allow input thrusts to be integrated to derive a net thrust effect across arbitrary true anomalies. This fundamental technique was applied to the MMS problem in Chapter 1. Chapter 2 fully solved this thrust input integral and extended the problem to examine the complex parameter space associated with a formation tetrahedron. Solutions over this parametric set were found for the general problem of a mixed-metric cost function which included data-taking capabilities and transition fuel cost. Collision avoidance constraints were also considered in the problem to guarantee all solutions would present realistic mission scenarios. In Chapter 3, the minimum fuel problem was extended to thrust along arbitrary axes, with application to rotating spacecraft. The example mission is similar to that of CU Sat, in which one spacecraft operates in close proximity to another while maintaining a constant rotation. This problem presents difficulties which are not inherent in the simplified two-axis thrust cases, but utilizing tools already established for generating approximations to the critical integrals, it is possible to determine fuel optimal solutions.

These results represent important steps toward the successful deployment of future spacecraft formation missions. However, much work remains before many such proposed missions are fully realized. Along with communication and fault-detection concerns, this dissertation addresses just a few of the formation keeping concerns. In particular, precise relative attitude maintenance will be necessary to accomplish many of the proposed tasks. And while the formation fuel optimization methods presented in this paper are flexible enough to be used to enhance the success of a variety of missions, they are specifically applicable to Keplerian orbits; other techniques must be employed for the three-body orbits suggested for programs such as MAXIM[4] and LISA[68]. In this respect, the field of spacecraft formation flying remains in its adolescence. The European Space Agency's recent investments in several proof-of-concept missions[69], however, indicates that the body of work will continue to expand, both theoretically and practically.

Appendix A: State Dynamics Fundamental Matrix Solution

A complete presentation of the development of the fundamental matrix solution to the relative orbital dynamics problem outlined in Section 2 is done by Humi[30]. The solution without singularities is given by Carter[13]. This fundamental matrix solution $\Phi(\theta)$ is

$$\Phi(\theta) = \begin{bmatrix} 2S(\phi_1) & 2S(\phi_2) & S(2\phi_3+1) & 1 & 0 & 0 \\ 2\phi_1 & 2\phi_2 & 2\phi_3+1 & 0 & 0 & 0 \\ \phi_1 & \phi_2 & \phi_3 & 0 & 0 & 0 \\ \phi_1' & \phi_2' & \phi_3' & 0 & 0 & 0 \\ 0 & 0 & 0 & 0 & \cos\theta & \sin\theta \\ 0 & 0 & 0 & 0 & -\sin\theta & \cos\theta \end{bmatrix} \tag{A.1}$$

where

$$
\begin{aligned}
\rho(\theta) &= 1 + e\cos\theta \\
\cos E &= \frac{\cos\theta + e}{1 + e\cos\theta} \\
\sin E &= \frac{\sqrt{1-e^2}\sin\theta}{1 + e\cos\theta} \\
\cos\theta &= \frac{\cos E - e}{1 - e\cos E} \\
K(\theta) &= (1-e^2)^{-\frac{5}{2}}\left[\frac{1}{2}E - \frac{1}{2}\sin E\cos E - \frac{e}{3}\sin^3 E\right] \\
\phi_1(\theta) &= \rho(\theta)\sin\theta \\
\phi_1'(\theta) &= \cos\theta + e(\cos^2\theta - \sin^2\theta) \\
S[\phi_1(\theta)] &= -\cos\theta\left[1 + \frac{e}{2}\cos\theta\right] \\
\phi_2(\theta) &= -6e^2\phi_1(\theta)K(\theta) + \frac{2e\sin^2\theta}{\rho(\theta)^2} - \frac{\cos\theta}{\rho(\theta)} \\
\phi_2'(\theta) &= -6e^2\phi_1'(\theta)K(\theta) + \frac{2e\sin\theta}{\rho(\theta)^3}(2\cos\theta - 3e\sin^2\theta + 2e) + \frac{\sin\theta}{\rho(\theta)^2} \\
S[\phi_2(\theta)] &= 3e\rho(\theta)^2K(\theta) - \frac{\sin\theta}{\rho(\theta)} \\
\phi_3(\theta) &= 6e\phi_1(\theta)K(\theta) - \frac{2\sin^2\theta}{\rho(\theta)^2} - \frac{\cos^2\theta}{\rho(\theta)} - cos^2\theta \\
\phi_3'(\theta) &= 6e\phi_1'(\theta)K(\theta) + \frac{6e\sin^3\theta}{\rho(\theta)^3} - \frac{4\sin\theta(e+\cos\theta)}{\rho(\theta)^3} \\
&\quad + \sin\theta\cos\theta\frac{(2+e\cos\theta)}{\rho(\theta)^2} + 2\sin\theta\cos\theta \\
S[2\phi_3(\theta)+1] &= -6\rho(\theta)^2K(\theta) - \frac{2\sin\theta\cos\theta}{\rho(\theta)} - \sin\theta\cos\theta
\end{aligned}
$$

and $S(\cdot)$ is defined as

$$S(\cdot) = S[\cdot(\theta)] = \int_{\theta_0}^{\theta} \cdot(\tau)d\tau$$

The inverse of this matrix is

$$\Phi^{-1}(\theta) = \begin{bmatrix} 0 & -2S(\phi_2) & 4S(\phi_2) + \phi_2' & -\phi_2 & 0 & 0 \\ 0 & 2S(\phi_1) & -4S(\phi_1) - \phi_1' & \phi_1 & 0 & 0 \\ 0 & 1 & -2 & 0 & 0 & 0 \\ 1 & -S(2\phi_3 + 1) & 2S(2\phi_3 + 1) + \phi_3' & -\phi_3 & 0 & 0 \\ 0 & 0 & 0 & 0 & \cos\theta & -\sin\theta \\ 0 & 0 & 0 & 0 & \sin\theta & \cos\theta \end{bmatrix} \quad \text{(A.2)}$$

Appendix B: Costate Matrix Solution

The fundamental matrix solution to the costate problem can be found by the identity

$$\Psi(\theta) = \Phi^{-T}(\theta) \begin{bmatrix} 0 & -1 & 0 & 0 & 0 & 0 \\ 1 & 0 & 0 & 0 & 0 & 0 \\ 0 & 0 & 0 & 1 & 0 & 0 \\ 0 & 0 & -1 & 0 & 0 & 0 \\ 0 & 0 & 0 & 0 & 0 & -1 \\ 0 & 0 & 0 & 0 & 1 & 0 \end{bmatrix} \tag{B.1}$$

with $\Phi^{-1}(\theta)$ as defined in Appendix A. The matrix $\Psi^{-1}(\theta)$ is then

$$\Psi^{-1}(\theta) = \begin{bmatrix} 0 & 1 & 0 & 0 & 0 & 0 \\ -1 & 0 & 0 & 0 & 0 & 0 \\ 0 & 0 & 0 & -1 & 0 & 0 \\ 0 & 0 & 1 & 0 & 0 & 0 \\ 0 & 0 & 0 & 0 & 0 & 1 \\ 0 & 0 & 0 & 0 & -1 & 0 \end{bmatrix} \Phi^{T}(\theta) \tag{B.2}$$

where $\Phi(\theta)$ is also given in Appendix A.

Appendix C: Thrust Effect Vector for Fixed-Thrust Input

The vector $\mathbf{Q}[\theta_0, \theta_F]$ gives the effect of a constant thrust input over the true anomaly segment $\theta_0 \leq \theta \leq \theta_F$. This can be calculated as the difference between the effects at the endpoints of the integral: $\mathbf{Q}[\theta_0, \theta_F] = \mathbf{Q}(\theta = \theta_F) - \mathbf{Q}(\theta = \theta_0)$. The complete integral at true anomaly θ is given in closed form componentwise for $\mathbf{Q}(\theta) = [Q_1(\theta), \ldots, Q_6(\theta)]^T + const$:

$$
\begin{aligned}
Q_1(\theta) &= C^3\left(-2u_1\left[3eN(\theta) - Y_1(\theta)\right] - u_2\left[-6e^2N(\theta) + 2eY_2(\theta) - Y_3(\theta)\right]\right) \\
Q_2(\theta) &= \frac{-2u_1C^3}{(1-e^2)^{\frac{5}{2}}}\left[\left(\frac{e^3}{2} - e\right)E + \sin E - \frac{e}{4}\left(E + \sin E\cos E\right)\right] - \frac{u_2C^3}{(1-e^2)}\cos E \\
Q_3(\theta) &= \frac{u_1C^3}{(1-e^2)^{\frac{5}{2}}}\left[E - 2e\sin E + \frac{e^2}{2}(E + \sin E\cos E)\right] \\
Q_4(\theta) &= C^3\left(-u_1\left[-6M(\theta) - 2Y_4(\theta) - Y_5(\theta)\right] - \right. \\
&\qquad \left. u_2\left[6eN(\theta) - 2Y_2(\theta) - Y_6(\theta) - Y_7(\theta)\right]\right) \\
Q_5(\theta) &= \frac{-u_3C^3}{(1-e^2)^2}\left(\frac{e}{2}\cos^2 E - \cos E\right) \\
Q_6(\theta) &= u_3C^3\left(\frac{\sin\theta}{\rho(\theta)^3} - 3eK(\theta)\right)
\end{aligned}
$$

where

$$
\begin{aligned}
\rho(\theta) &= 1 + e\cos\theta \\
\cos E &= \frac{\cos\theta + e}{1 + e\cos\theta} \\
\sin E &= \frac{\sqrt{1-e^2}\sin\theta}{1 + e\cos\theta} \\
\cos\theta &= \frac{\cos E - e}{1 - e\cos E}
\end{aligned}
$$

$$
\begin{aligned}
K(\theta) &= (1-e^2)^{-\frac{5}{2}}\left[\frac{1}{2}E - \frac{1}{2}\sin E\cos E - \frac{e}{3}\sin^3 E\right] \\
S[\cdot] &= \int \cdot \, d\,\theta \\
Y_1(\theta) &= S\left[\frac{\sin\theta}{\rho(\theta)^4}\right] = -(1-e^2)^{-3}\left(\cos E - e\sin^2 E - \frac{e^2}{3}\cos^3 E\right) \\
Y_2(\theta) &= S\left[\frac{\sin^2\theta}{\rho(\theta)^5}\right] = (1-e^2)^{-\frac{7}{2}}\left[\frac{E}{2} - \frac{\sin 2E}{4} - \frac{2e}{3}\sin^3 E + e^2\left(\frac{e}{8} - \frac{\sin 4E}{32}\right)\right] \\
Y_3(\theta) &= S\left[\frac{\cos\theta}{\rho(\theta)^4}\right] = (1-e^2)^{-\frac{7}{2}}\left[-eE + \left(1+2e^2\right)\sin E - \right. \\
&\qquad \left. \left(2e+e^3\right)\left(\frac{E}{2} + \frac{\sin 2E}{4}\right) + e^2\left(\sin E - \frac{\sin^3 E}{3}\right)\right] \\
Y_4(\theta) &= S\left[\frac{\sin\theta\cos\theta}{\rho(\theta)^4}\right] = (1-e^2)^{-3}\left[\frac{1}{2}\left(1+e^2\right)\sin^2 E + \left(1+\frac{1}{3}\cos^2 E\right)e\cos E\right] \\
Y_5(\theta) &= S\left[\frac{\sin\theta\cos\theta}{\rho(\theta)^3}\right] = (1-e^2)^{-2}\left(\frac{1}{2}\sin^2 E + e\cos E\right) \\
Y_6(\theta) &= S\left[\frac{\cos^2\theta}{\rho(\theta)^4}\right] = (1-e^2)^{-\frac{7}{2}}\left[\left(1+2e^2\right)\left(\frac{E}{2} + \frac{\sin 2E}{4}\right) + \right. \\
&\qquad \left. e\left(-3\sin E + \frac{\sin^3 E}{3}\right) + e^2\left(E - e\sin E\right)\right] \\
Y_7(\theta) &= S\left[\frac{\cos^2(\theta)}{\rho(\theta)^3}\right] = (1-e^2)^{-\frac{5}{2}}\left(e^2E - 2e\sin E + \frac{E}{2} + \frac{\sin 2E}{4}\right) \\
M(\theta) &= S\left[\frac{K(\theta)}{\rho(\theta)}\right] = (1-e^2)^{-3}\left(\frac{1}{4}E^2 - \frac{1}{4}\sin^2 E + \frac{e}{3}\cos E - \frac{e}{9}\cos^3 E\right) \\
N(\theta) &= S\left[\frac{\sin\theta K(\theta)}{\rho(\theta)^2}\right] = (1-e^2)^{-\frac{7}{2}}\left[\frac{1}{2}\left(\sin E - E\cos E\right) - \frac{1}{6}\sin^3 E - \right. \\
&\qquad \left. \frac{e}{3}\left(\frac{3E}{8} - \frac{\sin 2E}{4} + \frac{\sin 4E}{32}\right)\right]
\end{aligned}
$$

Appendix D: CU Sat Simulation Data

Initial conditions for the CU Sat spacecraft for the example simulations are provided in Table D.1 as a reference. Separation conditions are the values used at the instant of separation for an impulsive change in velocity; the positions of the spacecraft are identical. Thruster positions for the two spacecraft are as shown in Table D.2. Rotation occurs in the quaternion sense about a different vector for each spacecraft. For quaternion $\mathbf{q} = [\mathbf{a}sin(\zeta/2),\ cos(\zeta/2)]^T$, where ζ is the angle of rotation about the vector $\mathbf{a}$,

$$\mathbf{a}_{s/c,1} = \begin{pmatrix} 0.2575 \\ 0.0536 \\ 0.9648 \end{pmatrix}, \quad \mathbf{a}_{s/c,2} = \begin{pmatrix} 0.0990 \\ 0.0990 \\ 0.9901 \end{pmatrix} \tag{D.1}$$

Table D.1: Separation conditions for CU Sat example

	Global $(x_1^N, \dot{x}_1^N, x_2^N, \dot{x}_2^N, x_3^N, \dot{x}_3^N)^T$		Orbital elements $(a, e, i, \omega, \Omega, \theta)^T$
Spacecraft 1 (leader)	$3.46869135464401 \times 10^3$	km	7078.93100 km
	-6.52398592580395	km/s	0.04000000
	$4.75600512902940 \times 10^3$	km	42.3000000°
	2.37242325309425	km/s	14.0000000°
	$3.43551261223094 \times 10^3$	km	26.0000000°
	3.53075327556610	km/s	22.5000000°
Spacecraft 2(follower)	$3.46869135464401 \times 10^3$	km	7078.93342 km
	-6.52388735457831	km/s	0.04000051
	$4.75600512902940 \times 10^3$	km	42.3029145°
	2.37203625321527	km/s	14.0048943°
	$3.43551261223094 \times 10^3$	km	25.9957822°
	3.53119812624019	km/s	22.5005979°

Table D.2: Thruster data: Thrust-to-mass $u = 60/21 \times 10^{-6}$ m/s^2

	8 Thrusters							
	4 Thrusters							
$\mathbf{x}^B$	-0.6124	0.6124	-0.6124	0.6124	-0.6124	0.6124	-0.6124	0.6124
	0.3536	-0.3536	0.3536	-0.3536	-0.3536	0.3536	-0.3536	0.3536
	-0.7071	0.7071	0.7071	-0.7071	-0.7071	0.7071	0.7071	-0.7071

BIBLIOGRAPHY

[1] "The Magnetospheric Multiscale Mission...Resolving Fundamental Processes in Space Plasmas", proposal to NASA, 1999; URL: http://stp.gsfc.nasa.gov/documents/mms/mms_ stdt_ report.pdf [cited 21 Feb 2009].

[2] Beichman, C. A., Woolf, N. J., Lindensmith, C. A., "The Terrestrial Planet Finder (TPF) : a NASA Origins Program to search for habitable planets", Proposal to NASA; JPL Publication 99-3, 1999.

[3] Tsien, W., et al., "Advancing Military-Relevant Space Technologies", Space 2003 Conference, AIAA 2003-6363, Long Beach, CA, 2003.

[4] W. Cash, "MAXIM Preliminary Design", proposal to NASA, 2000; URL: http://maxim.gsfc.nasa.gov/docs/mission/niacdesign.pdf [cited 21 Feb 2009].

[5] Kumar, R., and Seywald, H., "Fuel-optimal stationkeeping via differential inclusions", *Journal of Guidance, Control, and Dynamics*, Vol 18, No. 5, 1995, pp. 1156-1162.

[6] Hablani, H.B., Tapper, M.L., and Dana-Bashian, D.J., "Guidance and Relative Navigation for Autonomous Rendezvous in a Circular Orbit", *AIAA Journal of Guidance, Control, and Dynamics*, Vol 25, No. 3, May-June 2002.

[7] Robertson, A., Inalhan, G., and How, J.P., "Spacecraft Formation Flying Control Design for the Orion Mission", *Proceedings of the 1999 AIAA Guidance, Navigation, and Control Conference*, AIAA Paper 99-4266, Portland, OR, Aug 1999.

[8] Milam, M.B, Petit, N., and Murray, R.M., "Constrained Trajectory Generation for Microsatellite Formation Flying", *Proceedings of the 2001 AIAA Guidance, Navigation, and Control Conference*, AIAA Paper 2001-4030, Montreal, Quebec, 2001.

[9] Campbell, M.E., "Collision Monitoring and Avoidance in Satellite Clusters", *IEEE Transactions of Control System Technology*, Vol 13 , Issue 1, 2005, pp. 42-55.

[10] Gim, D., and Alfriend, K.T., "State Transition Matrix of Relative Motion for the Perturbed Non-Circular Reference Orbit", *AAS/AIAA Space Flight Mechanics Conference*, AAS Paper 01-222, Santa Barbara, CA, Feb 2001.

[11] Carter, T.E., and Humi, M., "Fuel-Optimal Rendezvous Near a Point in General Keplerian Orbit", *J. Guidance*, Vol 10, No 6, Nov-Dec 1987.

[12] Carter, T.E., "New Form for the Optimal Rendezvous Equations Near a Keplerian Orbit", *Journal of Guidance, Control, and Dynamics*, Vol 13, No 1, Jan-Feb 1990.

[13] Carter, T.E., "State Transition Matrices for Terminal Rendezvous Studies: Brief Survey and New Example", *Journal of Guidance, Control, and Dynamics*, Vol 21, No 1, 1998, pp. 148-155.

[14] Inalhan, G., Tillerson, M., and How, J.P., "Relative Dynamics and Control of Spacecraft Formations in Eccentric Orbits", *Journal of Guidance, Control, and Dynamics*, Vol 25, No 1, 2002, pp. 48-59.

[15] *CUSat: An End-to-End In-Orbit Inspection System University Nanosatellite Program*, Annual Performance Report, Report No. A764574, 2007.

[16] Zanon, D.J., and Campbell, M.E., "Optimal Planner for Spacecraft Formations in Elliptical Orbits", *Journal of Guidance, Control, and Dynamics*, Vol. 29, No. 1, Jan-Feb 2006.

[17] Goddard Space Flight Center Magnetospheric Constellation; URL: http://stp.gsfc.nasa.gov/missions/mc/mc.htm [cited 16 Mar 2005].

[18] Campbell, M.E., "Planning Algorithm for Multiple Satellite Clusters", *Journal of Guidance, Control and Dynamics*, Vol 26, No 5, 2003, pp. 770-780.

[19] Campbell, M.E., Knagenhjelm, V., and Yingling, J., "Flight Software Development for the ION-F Formation Flying Mission", *2001 IEEE Aerospace Conference Proceedings*, Vol 2, pp. 553-562, Big Sky, MT, Mar 2001.

[20] Scharf, D., Hadeagh, F., and Kang, B, "A Survey of Spacecraft Formation Flying Guidance", *International Symposium on Formation Flying*, Toulouse Space Center, October 2002.

[21] Sabol, C., Burns, R., and McLaughlin, C.A., "Satellite Formation Flying Design and Evolution", *AAS/AIAA Space Flight Mechanics Conference*, AAS 99-121, Breckenridge, CO, 1999.

[22] Tillerson, M., and How, J.P., "Advanced Guidance Algorithms for Spacecraft Formation Flying"; *Proceedings of the American Control Conference*, ISSN: 0743-1619, 2002, Vol 4, pp. 2830-2835.

[23] Tillerson, M, Inalhan, G., and How, J.P., "Coordination and Control of Distributed Spacecraft Systems Using Convex Optimization Techniques", *International Journal of Robust and Nonlinear Control*, Vol 12, 2002, pp. 207-242.

[24] Carter, T.E., and Alvarez, S.A., "Quadratic-Based Computation of Four-Impulse Optimal Rendezvous near Circular Orbit", *Journal of Guidance, Control, and Dynamics*, Vol 23, No 1, 2000, pp. 109-117.

[25] Rayburn, C., et al, "Pulsed Plasma Thruster for Microsatellites", *AIAA Journal of Spacecraft and Rockets*, Vol 42, No 1, pp. 161-170, Jan-Feb 2005.

[26] Spores, R.A., et al, "Overview of the USAF Electric Propulsion Program", *37th Joint Propulsion Conference and Exhibit*, AIAA Paper 2001-3225, Salt Lake City, UT, July 2001.

[27] Ross, "How to Find Minimum Fuel Controllers", presented to the 2004 AIAA Guidance, Navigation, and Control Conference, AIAA Paper 2004-5346, Providence, R.I., Aug 2004.

[28] Alfriend, K.T., and Schaub, H., "Dynamics and Control of Spacecraft Formations: Challenges and Some Solutions", *Advances in the Astronautical Sciences*, AAS Paper 00-259, Vol 106, The Richard H. Battin Astrodynamics Symposium 2000.

[29] Tschauner, J., and Hempel, P., "Rendezvous zu einem in elliptischer Bahn umlaufenden Ziel", *Astronautica Acta*, Vol 11, No 5, 1965, pp. 104-109.

[30] Humi, M., "Fuel-Optimal Rendezvous in a General Central Force Field", *Journal of Guidance, Control, and Dynamics*, Vol 16, No 1, 1993, pp. 215-216.

[31] de Boor, C., *A Practical Guide to Splines*, Springer-Verlag, New York, 1978.

[32] Farin, G., *NURBS: from Projective Geometry to Practical Use*, A K Peters, Natick, MA, 1999.

[33] Zanon, D.J., and Campbell, M.E., "Optimal Planning for Tetrahedral Formations Near Elliptical Orbits"; AIAA Guidance, Navigation, and Control Conference, AIAA-2004-5127, 2004.

[34] "Solving Magnetospheric Acceleration, Reconnection, and Turbulence (SMART): Concept Study Report for the Magnetospheric Multiscale Mission", NASA AO 03-OSS-01, March 2004.

[35] Saylor, W.M., et al, "New Scientific Capabilities Enabed by Autonomous Constellations of Smallsats", *AIAA 21st Annual Conference on Small Satellites*, 2007.

[36] Wertz, J.R., and Bell, R., "Autonomous Rendezvous and Docking Technologies — Status and Prospects", *SPIE Space Systems Technology and Operations Conference AeroSense Symposium*, SPIE Paper No 5088-3, 2003.

[37] Clemente, D.C., and Atkins, E.M., "Optimization of a Tetrahedral Satellite Formation", *AIAA Guidance, Navigation, and Control Conference, Journal of Spacecraft and Rockets*, Vol 42, No 4, July-Aug 2005, pp 699-710..

[38] Mailhe, L.M., and Guzman, J.J., "Initialization and Resizing of Formation Flying using Global and Local Optimization Methods", *IEEE Aerospace Conference Proceedings*, 2004.

[39] Lawden, D.F., *Optimal Trajectories for Space Navigation*, Butterworths, London, 1963.

[40] Zanon, D.J., and Campbell, M.E., "Mission Objectives in Tetrahedral Formation Maneuvering"; *AIAA Guidance, Navigation, and Control Conference*, AIAA-2005-5834, 2005.

[41] Zanon, D.J., and Campbell, M.E., "Spacecraft Formation Fuel Optimal Maneuvers with Attitude Constraints"; *AIAA Guidance, Navigation, and Control Conference*, AIAA 2006-6588, 2006.

[42] Rahmani, A., Mesbahi, M., and Hadeagh, F.Y., "On the Optimal Balanced-Energy Formation Flying Maneuvers", *AIAA Guidance, Navigation, and Control Conference*, AIAA 2005-5836, 2005.

[43] Sultan, C., Seereram, S., and Mehra, R.K., "Deep Space Formation Flying Spacecraft Path Planning", *International Journal of Robotics Research*, Vol. 26, No. 4, Pg 405-430, 2007.

[44] Huntington, G.T., and Rao, A.V., "Optimal Configuration of Spacecraft Formations via a Gauss Pseudospectral Method", AAS 05-103, 2005.

[45] Inalhan, G., and How, J.P., "Formation Flying Control in Eccentric Orbits", *AIAA Guidance, Navigation, and Control Conference*, AIAA Paper 2001-4092, Montreal, Aug. 2001.

[46] Guzman, J.J., and Shiff, C., "A Preliminary Study for a Tetrahedron Formation: Quality Factors and Visualizations", *AIAA/AAS Astrodynamics Specialists Conference*, Aug. 2002.

[47] Robert, P., et al, "Tetrahedron Geometric Factors", *Analysis Methods for Multi-Spacecraft Data*, pp 323-348; Pashmann and Daly, eds., ISSI Report SR 001, ESA Publications Division, Noordwijk, The Netherlands, 1998.

[48] European Space Agency Science Programme Cluster; URL: http://clusterlaunch.esa.int/science-e/www/area/index.cfm?fareaid=8 [cited: 20 Feb 2008]

[49] Wertz, J.R., and Bell, R., "Autonomous Rendezvous and Docking Technologies — Status and Prospects", *SPIE Space Systems Technology and Operations Conference AeroSense Symposium*, SPIE Paper No 5088-3, 2003.

[50] Guibot, V.M., and Scheeres, D.J., "Solving Relative Two-Point Boundary Value Problems: Spacecraft Formation Flight Transfer Application", *AIAA Journal of Guidance, Control, and Dynamics*, Vol 27, No 4, July-Aug 2004.

[51] Eades, J.B., Jr., "Operational requirements and the geometry of a station-keeping maneuver", *Celestial Mechanics*, Vol 16, Nov 1977, pp. 315-342.

[52] Beard, R.W., and Hadeagh, F.Y., "Finite Thrust Control for Satellite Formation Flying with State Constraints", *Proceedings of the American Control Conference*, 1999.

[53] Shaohua, Y., "Autonomous rendezvous in elliptical orbits", *Acta Astronautica*, Vol 41, Issue 2, Pg 95-101, July 1997.

[54] Garcia, I., and How, J.P., "Trajectory Optimization for Satellite Reconfiguration Maneuvers with Position and Attitude Constraints", *Proceedings of the 2005 American Controls Conference*, Vol 2, Pg 889-894; 2005.

[55] Beard, R.W., and Hadeagh, F.Y., "A Coordination Architecture for Spacecraft Formation Control", *IEEE Transactions on Control System Technology*, Vol 9, No 6, 2001.

[56] Hall, C.D., and Ross, I.M., "Optimal Attitude Control for Coplanar Orbit Transfers", *The John L. Junkins Astrodynamics Symposium*, AAS 03-262, College Station, Texas, 2003.

[57] Tietz, J.C., and Almand, B.J., "Autonomous spacecraft rendezvous and docking", *Proceedings of the Eighth Annual Rocky Mountain Conference on Guidance and Control*, Keystone, CO, 1985.

[58] Zimpfer, D., Kachmar, P., and Tuohy, S., "Autonomous Rendezvous, Capture and In-Space Assembly: Past, Present and Future", *AIAA 1st Space Exploration Conference*, AIAA 2005-2523, Orlando, FL, 2005.

[59] Machula, M.F., and Gandhoo, G.S., "Rendezvous and Docking for Space Exploration", *AIAA 1st Space Exploration Conference*, AIAA 2005-2716, Orlando, FL, 2005.

[60] Polites, M.E., "Technology of Automated Rendezvous and Capture in Space", *Journal of Spacecraft and Rockets*, Vol 36, No 2, pp. 280-291, Mar-Apr 1999.

[61] Guerra, C.J., and Page, L.A., "Autonomous Planning for Satellite Rendezvous and Proximity Operations", The Charles Stark Draper Laboratory, Inc.; published under AIAA-2005-7026, 2005.

[62] Breger, L., and How, J.P., "Safe Trajectories for Autonomous Rendezvous of Spacecraft", *Proceedings of the AIAA Guidance, Navigation, and Control Conference and Exhibit*, AIAA 2006-6584, Keystone, CO, 2006.

[63] Kornfeld, R.P., et al., "New millennium ST6 autonomous rendezvous experiment (ARX)", *Proceedings of the IEEE Aerospace Conference*, Vol 1, 2003.

[64] Campbell, M.E., Schetter. T., "Comparison of Multi-Agent Based Organizations for Satellite Constellations", *AIAA Journal of Spacecraft and Rockets*, Vol 39, No. 2, March-April 2002, pp. 274-283.

[65] Hoffman, H.J., and Wielandt, H.W., "The Variation of the Spectrum of a Normal Matrix", *Duke Math Journal*, Vol 20, pp 37-39, 1953.

[66] Kall, P., and Mayer, J., *Stochastic Linear Programming: Models, Theory, and Computation*, Springer Science and Business Media, New York, 2005.

[67] Tillerson, M., Breger, L., and How, J.P., "Distributed Coordination and Control of Formation Flying Spacecraft", *Proceedings of the IEEE American Control Conference*, pp 1740-1745, 2003

[68] Jafry, Y.R., Cornelisse, J., and Reinhard, R., "LISA - A laser interferometer space antenna for gravitational-wave measurements", *ESA Journal*, Vol 18, No 3, pp 219-228, 1994.

[69] Fridlund, C.V.M., "Darwin The Infrared Space Interferometry Mission", ESA Bulletin 103, Aug. 2000.